Summer November 2014

Structural, Electronic and Catalytic Properties of Graphene-supported Platinum Nanoclusters

Ioanna Fampiou
University of Massachusetts Amherst

Recommended Citation

Fampiou, Ioanna, "Structural, Electronic and Catalytic Properties of Graphene-supported Platinum Nanoclusters" (2014). *Doctoral Dissertations*. 185.
https://doi.org/10.7275/5979991.0 https://scholarworks.umass.edu/dissertations_2/185

STRUCTURAL, ELECTRONIC AND CATALYTIC PROPERTIES OF GRAPHENE–SUPPORTED PLATINUM NANOCLUSTERS

A Dissertation Presented

by

IOANNA FAMPIOU

Submitted to the Graduate School of the
University of Massachusetts Amherst in partial fulfillment
of the requirements for the degree of

DOCTOR OF PHILOSOPHY

September 2014

Mechanical Engineering

STRUCTURAL, ELECTRONIC AND CATALYTIC PROPERTIES OF GRAPHENE–SUPPORTED PLATINUM NANOCLUSTERS

A Dissertation Presented

by

IOANNA FAMPIOU

Approved as to style and content by:

Ashwin Ramasubramaniam, Chair

Robert W. Hyers, Member

Dimitrios Maroudas, Member

Donald Fisher, Department Head
Mechanical Engineering

To my mother, Eleni and to the memory of my beloved grandparents
for inspiring me to work hard, aim high and follow my dreams.

ACKNOWLEDGMENTS

I would like to express my sincere gratitude to my thesis supervisor, Professor Ashwin Ramasubramaniam for his continuous support and guidance throughout the course of my graduate studies. He has been an invaluable mentor showing utmost regard, care, patience, and encouragement. I am also immensely thankful to the members of my committee, Professor Dimitrios Maroudas and Professor Robert W. Hyers for their service and their helpful comments and suggestions. My thanks are also due to Professor T. J. Mountziaris for his support and friendship and for serving as a mentor during my graduate school years.

I would be remiss if I didn't also acknowledge the members of our research group, past and present, Dr. Jin Yang, Corinne Carpenter, Raymond Gasper and Hongbo Shi, for our fruitful discussions, exchange of ideas and the fun times we spent together in the lab. Thanks to all the friends I made while in Amherst, for making my stay enjoyable and pleasant. I strongly hope that our paths cross again in the future.

I would like to express my gratitude to Daniel Fay for bringing happiness and comfort in my life and for keeping me mostly sane during the completion of my dissertation.

Last but not least, I am deeply grateful to my family and particular to my mother Eleni, for always supporting me and encouraging me to follow my dreams. I wouldn't have been where I am today without them.

This work was supported by U.S. Department of Energy under Award Number DE-SC0010610. Computational resources provided by the National Energy Research Scientific Computing Center, which is supported by the Office of Science of the U.S.

Department of Energy under Contract No. DE-AC02-05CH11231 are also acknowledged.

ABSTRACT

STRUCTURAL, ELECTRONIC AND CATALYTIC PROPERTIES OF GRAPHENE–SUPPORTED PLATINUM NANOCLUSTERS

SEPTEMBER 2014

IOANNA FAMPIOU
Diploma, NATIONAL TECHNICAL UNIVERSITY OF ATHENS
Ph.D., UNIVERSITY OF MASSACHUSETTS AMHERST

Directed by: Professor Ashwin Ramasubramaniam

Carbon materials are predominantly used as catalytic supports due to their high surface area, excellent electrical conductivity, resistance to corrosion and structural stability. Graphene, a 2D monolayer of graphite, with its excellent thermal, electronic and mechanical features, has been considered a promising support material for next generation metal-graphene nanocatalysts. The main focus of this dissertation is to investigate the properties of such metal-graphene nanocomposites using computational methods, and to develop a comprehensive understanding of the experimentally observed enhanced catalytic activity of graphene–supported Platinum (Pt) clusters. In particular, we seek to understand the role of graphene supports on the ground-state morphology and the electronic structure of graphene–supported Pt nanoparticles, which correlate strongly with their catalytic activity. First, through a series of empirical potential and density functional theory (DFT) calculations, we determine low-energy isomers of Pt nanoclusters on pristine and defective graphene.

Our results indicate that point defects in the graphene support enhance the cluster-support interaction, increasing their stability and significantly alter their electronic properties. Next, we investigate the support effects on CO and O adsorption on graphene–supported Pt_{13} nanoclusters. Defective-graphene-supported Pt_{13} nanoclusters bind CO and O more weakly than clusters on pristine graphene or unsupported clusters. Additional *ab initio* MD calculations on COsaturated Pt_{13} nanoclusters show that support defects are crucial in stabilizing Pt_{13} clusters at high CO-coverages; in contrast, Pt_{13} clusters supported on pristine graphene desorb upon CO saturation, leading to potential catalyst loss. Finally, we examine the support effects on the CO oxidation reaction on graphene–supported Pt_{13} nanoclusters. A detailed study of the CO oxidation kinetics is undertaken in the high CO coverage regime, locating transition states and minimum energy pathways. The relevant kinetic mechanism is sampled at various surface sites on clusters bound at support defects and on unsupported clusters. The results of this study show that strong cluster-support interactions can substantially reduce the reaction barrier for CO oxidation on graphene–supported clusters compared to unsupported ones. Our studies suggest that defect engineering of graphene could serve to enhance the catalytic activity of ultra-small Pt clusters, opening up another dimension for rational design of catalytic materials.

TABLE OF CONTENTS

Page

ACKNOWLEDGMENTS . . . . **v**

ABSTRACT . . . . **vii**

LIST OF TABLES . . . . **xii**

LIST OF FIGURES . . . . **xv**

CHAPTER

1. INTRODUCTION AND BACKGROUND **1**

1.1 A Brief History of Surface Catalysis 1
1.2 Fuel Cell Electrocatalysts 4

1.2.1 Carbon Materials as Catalytic Supports 6

1.3 Platinum–Graphene Nanocomposites for Catalysis 10

1.3.1 Experimental Studies of Pt–graphene Nanocomposites for Catalysis 10
1.3.2 Computational Studies of Minimum-Energy Structures of Clusters and Pt–graphene Nanocomposites for Catalysis 12

1.4 Research Objectives 14
1.5 Dissertation Outline 15

2. BINDING OF PT NANOCLUSTERS TO POINT DEFECTS IN GRAPHENE: ADSORPTION, MORPHOLOGY, AND ELECTRONIC STRUCTURE **18**

2.1 Introduction 18
2.2 Computational Details 23
2.3 Results and discussion 27

2.3.1 Adsorption of Pt atoms 27
2.3.2 Adsorption of Pt dimers 28
2.3.3 Adsorption of Pt trimers 30
2.3.4 Adsorption of Pt tetramers 34
2.3.5 Adsorption of Pt$_{13}$ clusters 35
2.3.6 Electronic Structure of adsorbed Pt$_{13}$ clusters 41

2.4 Conclusions 46

3. CO ADSORPTION ON DEFECTIVE GRAPHENE–SUPPORTED PT$_{13}$ NANOCLUSTERS 50

3.1 Introduction 50
3.2 Computational Details 52
3.3 Results and Discussion 53

3.3.1 CO adsorption on free and graphene–supported Pt$_{13}$ clusters 53
3.3.2 Electronic structure of CO bound on graphene-supported and free Pt$_{13}$ clusters 58

3.4 Conclusions 61

4. THE INFLUENCE OF SUPPORT EFFECTS ON CO OXIDATION KINETICS ON CO–SATURATED GRAPHENE–SUPPORTED PT$_{13}$ NANOCLUSTERS 63

4.1 Introduction 63
4.2 Computational Details 66
4.3 Results and Discussion 69

4.3.1 Support effects on CO and O adsorption on graphene–supported Pt$_{13}$ clusters 69
4.3.2 Effect of CO-saturation on the stability of graphene–supported Pt$_{13}$ clusters 72
4.3.3 CO oxidation on defective-graphene supported and free CO–saturated Pt$_{13}$ clusters 76

4.4 Conclusions 84

5. SUMMARY, CONCLUSIONS AND FUTURE WORK 85

5.1 Summary 85
5.2 Conclusions 87
5.3 Future Directions 88

APPENDICES

A. EDGE STRESSES OF NON-STOICHIOMETRIC EDGES IN TWO-DIMENSIONAL CRYSTALS 91
B. ELASTIC PROPERTIES OF GRAPHENE NANOMESHES 97
C. DENSITY-FUNCTIONAL TIGHT-BINDING SIMULATIONS OF CURVATURE-CONTROLLED LAYER DECOUPLING AND BAND-GAP TUNING IN BILAYER MOS$_2$ 103

BIBLIOGRAPHY 109

LIST OF TABLES

Table **Page**

2.1 Optimal adsorption energies, formation energies, C-Pt bond lengths (d_{C-Pt}), and Pt-Pt bond lengths (d_{Pt-Pt}) for single Pt atom on pristine graphene, single vacancy, unreconstructed divacancy, 5-8-5 reconstructed divacancy, and 555-777 reconstructed divacancy. EP values are in parentheses. 29

2.2 Optimal adsorption energies, formation energies, C-Pt bond lengths (d_{C-Pt}), and Pt-Pt bond lengths (d_{Pt-Pt}) for Pt dimers on pristine graphene, single vacancy, unreconstructed divacancy, 5-8-5 reconstructed divacancy, and 555-777 reconstructed divacancy. EP values are in parentheses. 31

2.3 Optimal adsorption energies, formation energies, average C-Pt bond lengths ($\langle d \rangle_{C-Pt}$), and average Pt-Pt bond lengths ($\langle d \rangle_{Pt-Pt}$) for Pt trimers on pristine graphene, single vacancy, unreconstructed divacancy, 5-8-5 reconstructed divacancy, and 555-777 reconstructed divacancy. EP values are in parentheses. 33

2.4 Optimal adsorption energies, formation energies, average C-Pt bond lengths ($\langle d \rangle_{C-Pt}$), and average Pt-Pt bond lengths ($\langle d \rangle_{Pt-Pt}$) for Pt tetramers on pristine graphene, single vacancy, unreconstructed divacancy, 5-8-5 reconstructed divacancy, and 555-777 reconstructed divacancy. EP values are in parentheses. 35

2.5 Optimal adsorption energies, formation energies and average Pt-Pt bond lengths ($\langle d \rangle_{Pt-Pt}$) for Pt_{13} clusters on pristine graphene, single vacancy, unreconstructed divacancy, 5-8-5 reconstructed divacancy, and 555-777 reconstructed divacancy. Results are reported both for structural relaxation of high-symmetry clusters as well as annealed and relaxed clusters. EP results are in parentheses; for Annealing+Relaxation, the EP energies and bond lengths are averaged over eight different low energy structures. 37

2.6 *d*-band centers (ϵ_d) of adsorbed Pt_{13} clusters (relative to Fermi level) on various defective and defect-free graphene supports and charge transfer (Δq) *from* the Pt_{13} cluster *to* the support (electron charge taken to be negative). 44

3.1 Average adsorption energy and bond lengths (d_{C-O}) for CO molecules adsorbed on low-symmetry Pt_{13} clusters supported on pristine and defective (single vacancy, unreconstructed divacancy, 555-777 reconstructed divacancy) graphene, as well as on free Pt_{13} clusters. CO adsorption energies on Pt(111) at an on-top (T) site, a vacancy site (V) and a vacancy line (V-line) are reported for comparison. For reference, the C-O bond length in an isolated molecule is calculated to be 1.17 Å. 55

3.2 Average charge transfer [Δq (e$^-$)] from the Pt_{13} cluster to CO and pristine graphene, single vacancy, unreconstructed divacancy and 555-777 reconstructed divacancy based on Bader analysis. (Positive/negative numbers indicate accumulation/depletion of electrons.) 60

4.1 Average adsorption energy for CO (from Ref. [46]) and O molecules adsorbed on low-symmetry Pt_{13} clusters supported on pristine and defective (single vacancy, unreconstructed divacancy) graphene, as well as on free Pt_{13} clusters. The position of *d*-band center (E_{d-band}) for the Pt_{13} clusters is reported in the last column. 69

4.2 Average charge transfer [Δq (e$^-$)] from the Pt_{13} cluster to O and pristine graphene, single vacancy, and unreconstructed divacancy based on Bader analysis. (Positive/negative numbers indicate accumulation/depletion of electrons.) 72

4.3 Adsorption energy of the CO–saturated Pt_{13} clusters to the different graphene substrates is reported in the first column. Average charge transfer [Δq (e$^-$)] from the CO–saturated Pt_{13} cluster to the CO molecule and pristine graphene, single vacancy, and unreconstructed divacancy substrates based on Bader analysis. (Positive/negative numbers indicate accumulation/depletion of electrons.) 73

4.4 Adsorption energy per CO molecule on graphene–supported and free CO–saturated Pt_{13} clusters is reported in the first column. Single CO adsorption energy[46] on graphene–supported and free Pt_{13} clusters is reported in the second column. Results for CO adsorption at a Pt(111) surface are also included for comparison. 75

4.5 Activation energies (E_a) for the CO oxidation reaction on CO–saturated Pt_{13} clusters. 79

LIST OF FIGURES

Figure **Page**

1.1 Schematic representation of a membrane–electrode assembly of a PEMFC. Platinum particles and carbon agglomerates are colored in black and dark gray, respectively. [116] 5

2.1 DFT-optimized cluster geometries in vacuum for linear and triangular Pt_3 clusters; planar and tetrahedral Pt_4 clusters; and icosahedral (I_h) and cuboctahedral (O_h) Pt_{13} clusters. 25

2.2 Defect-free and defective graphene substrates employed in this study. Pentagons, heptagons, and octagons associated with divacancy reconstructions are indicated in the figure. 26

2.3 Low-energy DFT configurations for adsorption of a Pt atom on graphene. Cyan and gold spheres represent C and Pt atoms, respectively. 29

2.4 Low-energy DFT configurations for Pt dimers on graphene. Cyan and gold spheres represent C and Pt atoms, respectively. 32

2.5 Low-energy DFT configurations for Pt trimers on graphene. Cyan and gold spheres represent C and Pt atoms, respectively. 33

2.6 Low-energy DFT configurations for Pt tetramers on graphene. Cyan and gold spheres represent C and Pt atoms, respectively. 36

2.7 Low-energy configurations obtained by DFT structural relaxation of Pt_{13} clusters on graphene. Cyan and gold spheres represent C and Pt atoms, respectively. 38

2.8 Selected low-energy configurations obtained by DFT structural relaxation of EP-based MD annealing of Pt_{13} clusters on graphene. Cyan and gold spheres represent C and Pt atoms, respectively. 39

2.9 (a) Adsorption energy (E_{ad}) versus average bond length ($\langle d\rangle_{Pt-Pt}$) from DFT relaxation of the lowest-energy Pt_{13} clusters on graphene supports obtained after EP-based MD annealing. Vertical dotted lines indicate the average bond lengths for bulk Pt and for unsupported clusters (annealed clusters removed from graphene substrate and relaxed). (b) E_{ad} versus $\langle d\rangle_{Pt-Pt}$ obtained after averaging over eight different low energy structures obtained with the EP-based MD annealing schedule. (Error bars are much too small to be visible on this scale and are omitted.) The corresponding data are in Table 2.5. 40

2.10 Projected density of states (PDOS) plots for clusters subjected to relaxation alone: (a) free graphene, (b) graphene after Pt_{13} adsorption, (c) adsorbed Pt_{13} cluster, (d) free Pt_{13} cluster. (e) Charge-density difference plot. Isosurfaces are at 0.027 e/Å^3); yellow (blue) color represents charge accumulation (depletion). The charge lost by Pt atoms bound to the substrate is indicated. 43

2.11 Projected density of states (PDOS) plots for annealed and relaxed clusters: (a) free graphene, (b) graphene after Pt_{13} adsorption, (c) adsorbed Pt_{13} cluster, (d) free Pt_{13} cluster. (e) Charge-density difference plot. Isosurfaces are at 0.034 e/Å^3); yellow (blue) color represents charge accumulation (depletion). The charge lost by Pt atoms bound to the substrate is indicated. 47

2.12 Position of *d*-band center ($\epsilon_{\mathrm{d,Pt}}$) relative to the Fermi level for supported Pt_{13} clusters subjected to (a) relaxation alone, and (b) annealing followed by relaxation. Horizontal dotted lines indicate the *d*-band center of the Pt(111) surface ($\epsilon_{\mathrm{d,Pt(111)}}$) and the average *d*-band center of the various free Pt_{13} clusters ($\langle\epsilon_{\mathrm{d,Pt_{13}}}\rangle$) considered here. Charge transfer from (c) relaxed, and (d) annealed and relaxed Pt_{13} clusters to the substrate. (The electron charge is taken to be negative here.) The dashed lines in all figures are merely a guide to the eye. 48

3.1 Sampled CO adsorption sites on a low-energy Pt_{13} cluster supported at a single vacancy in graphene. Cyan, gold, and red spheres represent C, Pt, and O atoms, respectively. 54

3.2 Side and top view of selected low energy DFT configurations for adsorption of a CO molecule on graphene-supported Pt_{13} clusters. Cyan, gold and red spheres represent C, Pt and O atoms, respectively. 56

3.3 Side and top view of DFT configurations for adsorption of a CO molecule on Pt(111) surface slabs. Cyan, gold and red spheres represent C, Pt and O atoms, respectively. 57

3.4 CO adsorption energy (E_{ad}) as a function of *d*-band center (ϵ_d) relative to the Fermi energy for supported Pt_{13} clusters, free Pt_{13} clusters, and Pt(111) surface. A downshift of the cluster *d*-band center with respect to the Fermi level (more negative ϵ_d) is directly correlated with weaker adsorption of CO on the cluster. Error bars indicate 95% confidence intervals obtained from sampling over multiple adsorption sites on the cluster. 59

3.5 Charge-density difference plots for the selected DFT configurations of Figure 3.2. Isosurfaces are at 0.054 e/$Å^3$; yellow(blue) color represents charge accumulation(depletion). 61

4.1 Side and top view of selected low energy DFT configurations for adsorption of an O atom on graphene-supported Pt_{13} clusters. Cyan, gold and red spheres represent C, Pt and O atoms, respectively. 70

4.2 CO (top) and O (bottom) adsorption energy (E_{ad}) as a function of *d*-band center (ϵ_d) relative to the Fermi energy for supported Pt_{13} clusters, free Pt_{13} clusters, and Pt(111) surface. Error bars indicate 95% confidence intervals obtained from sampling over multiple adsorption sites on the clusters. CO adsorption energy results are adapted from Ref. [46]. 71

4.3 Fully relaxed atomic structures and charge-density difference plots for graphene–supported (a, b and, c) and free (d) CO–saturated Pt_{13} clusters. Isosurfaces are at 0.081 e/$Å^3$; yellow(blue) color represents charge accumulation(depletion). Cyan, gold and red spheres represent C, Pt and O atoms, respectively. 74

4.4 Minimum energy pathway and atomic structures for the CO oxidation reaction on a CO–saturated Pt_{13} cluster supported at a SV (Case (a)). Cyan, gold and red spheres represent C, Pt and O atoms, respectively. Pink spheres denote the O_2 molecule that participates in the reaction. 79

4.5 Minimum energy pathway and atomic structures for the CO oxidation reaction on a CO–saturated Pt_{13} cluster supported at a SV (Case (b)). Cyan, gold and red spheres represent C, Pt and O atoms, respectively. Pink spheres denote the O_2 molecule that participates in the reaction. 81

4.6 Minimum energy pathway and atomic structures for the CO oxidation reaction on a CO–saturated Pt_{13} cluster supported at a DV. Cyan, gold and red spheres represent C, Pt and O atoms, respectively. Pink spheres denote the O_2 molecule that participates in the reaction. 82

4.7 Minimum energy pathway and atomic structures for the CO oxidation reaction on an unsupported CO–saturated Pt_{13} cluster. Cyan, gold and red spheres represent C, Pt and O atoms, respectively. Pink spheres denote the O_2 molecule that participates in the reaction. 83

CHAPTER 1

INTRODUCTION AND BACKGROUND

1.1 A Brief History of Surface Catalysis

Chemical catalysis affects our lives in myriad ways. Catalysts provide a means of changing the rates at which chemical bonds are formed and broken thereby controlling the yields of chemical reactions to increase the amounts of desirable products while reducing the amounts of undesirable ones. Catalysis lies at the heart of our quality of life: reduced emissions of modern cars, the abundance of fresh food at our stores, and the new pharmaceuticals that improve our health are made possible by chemical reactions controlled by catalysts.

Catalysis as a scientific discipline originated in the early 19th century. In 1814, Kirchoff reported that acids aid the hydrolysis of starch to glucose. The oxidation of hydrogen by air over platinum (Pt) was observed by H. Davy (1817) and E. Davy (1820). Platinum was also found to aid the oxidation of CO and ethanol (Dobereiner).[143] Faraday was the first to carry out experiments to explore why Pt facilitates the oxidation reactions of different molecules. Thus, Faraday was the first scientist to study catalytic reactions. In 1835, Berzelius was the first to systematically investigate previous recorded observations and classified them as *catalysis*. [107] He suggested the existence of a catalytic force associated with the action of catalysts. Catalyst-based technologies were introduced in the second half of the 19th century. During this period it became clear that catalysis was applicable in most chemical processes. This new perception of catalysis was formulated by Ostwald, who developed the process of ammonia oxidation to form nitric oxide, the precursor to nitric acid manufacture (1902). [7]

During the end of the nineteenth century the growth of academic knowledge translated into industrial applications. At this point the number of developed catalytic processes had grown into hundreds and the economic potential of some of these processes were highly feasible. Catalysis science was developed (1915–1940) through the efforts of Langmuir (sticking probability, adsorption isotherm, dissociative adsorption, role of monolayers), Emmett (surface area and measurements, kinetics of ammonia synthesis), Taylor (active sites, activated adsorption), Bonhoeffer, Rideal, Roberts, Polanyi, Farkas (kinetics and molecular mechanisms of ethylene hydrogenation, isotope exchange, intermediate compound theories), and many others. There was also a general growth in the demand for bulk chemicals and therefore minimization of by-products, by catalysis, had evident economic advantages. Catalyzed reactions of CO and hydrogen were utilized to produce methanol in 1923 and higher-molecular-weight liquid hydrocarbons by 1930. The production of motor fuels became one of the chief aims of catalysis during the period of 1930–1950. [158]

The discovery of abundant and inexpensive oil in the early 1950s focused the development of catalytic processes on converting petroleum crude to fuels and chemicals. Oil and oil-derived intermediates (ethylene, propylene) became the dominant feedstocks. Platinum (metal–) and acid (oxide–) catalyzed processes were developed to convert petroleum to high-octane fuels. The discovery of microporous crystalline alumina silicates (zeolites) provided more selective and active catalysts for many reactions, including cracking, hydrocracking, alkylation, isomerization, and oligomerization. A new generation of more active bimetallic catalysts dispersed on high–surface area oxides were synthesized. The new catalysts were also more resistant to deactivation. [158]

The energy crisis in the early 1970s renewed interest in chemicals and fuels, producing technologies using feedstocks other than crude oil. Intensive research was carried out utilizing coal, shale, and natural gas to develop new technologies and to improve on the activity and selectivity of older catalyst–based processes. Environmental catalysis was the first step towards the modern chemical industry where catalysis is applied to almost every process, including the production of fine chemicals for pharmaceutical applications to the production of bulk chemicals and exhaust gas catalysts. [107]

Modern surface science developed during the same period and has been applied intensively ever since to explore the working of catalysts on the molecular level, to characterize the active surface, and to aid the development of new catalysts for new chemical reactions. During the later part of the 20th century, with the development of nanoscience, nanocatalysis has clearly emerged as a domain to answer the demanding conditions for catalyst improvement.

Today, we are facing a variety of unprecedented challenges in creating alternative fuels, reducing harmful by-products in manufacturing, cleaning up the environment and preventing future pollution, dealing with the causes of global warming, preventing the release of toxic substances and infectious agents, and creating safe pharmaceuticals. Catalysts are needed to meet these challenges and their complexity and diversity demand a revolution in the way catalysts are designed and used. Therefore, the application of new methods for synthesizing and characterizing molecular and material systems is essential. Opportunities to understand and predict how catalysts work at the atomic scale and the nanoscale are made possible by breakthroughs in the last decade in computation, measurement techniques, and imaging and by new developments in catalyst design, synthesis, and evaluation.

1.2 Fuel Cell Electrocatalysts

The use of fossil fuels, especially coal, oil, and gas, represents a serious environmental threat and might lead to a global energy crisis, including natural resource exhaustion, pollutant emission, and waste generation. Carbon dioxide emission from burning fossil fuels is considered a key contributor to climate change and related environmental problems. Consequently, there is urgent need to increase electricity-generation efficiency and to develop clean, sustainable, and renewable energy sources. Fuel cells are an electrochemical energy conversion technology to directly convert the chemical energy of fuels, such as hydrogen, methanol, ethanol, and natural gas, to electrical energy. Fuel cells are considered to be the most efficient and least polluting power-generating technology and are a potential and viable candidate to moderate the fast increase in power requirements and to minimize the impact of the increased power consumption on the environment. [133]

A fuel cell, as depicted in Figure 1.1, [116] is an electrochemical cell comprised of three main components: the anode, cathode, and the electrolyte. Assembly of these three components is often referred to as membrane–electrode assembly (MEA). Electric current generation in a fuel cell depends largely on the kinetics of the reaction that takes place at the anode and the cathode. Generally, hydrogen gas is the preferred fuel for fuel cells. Hydrogen and oxygen are consumed to produce electricity giving water as the only byproduct, with no greenhouse gas emission. The main obstacle in the use of hydrogen as an energy carrier is that hydrogen is not a readily available fuel. The direct use of liquid fuels in fuel cells is of significant importance due to potentially higher energy density and higher maximum thermodynamic efficiencies. Liquid fuels, such as methanol and ethanol, have several advantages with respect to hydrogen. They are relatively cheap; are easily handled, transported, and stored; and have a high theoretical energy density. However, apart from the energy density, the toxicological–ecological hazards of the liquid fuels and the environmental effects of the byproducts of the liquid fuel oxidation reactions should also be taken into account when selecting one particular fuel. Direct liquid fuel cells using methanol, ethanol, propanol, formic acid, etc., suffer from the additional problem of catalyst poisoning due to CO formation from the indirect decomposition of liquid fuels. [75] Therefore, the development of advanced nanocatalysts is imperative to significantly enhance the electrocatalytic activity and durability of the Pt-based catalysts that are required for liquid fuel–based fuel cell systems.

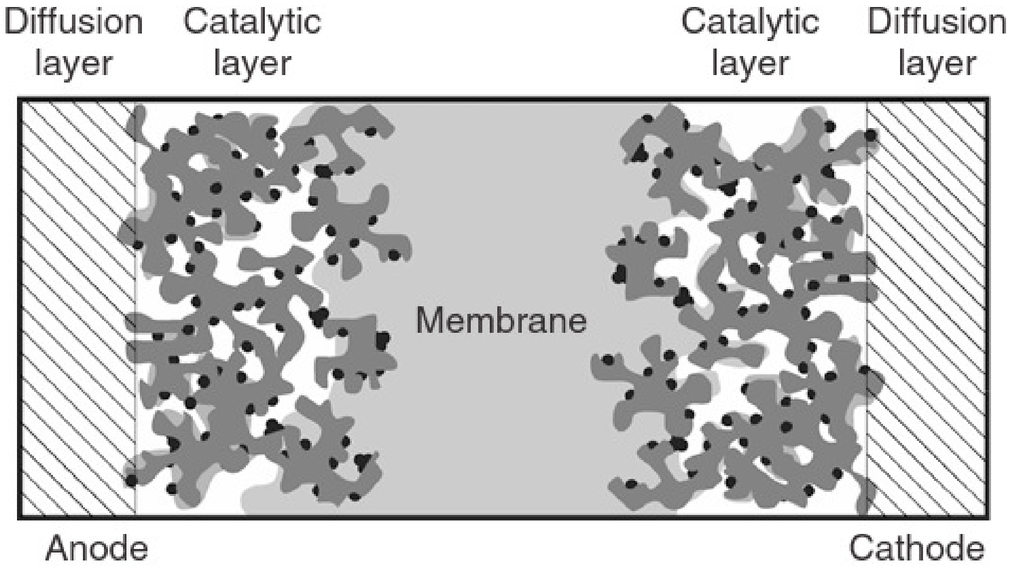

Figure 1.1: Schematic representation of a membrane–electrode assembly of a PEMFC. Platinum particles and carbon agglomerates are colored in black and dark gray, respectively. [116]

Fuel cells can be classified based on the type of fuel used, for example, direct methanol fuel cells (DMFCs), direct ethanol fuel cells (DEFCs), direct formic acid fuel cells (DFAFCs), and direct carbon fuel cells (DCFCs). Apart from the type of fuel used, fuel cells are usually classified according to their working temperature or to the electrolyte employed. There are, thus, low- and high- temperature fuel cells. Low-temperature fuel cells include alkaline fuel cells (AFCs), polymer electrolyte membrane fuel cells (PEMFCs,) direct methanol fuel cells (DMFCs), and phosphoric acid fuel cells (PAFCs). The high-temperature fuel cells operate at 500° C – 1000° C. Due to their high operating temperature, they show a higher tolerance to typical catalyst poisons, such as CO, produce high-quality heat for reforming of hydrocarbons, and offer the possibility of direct utilization of hydrocarbon fuels. As for the electrolytes used in fuel cells, they can be solid (polymer or ceramic) or liquid (aqueous or molten) and must have high ionic conductivity with negligible electronic conductivity. [75]

After this brief description of the basic concepts of fuel cells, we will now focus on the materials composing the catalytic layers in the membrane electrode assembly (MEA), where the electrochemical reactions occur. The structure and composition of the MEAs have undergone decisive changes during the past 30 years. [160] In early PEMFCs the catalytic layers were prepared from noble metals and thus contained very high metal loadings per geometric MEA area. Later, it became apparent that precious metals in these catalytic layers were not utilized efficiently and the new generation of PEMFCs emerged, based on carbon-supported precious-metal catalysts (usually Pt or Pt-based alloy). Platinum catalysts are often the transition metal of choice, for fuel cell catalysts, due to their high activity and selectivity for a variety of electrochemical reactions. In the following section, we will focus on carbon materials as catalytic supports for PEMFCs and DMFCs, from traditional carbon supports to novel nanostructured forms of carbon.

1.2.1 Carbon Materials as Catalytic Supports

Because of their high conversion efficiency, low pollution, light weight, and high power density, low-temperature fuel cells have attracted lots of attention. However, the high catalyst cost is a major barrier to the commercialization due to the requirement of platinum-based catalysts for both the anode and cathode. In order to reduce the cost, a lot of effort has been focused on reducing the usage of precious metal content by enhancing the Pt utilization efficiency, creating Pt catalysts with a smaller size and high electrochemically active surface area.

Nowadays, the popular method to obtain a high active surface area is to deposit the Pt particles on a porous support. Various carbon materials such as graphite, carbon black, activated carbon, activated carbon fibers, ordered mesoporous carbon, pyrolytic carbon and polymer-derived carbon have been used to prepare carbon-supported catalysts. [8–10, 26, 37, 42, 48, 81, 162, 165, 174, 198] Carbon presents some unique characteristics: it is inert in acidic or basic environment, and can been functionalized by various methods so as to control its surface chemistry. In addition, carbon is abundant in nature and environmental friendly. The choice of the suitable support is determined by the chemical reactions with the aspects of high conversion rate, high selectivity, long-term stability and acceptable cost.

High surface area activated carbon and carbon blacks have been extensively used as the carbon materials of choice for most carbon supported catalysts, due to their flexible porous structure, high conductivity, and low cost. [11, 12] However, despite their high surface area, carbon black based electrocatalyst supports present two main problems: (i) they induce significant mass transfer limitations due to their dense structure, leading to a very low Pt utilization [141], and (ii) carbon black is known to undergo electrochemical oxidation, forming surface functional groups such as OH, COOH and CO, which further react to give CO_2 at the cathode of the fuel cell [78]. As carbon corrodes, Pt nanoparticles will detach from the carbon black and aggregate into larger particles resulting in the loss of Pt surface area and in the subsequent lowering of the performance of fuel cells. [108, 152] Activated carbon is usually manufactured by high-temperature pyrolysis of various vegetative residues as well as pitch and polymer substances, followed by activation to create desirable porous structure of the target materials. The advantage of chemical activation is the more uniform pore structure of the target activated carbon materials. Activated carbons possess high surface areas and micropore volumes, which makes them particularly attractive catalyst materials. On the other hand, there are several disadvantages associated with their extensive use, such as narrow microporosity, inconsistent quality with traces of impurities, and low mechanical and thermal stability, which essentially lower the performance of the catalyst. [10, 48, 165, 174, 178]

Ordered mesoporous carbons (OMCs) is another carbon material often used as a catalytic support, since these have controllable pore sizes, high surface areas, and large pore volumes. [26, 37, 162] It has been found that nanoporous carbons with 3D ordered pore structures can improve the mass transport of the reactants and products during fuel cell operation.[26, 37] The electrocatalysts that employ such OMC supports are shown to exhibit promising catalytic activities toward methanol oxidation and superior electrocatalytic mass activity toward oxygen reduction compared with the same catalyst dispersed on a conventional carbon black support. [26, 37] Generally, in these studies all OMC-supported metals presented higher metal dispersion and higher catalytic activity, both for oxygen reduction and methanol oxidation than carbon black–supported metals. However, OMCs contain a small oxygen surface groups, which might be disadvantageous in the long-term use of the catalyst.

Nanostructured forms of carbon, such as carbon nanotubes (CNTs) and carbon nanofibers (CNFs) have been exploited in the last two decades as alternative support materials in heterogeneous catalysis. [17, 51, 74, 94, 110, 135] CNTs are nanoscale cylinders of rolled up graphene sheets with an extensive range of variations, such as single-walled nanotubes and multi-walled nanotubes. CNFs have lengths on the order of micrometers while their diameter varies between tens to several hundreds of nanometers. The mechanical strength and electric properties of CNFs are similar to that of CNTs while their size and graphitic ordering can be well controlled. [147] The potential benefits of using these nanostructured forms of carbon as catalytic supports include higher utilization of active metal due to good mesoporosity that can improve mass transfer, high purity that can prevent the catalyst from self-poisoning, corrosion resistance, higher electrical conductivity, mechanical strength and thermal stability compared to carbon black supports. [97, 99, 177] A large number of studies have shown that Pt supported on CNTs and CNFs could exhibit better performance for the electro-oxidation of methanol [59, 69, 110], oxygen reduction reaction, [24, 82, 119, 182] and higher durability than on traditional carbon particles. [17, 51, 98, 161] However, there are several challenges to the development of CNT-/CNF-supported catalysts in terms of fabrication and synthesis, with the most significant limitation being the particle size control and CO poisoning prevention. High catalyst loading required for DMFCs is difficult to achieve in CNT– supported electrocatalysts. Without surface modification, most CNTs have insufficient binding sites to anchor the precursor metal ions or metal nanoparticles, which usually leads to poor dispersion and aggregation of metal nanoparticles, especially at high loading conditions. [184] Less than 30 wt% Pt/MWCNTs catalyst loading can be achieved because high Pt loading on unfunctionalized CNTs leads to aggregation. [190] Therefore functionalization of CNTs is essential for practical applications. Another limitation is that in comparison with carbon black, CNT–supported electrocatalysts commonly exist in unusual shapes and have bulky specific volumes, making the fabrication into fuel cell electrodes challenging. As for CNFs, despite their superior thermal stability and corrosion resistance in the low-temperature fuel cell environment, they have an inert surface with only a very limited amount of surface defects for the anchorage of Pt-catalyst nanoparticles, which may assist the particle agglomeration. This effect can be partially avoided by functionalization of CNFs to create surface functional groups that Pt nanoparticles can use as anchoring sites. [58, 100]

Before proceeding with describing the advantages of using Pt-graphene nanocomposites as electrocatalysts in fuel cells, which is the main focus of this dissertation, we could briefly conclude that the use of carbon materials with high surface area, good electrical conductivity, and suitable porosity as catalyst supports for precious metals increases due to the development of fuel cells. The high availability and low cost of carbon, make carbon blacks still the most popular support for fuel cell catalysts. Among the new nanostructured forms of carbon, CNTs are the most investigated as catalyst support for low-temperature fuel cells showing considerable advantages compared to traditional carbon blacks. However, commercialization aspects, including cost and durability of these new materials, have revealed inadequacies that need to be addressed before fuel-cell technology can gain a significant share of the electrical power market.

1.3 Platinum–Graphene Nanocomposites for Catalysis

Nanotechnology offers new insights in the development of advanced materials for alternative energy sources. As described in the previous sections, current research on materials for catalytic applications focuses on creating more active support surfaces and achieving lower precious metal content, optimizing the catalytic metal nanoparticles. Tuning the size and the morphology of the cluster and the properties of the support material is necessary to increase the catalyst efficiency. Since its discovery by Geim et al. [126] in 2004, graphene has attracted great scientific interest and has already shown much promise as a catalytic support in low-temperature fuel cells.

1.3.1 Experimental Studies of Pt–graphene Nanocomposites for Catalysis

Graphene, a single-atom thick layer of sp^2–bonded carbon atoms in a honeycomb lattice, due to its unique structure and excellent properties is considered a promising material for catalytic support in fuel cell electrodes. It offers high conductivity, high surface area, exceptionally high mechanical strength and one of the fastest available electron transfer capabilities. [125, 126]

Significant experimental research has been already performed and has shown that subnanometer Pt nanoparticles supported on functionalized graphene, graphene synthesized by graphene oxide (GO) and chemically converted graphene (CCG) show extraordinary properties as electrocatalytic supports in direct methanol fuel cells, proton exchange membrane fuel cells, and hydrogen fuel cells. [9, 12, 38, 40, 77, 82, 84, 90, 101, 102, 135, 139, 140, 142, 148, 149, 151, 155, 164, 166, 183, 185, 191, 192, 192, 194, 196] Experimental studies attribute the improved performance of Pt-graphene nanocatalysts to the synergetic effect between the Pt catalyst and the functionalized graphene substrate, leading to a strong interaction between the cluster and the support. [49, 67, 68, 84, 101, 137, 144, 172, 183] Experiments clearly reveal that electron damage–induced point defects in graphene are very effective traps for diffusing atoms and clusters. [144] Such defect-mediated anchoring of Pt nanoparticles is also shown to prevail in experimentally synthesized Pt-graphene composites, which are typically produced via solution processing of graphene oxide, known to contain lattice defects (vacancies, holes) and functional groups (carbonyls, epoxides, hydroxyls, etc.),[14, 96, 131] which can act as strong anchoring sites for Pt nanoparticles.[83, 84, 176] The presence of defects and functional groups could therefore explain the increased stability of Pt nanoparticles towards sintering in these composites.

The use of graphene oxide (GO) as catalyst support material has already shown promising results. [101, 140, 153, 181] Oxygen groups are introduced into the graphene structure during the preparation of GO, creating defect sites on the surface and at edge planes. These defect sites act as nucleation centers and anchoring sites for growth of metal nanoparticles. In comparison with CNTs, graphene nanosheets (GNs) possess not only similar stable physical properties but also large surface area. In addition, the production cost of GNS mass scale is cheaper than that of CNTs.[93] GNSs have been reported to have good dispersion stability and large surface area.

[138] Oxygen reduction reaction studies on Pt/RGO showed 11% higher maximum power density in comparison to commercial Pt/C catalyst. [60] Electrochemical data for methanol oxidation on Pt-Ru/GNS have shown better catalytic activity than that of Pt-Ru/Vulcan carbon. [20] When compared with standard Pt-carbon black catalysts, Pt-graphene composites display enhanced catalytic activity and tolerance to CO poisoning [101, 192] and, additionally, long-term stability toward sintering. [84, 101, 192] These results indicate that graphene nanosheets could be good candidates as support material for high-loading Pt catalysts in fuel cells.

1.3.2 Computational Studies of Minimum-Energy Structures of Clusters and Pt–graphene Nanocomposites for Catalysis

Computational modeling and simulations play an increasingly important role in the field of nanocatalysis. Direct numerical simulations can be very helpful in establishing quantitative understanding of structure–property–function–performance relationships that can lead to accelerated discovery of novel nanomaterials. Such computational findings can facilitate our quest to understand the physical and chemical effects at the nanoscale and can serve as guidelines for designing experiments and generating experimentally testable hypotheses.

From a computational perspective, the interaction of Pt clusters with graphene and CNTs has been explored in several recent studies. [2, 19, 22, 30, 32, 33, 41, 80, 81, 83, 105, 106, 117, 128, 129, 145, 170, 176, 179] Briefly, the following features of Pt-graphene interactions can be gleaned from these studies. First, Pt does not wet pristine graphene due to relatively high cohesive energy for Pt as compared to the Pt-C bond energy.[19, 117, 129] Consequently, Pt clusters on graphene are essentially three-dimensional structures for cluster sizes in excess of about ten atoms. Second, Pt clusters bind more strongly to defects (vacancies, disclinations, dopants, edges, 5-8-5 reconstructed divacancies)[2, 81, 83, 128, 176, 179] in graphene due to the formation of strong Pt-C bonds at the defect, which partially alleviates the disruption of the graphene sp^2 network. The electronic structure of the cluster is modified both due to bond formation as well as due to strains induced in the cluster. Third, there is a clear indication of charge transfer from the Pt cluster to the graphene support accompanied by a shift of the Pt *d*-band away from the Fermi level, which is greater in the presence of a support-defect.[30, 105, 128, 179] The binding energy of CO molecules, for example, is then found to decrease as one goes from an unsupported particle, to a supported one, to one on a defective support.[128] Similarly, the presence of vacancies in the graphene substrate has been shown to enhance the stability of Pt_{13} nanoparticles on the graphene support while weakening the O_2 adsorption energy on the cluster; this effect can alter the catalytic activity of the nanoparticle toward oxygen reduction.[105, 106] There have also been some recent computational studies investigating the catalytic performance of metal-graphene or metal-graphene-oxide supported nanoparticles [80, 95, 103, 105, 114, 159, 167, 169, 197]. For instance, the presence of a defect at the graphene support was also found to increase the reactivity of Pt_4 clusters and reduce the barrier of catalyzed CO oxidation. [197] Another study by Li *et al.*[95] showed high catalytic activity of Fe clusters anchored on graphene oxide for the CO reaction via the Eley-Rideal mechanism. Song *et al.* [159] reported enhanced catalytic activity of graphene-supported Cu clusters towards the catalytic oxidation of CO, while Lu *et al.*[114] reported a low activation barrier ($\sim$0.31 eV) for CO oxidation on graphene-supported Au clusters.

Briefly summarizing, the improved performance of Pt-graphene composite electrodes according to the studies previously reported, may then be attributed to several factors including: (i) stability towards sintering, which maintains high surface area over extended periods; (ii) improved electrical conductivity of graphene supports relative to standard carbon black counterparts; and (iii) fundamental modifications in the electronic structure of the supported nanoparticle as a result of strong binding to support defects. However, the relative importance of these factors and their potentially synergistic interaction is still neither understood nor analyzed in a systematic way and constitutes the main focus of this dissertation.

1.4 Research Objectives

This thesis is aimed at obtaining a fundamental and quantitative understanding of the complex phenomena that govern the properties of Pt–graphene nanocomposites as electrocatalysts in fuel cells. Our computational study follows a synergistic combination of first-principles Density Functional Theory (DFT) calculations with Empirical–Potential based classical Molecular Dynamics simulations. Through atomic-scale simulations of the key thermodynamic and kinetic processes, our modeling predictions and analyses aim to elucidate the fundamental mechanisms that underlie the experimentally observed enhanced electrocatalytic activity of Pt nanonclusters supported on graphene and provide insights into optimal catalyst design.

In particular, the goal of this thesis is to provide a systematic investigation of the structural, electronic and catalytic properties of Pt nanoclusters in relation to the type substrate point defect. More specifically, the thesis efforts are focused on (i) identification of the hierarchy of the energetics of binding of Pt_n, (n=1, 2, 3, 4, 13) clusters to pristine graphene, vacancies, unreconstructed divacancies, pentagon-octagon-pentagon (5-8-5) reconstructed divacancies, and haeckelite (555-777) reconstructed divacancies; (ii) identification of low-energy isomers of graphene-supported Pt clusters, the possible correlation between the structure of a Pt_n cluster with the type of binding defect and the effect of these substrate-induced structural modifications on the electronic structure of the clusters; (iii) analysis of the effect of the cluster–substrate interaction on the catalytic activity of graphene-supported Pt nanoclusters for electrochemical reactions; (iv) analysis of the effect of the clusters' CO-coverage on the stability of graphene–supported Pt nanoclusters; and (v) investigation of the detailed kinetic mechanisms for CO oxidation on graphene–supported CO–saturated Pt nanoclusters.

The outcomes of this thesis provide important insights into the observed phenomena in the body of experiments that have been reported in the literature and generate a series of experimentally testable hypotheses, which can guide future experiments in the field. The findings reported in this thesis are expected to be of fundamental importance toward the design of efficient graphene–supported Pt nanocatalysts with desired and tailored properties.

1.5 Dissertation Outline

The rest of this thesis is directed towards accomplishing the aforementioned research objectives. Accordingly, the remaining of this dissertation is organized as follows.

In Chapter 2, a systematic computational study of the adsorption energetics, structural features, and electronic structure of platinum nanoclusters supported on defective and defect-free graphene is presented. The study is based on a combination of classical empirical-potential based molecular dynamics and first principles DFT calculations and aims to identify low-energy isomers of graphene–supported Pt nanoclusters and analyze the effect of the nanoparticle–substrate interaction on the electronic properties of the system. The results reported in this chapter have appeared in the following publication:

- I. Fampiou, A. Ramasubramaniam, *Binding of Pt nanoclusters to defects in graphene: adsorption, morphology, and electronic structure*, *J. Phys. Chem. C* **2012**, 116, 6543–6555

In Chapter 3, a detailed study of the energetics of CO adsorption on low-energy graphene–supported Pt_{13} nanoclusters is presented and the effect of the cluster–substrate interaction on the CO tolerance of the system is addressed, via first-principles

DFT calculations. Since CO poisoning is a key issue in catalysis, the results of this study are particularly important, indicating the propensity of defective graphene substrates to reduce the binding energy of CO molecules on Pt_{13} clusters. The findings of this chapter have appeared in the following publication:

- I. Fampiou, A. Ramasubramaniam, *CO adsorption on defective graphene - supported Pt_{13} nanoclusters*, *J. Phys. Chem. C* **2013**, 117, 19927-19933

In Chapter 4, we systematically investigate, using DFT calculations, the role of support effects on the kinetics of CO oxidation reaction on fully CO–saturated graphene–supported Pt_{13} nanoclusters. CO oxidation is a reaction of practical relevance, as CO poisoning of the catalyst remains a serious problem in the operation of fuel cells, significantly compromising anode performance even in trace amounts. The relevant kinetic mechanisms are explored at various surface sites on unsupported Pt_{13} nanoclusters as well as clusters bound at support point defects (vacancies/divacancies). Our results clearly establish the role of the defective graphene supports in stabilizing the Pt_{13} nanoclusters at high CO–coverages, and in substantially reducing the barrier for CO oxidation reaction on supported clusters compared to unsupported ones.

Chapter 5 summarizes the most important results and concludes this thesis. This chapter also provides suggestions for future research directions in the field of optimal design of novel graphene–supported nanocatalysts.

In addition to the main topic of this thesis, presented in Chapters 1–5, this thesis also resolves certain outstanding issues relevant to the mechanical and electronic properties of other two-dimensional materials, as discussed in Appendices I-III. The findings of these studies have appeared in the following publications:

- J. Deng, I. Fampiou, J. Z. Liu, A. Ramasubramaniam, N. V. Medhekar, *Edge stresses of non-stoichiometric edges in two-dimensional crystals*, *Appl. Phys. Lett.* **2012**, 100, 251906

- C. Carpenter, A. M. Christmann, L. Hu, I. Fampiou, A. R. Muniz, A. Ramasubramaniam, D. Maroudas, *Elastic properties of graphene nanomeshes*, *Appl. Phys. Lett.* **2014**, 104, 141911

- P. Koskinen, I. Fampiou, A. Ramasubramaniam, *Density-functional tight-binding simulations of curvature-controlled valley polarization and band-gap tuning in bilayer* MoS_2, *Phys. Rev. Lett* **2014**, 112, 186802

CHAPTER 2

BINDING OF PT NANOCLUSTERS TO POINT DEFECTS IN GRAPHENE: ADSORPTION, MORPHOLOGY, AND ELECTRONIC STRUCTURE

2.1 Introduction

As discussed in Chapter 1, carbonaceous materials such as activated carbon and carbon black [12] and nanostructured forms of carbon such as nanotubes (CNT) [135] and graphite nanofibers,[166] are widely used as catalyst supports due to their high surface area, excellent electrical conductivity, resistance to corrosion, and structural stability. Carbon nanotubes, for example, exhibit greater stability and are better at suppressing catalyst aggregation than traditional carbon black supports.[82] More recently, a spate of advances in synthesizing graphene-based nanomaterials have opened up exciting avenues for the development of graphene-supported metal catalysts. [77, 84, 101, 148, 192] Preliminary experiments already indicate much promise for platinum-graphene nanocomposites as electrocatalysts in direct methanol fuel cells, [101, 192] proton-exchange membrane fuel cells (for oxygen reduction), [84] and hydrogen fuel cells. [148] When compared with standard Pt-carbon black catalysts, Pt-graphene composites display enhanced catalytic activity and tolerance to CO poisoning [101, 192] and, additionally, long-term stability toward sintering [84, 101, 192] with typical stable cluster sizes remaining below 5 nm. Moreover, these experiments have also demonstrated facile solution-processing methods for preparation of these catalyst materials. Thus, the overall outlook for Pt-graphene catalysts in transportation and portable electronics applications appears promising.

Pristine graphene is an sp^2-bonded carbon allotrope and is relatively inert. Metal clusters are typically weakly adsorbed on graphene and can diffuse fairly easily along the surface[49, 122] leading to eventual catalyst sintering. Therefore, in spite of its desirable properties such as excellent electrical conductivity and structural stability, pristine graphene is an unlikely candidate for a suitable support unless appropriate strategies can be devised to stabilize and immobilize clusters. Defect-engineering of graphene is one such possibility with promise; intuition suggests that undercoordinated C atoms should act as traps for metal atoms. Indeed, experiments clearly reveal that electron damage-induced point defects in graphene are very effective traps for diffusing atoms and clusters. [144] This was also noted in older work on highly-oriented pyrolitic graphite (HOPG) surfaces by Zoval *et al.* [199] who demonstrated that Pt nanoparticles nucleate preferentially at point defects and step edges on the graphite basal plane. Such defect-mediated anchoring of Pt nanoparticles is also expected to prevail in experimentally synthesized Pt-graphene composites, which are typically produced via solution processing of graphene oxide. Graphene oxide is known to contain lattice defects (vacancies, holes) and functional groups (carbonyls, epoxides, hydroxyls, etc.),[14, 96, 131] which can act as strong anchoring sites for Pt nanoparticles;[83, 84, 176] Other strategies such as boron [1, 80] or nitrogen doping [80] have also been proposed for enhancing the binding of Pt clusters to graphene.

From a computational perspective, the interaction of Pt clusters with graphene and carbon nanotubes has been extensively researched. [2, 19, 22, 30, 32, 33, 81, 83, 105, 117, 128, 129, 145, 176, 179]. Briefly, the following features of Pt-graphene interactions can be gleaned from these studies. First, Pt does not wet pristine graphene due to relatively high cohesive energy for Pt as compared to the Pt-C bond energy.[19, 117, 129] Consequently, Pt clusters on graphene are essentially three-dimensional structures for cluster sizes in excess of about ten atoms. Second, Pt clusters bind more strongly to defects (vacancies,[179] disclinations,[128] dopants,[2] edges,[81, 176] 5-8-5 reconstructed divacancies[83]) in graphene due to the formation of strong Pt-C bonds at the defect, which partially alleviates the disruption of the graphene sp^2 network. The electronic structure of the cluster is modified both due to bond formation as well as due to strains induced in the cluster. Third, there is a clear indication of charge transfer from the Pt cluster to the graphene support accompanied by a shift of the Pt d-band away from the Fermi level, which is greater in the presence of a support-defect.[30, 105, 128, 179] The binding energy of CO molecules, for example, is then found to decrease as one goes from an unsupported particle, to a supported one, to one on a defective support;[128] this provides a plausible explanation for the increased CO tolerance of Pt-graphene nanocomposites. Similarly, the presence of vacancies in the graphene substrate has been shown to enhance the stability of Pt_{13} nanoparticles on the graphene support while weakening the O_2 adsorption energy on the cluster; this effect can alter the catalytic activity of the nanoparticle toward oxygen reduction.[105] The presence of a defect at the graphene support was also found to increase the reactivity of Pt_4 clusters and reduce the barrier of catalyzed CO oxidation. [197]

There are also several studies on the adsorption and electronic properties of clusters of various other metals on graphene. Logsdail and Akola [112] investigated the adsorption of Au_{16} nanoclusters on bilayer graphene, with varying numbers of defects and different cluster orientations, and found that the adsorption energy increases with the number of the defects, leading to distortion of the initial structure. The cluster binds to the top layer of graphene creating Au-C bonds of metallic nature. As for the catalytic activity, those authors found that in the presence of defects, O_2 binding to the Au_{16} nanocluster was unfavorable in most cases. Lim *et al.* [104] studied the structural and electronic properties of graphene-supported Fe_{13} and Al_{13} nanoparticles and found strong binding at vacancies, which they attributed to significant hybridization between the metal cluster with the sp^2 dangling bonds of the carbon atoms. Recently, Liu *et al.* [109] investigated the properties of Pd nanoparticles on defective graphene as oxygen reduction catalysts. They found increased binding energy of Pd_{13} nanoclusters at vacancies and hybridization of the *dsp* states of Pd with the sp^2 dangling bonds of carbon, accompanied by a shift of the d-band center of the Pd nanoparticles away from the Fermi level. The defective graphene support was found to reduce the adsorption energies of O, OH and OOH on the Pd_{13} nanoparticles, which is directly related to electrocatalytic performance in oxygen reduction reactions.

The purpose of the computational study in this chapter is to provide a systematic investigation of the structural and electronic properties of Pt clusters in relation to the type of substrate defect that binds the cluster. Specifically, we are interested here in the hierarchy of the energetics of binding of Pt_n, (n=1, 2, 3, 4, 13) clusters to pristine graphene, vacancies, unreconstructed divacancies, pentagon-octagon-pentagon (5-8-5) reconstructed divacancies, and haeckelite (555-777) reconstructed divacancies in graphene. The divacancy is of particular interest as it presents the smallest defect in graphene with non-trivial reconstructions, namely the 5-8-5 and 555-777 reconstructions.[91, 92] Apart from binding energetics of specific cluster geometries, we are also interested in identifying low-energy isomers of these clusters and the possible correlation between the structure of a Pt_n cluster with the type of binding defect. These substrate-induced structural modifications are expected to influence the electronic structure and activity of the cluster. Such low-energy structures have been identified fairly systematically for small Pt clusters on pristine graphene and at vacancies;[19, 129] comparisons to existing literature will be presented in Section 2.3. There are no systematic studies at divacancies and reconstructed divacancies to the best of our knowledge. At best, there have been investigations of binding of a Pt_6 cluster [83] and a Pt_{27} cluster [176] to a 5-8-5 defect; however, neither study appears to have undertaken a systematic optimization of the cluster shape beyond structural relaxations starting from a specific initial guess. Indeed, this appears to be the prevalent situation even in other studies of binding of Pt_{13} clusters to pristine graphene as well as to vacancy defects wherein the clusters have typically been assumed to be of icosahedral (I_h) symmetry prior to relaxation.[30, 32, 128] Okazaki-Maeda *et al.* [129] have used a few other initial guesses such as icosahedral, cuboctahedral (O_h), planar, and layered Pt_{13} clusters in their study on binding to pristine graphene; while the bias from initial conditions is still to be expected, their study nevertheless provides more insight into the classes of low-energy structures that might be expected. Also, while structural relaxation can certainly induce significant distortions in the cluster shape, typical relaxation algorithms (steepest descent, conjugate gradient, etc.) are only guaranteed to find local minima in the vicinity of the initial guess rather than a global minimum. Furthermore, while there is still some debate about the minimum energy structures even for unsupported clusters, density functional theory studies [25, 89, 113, 180] clearly indicate that Pt_{13} clusters tend to adopt low-symmetry, open structures rather than high-symmetry compact ones; the latter (I_h, O_h symmetry) can be about 2 eV higher in energy than their low-symmetry counterparts. Hence, we suggest that studies of high-symmetry supported clusters—even after structural relaxation—might not convey meaningful information about the electronic structure and activity of realistic Pt clusters. To address this issue in more detail, we study both relaxed high-symmetry supported clusters (on a variety of substrate defects) as well as low-symmetry ones generated by molecular dynamics (MD) annealing, and demonstrate that the annealed structures are significantly more stable over the relaxed high-symmetry ones. Finally, we also present a detailed electronic structure analysis of the Pt_{13} clusters bound at various defects and correlate cluster–substrate charge transfer as well as cluster d-band shifts with the strength of binding to the defect.

The computational methodology employed in this study is described in Section 2.2. Results and discussion on cluster binding energetics, structural analyses, and electronic structure are presented in Section 2.3. The main conclusions are summarized in Section 2.4.

2.2 Computational Details

We employ a combination of density functional theory (DFT) and empirical potential (EP) simulations at the level of Tersoff-Brenner potentials. EP simulations allow for extended molecular dynamics (MD) annealing runs and sampling to generate candidate low-symmetry structures for further DFT studies as described in detail below. We present the details of the DFT calculations first, followed by the EP calculations.

DFT calculations are performed in the Vienna *Ab Initio* simulation package (VASP). [86]. The projector-augmented wave (PAW) method [18, 88] is used to describe the core and valence electrons; the PAW potentials are derived from fully relativistic atomic calculations. The Perdew-Burke-Ernzerhof [132] form of the Generalized-Gradient Approximation is employed to describe electron exchange and correlation. All calculations are performed on a 6×6 graphene supercell (72 atoms) with periodic boundary conditions; periodic images are separated by 18 Å of vacuum normal to the sheets to prevent spurious image interactions. A kinetic energy cutoff of 400 eV is used in all simulations and the Brillouin zone is sampled using a 5 x 5 x 1 Γ-centered k-point mesh. Structural relaxations are performed using a conjugate gradient algorithm until forces on all atoms are below 0.01 eV/Å. To accelerate electronic convergence, a second-order Methfessel-Paxton[121] smearing of the Fermi surface is employed with a smearing width of 0.05 eV. All calculations are spin-polarized. For Pt clusters in vacuum, calculations are performed in a large supercell with Γ-point sampling only.

EP calculations are performed in the LAMMPS simulation package [136] with a Tersoff-Brenner style potential for Pt-C developed by Albe *et al.*[5] The EP calculations are performed for the same 72-atom graphene sheet that was used in the entire set of the DFT calculations; the only difference of note is that the graphene supercell employed here is constructed at the equilibrium C-C bond length of 1.45 Å for the Tersoff-Brenner potential as opposed to the DFT value of 1.42 Å. Structural relaxations, analogous to the DFT studies, are performed with conjugate gradient minimization and a tolerance of 10^{-4} eV/Å on the N-dimensional force vector. In addition to structural relaxation, supported 13-atom Pt clusters on the various defective graphene substrates are also subjected to MD annealing in a canonical (NVT) ensemble. For these annealing studies, the system is initially thermalized at 1500 K for 50 ps and gradually cooled to 1 K over another 50 ps. Structural data are then gathered over 2.5 ps at 1 K.The MD time-step is set to 1 fs. The system is then reheated to 1500 K and the annealing process repeated. This entire heat–anneal–gather procedure is repeated eight times to allow the system to sample the energy landscape more extensively and to gather reasonable statistics. The *lowest* energy structures are then imported into VASP for further structural relaxation and electronic structure analysis; the lattice vectors and atomic positions must be rescaled in this step to account for the slight mismatch of the EP (1.45 Å) and DFT (1.42 Å) C-C bond length. This procedure allows us to generate low-symmetry, low-energy structures at minimal computational cost, which can then be studied in greater detail with DFT. Of course, it is entirely possible that the EP potential energy surface is quite different from the DFT one, which implies that an optimal EP structure might not be close to optimal in DFT. Also, there is no guarantee that annealing brings us close to a global minimum. Nevertheless, as we will see later in this chapter, this procedure is sufficient to identify structures that are favored by several eV over those obtained from structural relaxation of high-symmetry shapes alone.

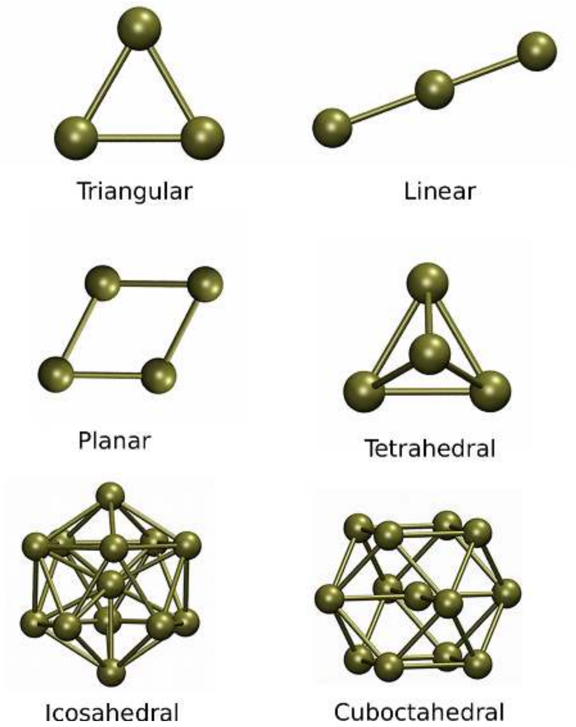

Figure 2.1: DFT-optimized cluster geometries in vacuum for linear and triangular Pt_3 clusters; planar and tetrahedral Pt_4 clusters; and icosahedral (I_h) and cuboctahedral (O_h) Pt_{13} clusters.

As far as Pt clusters are concerned, for high-symmetry structures we consider the Pt monomer; dimer; linear and triangular Pt trimers; planar and tetrahedral Pt tetramers; and I_h and O_h Pt_{13} clusters. The DFT-optimized vacuum structures for Pt_3, Pt_4, and Pt_{13} clusters are displayed in Figure 2.1. For substrates, we consider pristine (defect-free) graphene as well as defective graphene with a single vacancy, an unreconstructed divacancy, a 5-8-5 reconstructed divacancy, and a 555-777 reconstructed divacancy, which are displayed in Figure 2.2.

For both DFT and EP calculations we report the adsorption energy (E_{ad}) and the formation energy (E_f) of the clusters. The adsorption energy E_{ad} of the Pt_n cluster is defined as

$$E_{ad} = E_{C_m+Pt_n} - E_{C_m} - E_{Pt_n} , \tag{2.1}$$

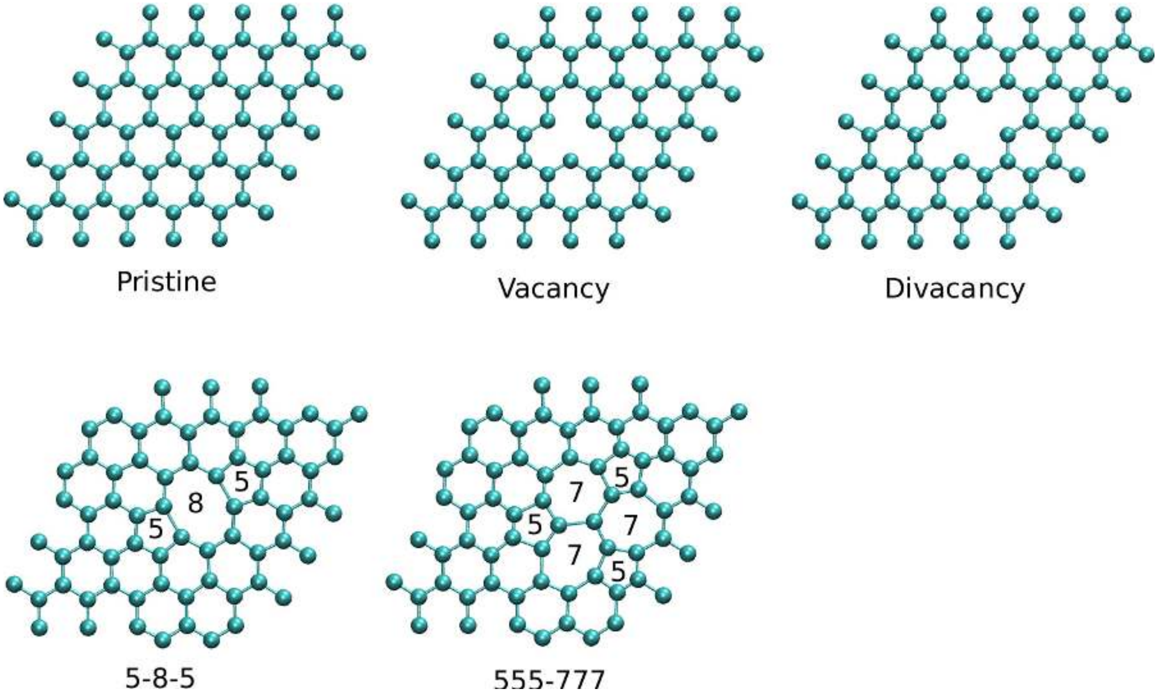

Figure 2.2: Defect-free and defective graphene substrates employed in this study. Pentagons, heptagons, and octagons associated with divacancy reconstructions are indicated in the figure.

where $E_{C_m+Pt_n}$, E_{C_m} and E_{Pt_n} are the total energies of the Pt_n–graphene system, the graphene sheet of m carbon atoms, and the $\mathrm{Pt_n}$ cluster in vacuum. The formation energy is defined as

$$E_f = E_{C_m+Pt_n} - mE_C - nE_{Pt}\,, \tag{2.2}$$

where $E_{C_m+Pt_n}$ is the total energy of the Pt_n–graphene system, and E_C and E_{Pt} are the energies of a C atom in graphene and a Pt atom in vacuum, respectively. As defined, a more negative value of E_{ad} signifies stronger binding of a cluster to the support. Similarly, a more negative value of E_f signifies greater thermodynamic stability of the structure with respect to the reference states of its individual constituents. For adsorption energy calculations, the reference energy of the Pt_n, (n=1, 2, 3, 4) cluster is taken to be that of its corresponding high-symmetry structure (Figure 2.1) in vacuum. Supported Pt_{13} clusters can often display final relaxed shapes that are significantly different from their high-symmetry, vacuum structures (in spite of this being the initial condition for relaxation). For low-symmetry Pt_{13} clusters generated by MD annealing on the graphene support, there is no correlation whatsoever with the high-symmetry vacuum structures. Therefore, there is some ambiguity in defining the reference energy of the Pt_{13} cluster in the adsorption energy calculation. We adopt the simple strategy of removing the carbon atoms from the fully relaxed/annealed Pt-graphene structure and relaxing the residual Pt cluster alone in vacuum. This cluster energy is then chosen as the reference for computing the adsorption energy; this definition is not unique and other equally valid choices can be made. The formation energy clearly does not suffer from any such ambiguities.

2.3 Results and discussion

2.3.1 Adsorption of Pt atoms

First, we examine the adsorption of a single Pt-atom on the five different graphene substrates. In each case, there are several stable adsorption sites (hollow/top/bridge sites) that can be rendered inequivalent due to substrate reconstructions. For brevity, we only report adsorption and formation energies along with C-Pt bond length for minimum energy structures in Table 2.1; corresponding atomic structures (from DFT) are displayed in Figure 2.3. On pristine graphene, a single Pt atom is adsorbed most strongly on the bridge site (B site), which is consistent with several previous studies [19, 22, 30, 35, 129, 175] and it is located at 1.97 Å above the graphene layer. This result is in good agreement with the reported values from Błoński *et al.*[19] and Okazaki-Maeda *et al.*[129]. At a vacancy, the Pt atom essentially binds as a substitutional that is displaced by 1.12 Å out of the graphene plane due to the greater length of C-Pt bond as compared to a C-C bond. At an unreconstructed divacancy, the Pt atom occupies a “cross” configuration and is again slightly displaced out of the graphene plane by 0.31 Å. These observations are in agreement with DFT calculations by Krasheninnikov *et al.*[85] Also, as noted by those authors, our DFT results also confirm that the Pt atom is bound less strongly to the divacancy due to weaker interactions with the ligand bonds. This is not reflected in the EP calculation though, which predicts that the Pt atom binds more strongly to the divacancy rather than the vacancy. [1] The 5-8-5 and 555-777 defects bind the Pt atom more weakly than the unreconstructed divacancy but more strongly than pristine graphene. Interestingly, both the unreconstructed divacancy and 5-8-5 structures in Figure 2.3 produce identical adsorption configurations after the DFT calculation even though the initial configurations of the graphene sheet are different (unreconstructed vs. reconstructed). The Pt atom thus appears to break the 5-8-5 reconstruction. This is not observed for the 555-777 substrate case, which is known to be a lower energy (more stable) reconstruction than the 5-8-5 defect [91, 92] and is therefore less prone to unreconstructing. Finally, an examination of the formation energies shows that with the exception of the pristine sheet, the defective sheets with adsorbed Pt atoms are all thermodynamically less stable with respect to their constituents. This is a reflection of the high defect formation energy in each case, which is not adequately compensated by formation of bonds with the single Pt atom.

2.3.2 Adsorption of Pt dimers

Next, we consider adsorption of the Pt_2 cluster (dimer) on defect-free and defective graphene substrates. We report adsorption and formation energies only for the lowest energy structures in Table 2.2 and their corresponding atomic structures (from DFT) in Figure 2.4. For pristine graphene, we find that the most stable configuration is a vertically oriented dimer bound at a bridge site. The Pt-Pt (DFT) bond length for the adsorbed dimer is elongated to 2.38 Å as compared to the gas phase bond length of

---

[1] This discrepancy from the EP calculation persists even in tests on much larger graphene sheets (1500 atoms) suggesting deficiencies in the potential itself; size-effects can be conclusively ruled out.

Table 2.1: Optimal adsorption energies, formation energies, C-Pt bond lengths (d_{C-Pt}), and Pt-Pt bond lengths (d_{Pt-Pt}) for single Pt atom on pristine graphene, single vacancy, unreconstructed divacancy, 5-8-5 reconstructed divacancy, and 555-777 reconstructed divacancy. EP values are in parentheses.

Substrate	E_{ad} (eV)	E_f (eV)	d_{C-Pt} (Å)
pristine	-1.57 (-1.99)	-1.57 (-1.99)	2.10 (2.06)
vacancy	-7.45 (-6.68)	0.54 (-1.37)	1.94 (1.98)
divacancy	-6.97 (-8.60)	0.71 (-1.51)	1.98 (2.01)
5-8-5	-6.12 (-6.94)	0.71 (-1.51)	1.99 (2.01)
555-777	-2.38 (-2.27)	4.71 (2.28)	2.06 (2.07)

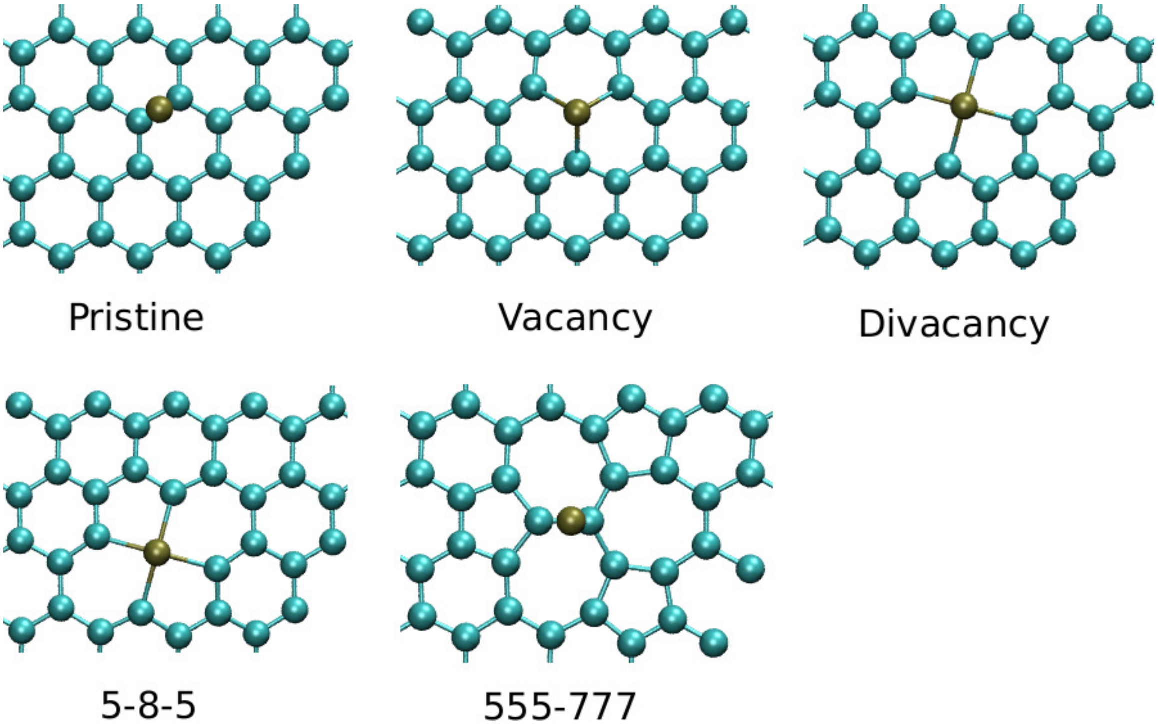

Figure 2.3: Low-energy DFT configurations for adsorption of a Pt atom on graphene. Cyan and gold spheres represent C and Pt atoms, respectively.

2.33 Å. These results are in agreement with the study by Błoński and Hafner; [19] the horizontal adsorption configuration (Pt atoms bound at diametrically opposite near-on-top sites of the hexagon), which is predicted to be the lowest energy structure by

Okazaki-Maeda *et al.*,[129] is actually adsorbed less weakly by 0.36 eV as compared to the vertical dimer.

For adsorption at a vacancy or divacancy, one Pt atom is consistently bound at an on-top site (slightly displaced) whereas the second Pt atom occupies a position similar to that occupied by a single Pt atom bound at the defect (substitutional/cross configuration displaced out of the graphene plane; see Section 2.3.1). The dimer is bound more strongly to the single vacancy rather than to the unreconstructed divacancy, as was the case for Pt_1. Similarly the 5-8-5 and 555-777 defects bind the dimer more strongly than pristine graphene but less strongly than either the vacancy or the divacancy. For the 5-8-5 case, we observe as in the case of the single Pt atom that the dimer breaks the reconstruction; the Pt atoms are situated at bridge sites of atoms shared by the pentagon and octagon. Clearly, this is a local minimum en route to the dimer–divacancy configuration. The empirical potential once again reverses the relative ordering of adsorption energies at the vacancy and divacancy in comparison with DFT. For adsorption at the 555-777 defect, the most stable configuration is similar to the one we found for the pristine graphene case and consists of a vertically oriented dimer bound at the bridge site between the pentagon and heptagon of the 555-777 defect. It is interesting to note that in the cases that there are no dangling bonds (pristine and 555-777 substrate) the most stable adsorption configuration is the upright dimer while for the other three substrates the dimer binds to the substrate in a manner that passivates the dangling C bonds. Thermodynamically, all structures with the exception of the 555-777 case are stable with respect to their individual components.

2.3.3 Adsorption of Pt trimers

The Pt_3 cluster (trimer) has two non-equivalent structures, namely the linear and the triangular configuration as shown in Figure 2.1. We considered adsorption

Table 2.2: Optimal adsorption energies, formation energies, C-Pt bond lengths (d_{C-Pt}), and Pt-Pt bond lengths (d_{Pt-Pt}) for Pt dimers on pristine graphene, single vacancy, unreconstructed divacancy, 5-8-5 reconstructed divacancy, and 555-777 reconstructed divacancy. EP values are in parentheses.

Substrate	E_{ad} (eV)	E_f (eV)	d_{C-Pt} (Å)	d_{Pt-Pt} (Å)
pristine	-0.78 (-1.94)	-4.58 (-5.62)	2.25 (2.07)	2.38 (2.39)
vacancy	-7.26 (-6.93)	-3.07 (-5.30)	1.96, 2.01(1.96, 1.97)	2.53 (2.63)
divacancy	-6.40 (-8.66)	-2.52 (-5.25)	1.97, 2.04 (1.96, 2.01)	2.56 (2.72)
5-8-5	-4.14 (-7.34)	-1.11 (-5.58)	1.92, 2.00 (1.94)	2.51 (2.62)
555-777	-2.43 (-2.21)	0.86 (-1.35)	2.07 (2.07)	2.33 (2.39)

of these two structures both parallel and perpendicular to the graphene substrates. Adsorption and formation energies for the most stable structures as well as average Pt-C and Pt-Pt bond lengths are reported in Table 2.3 and their corresponding atomic structures (from DFT) displayed in Figure 2.5. In none of the cases is the linear trimer chain energetically preferred. For pristine graphene, we find that the triangular configuration with two Pt atoms bound to the substrate is the most stable one in agreement with other studies. [19, 129] The basal Pt atoms are bound to the substrate at positions intermediate between on-top and bridge sites in agreement with Błoński and Hafner; [19] and in disagreement with Okazaki-Maeda *et al.*,[129] which seems to favor bridge sites. At a vacancy, one atom at the vertex of the triangle is bound at the site of the missing C atom with an out-of-plane displacement as before; the second Pt atom occupies a bridge site; the third Pt atom is directly bonded only to the Pt atoms. At a divacancy, two Pt atoms of the cluster passivate the dangling C bonds; the third Pt atom is bound only to the other Pt atoms. The 5-8-5 defect reconstruction is broken by the Pt trimer. The cluster is now an inverted triangle with one atom bound at a cross configuration while the other two Pt atoms occupy on-top sites. This configuration is higher in energy than the trimer–divacancy configuration and represents a local minimum en route to the latter structure. At the 555-777 defect,

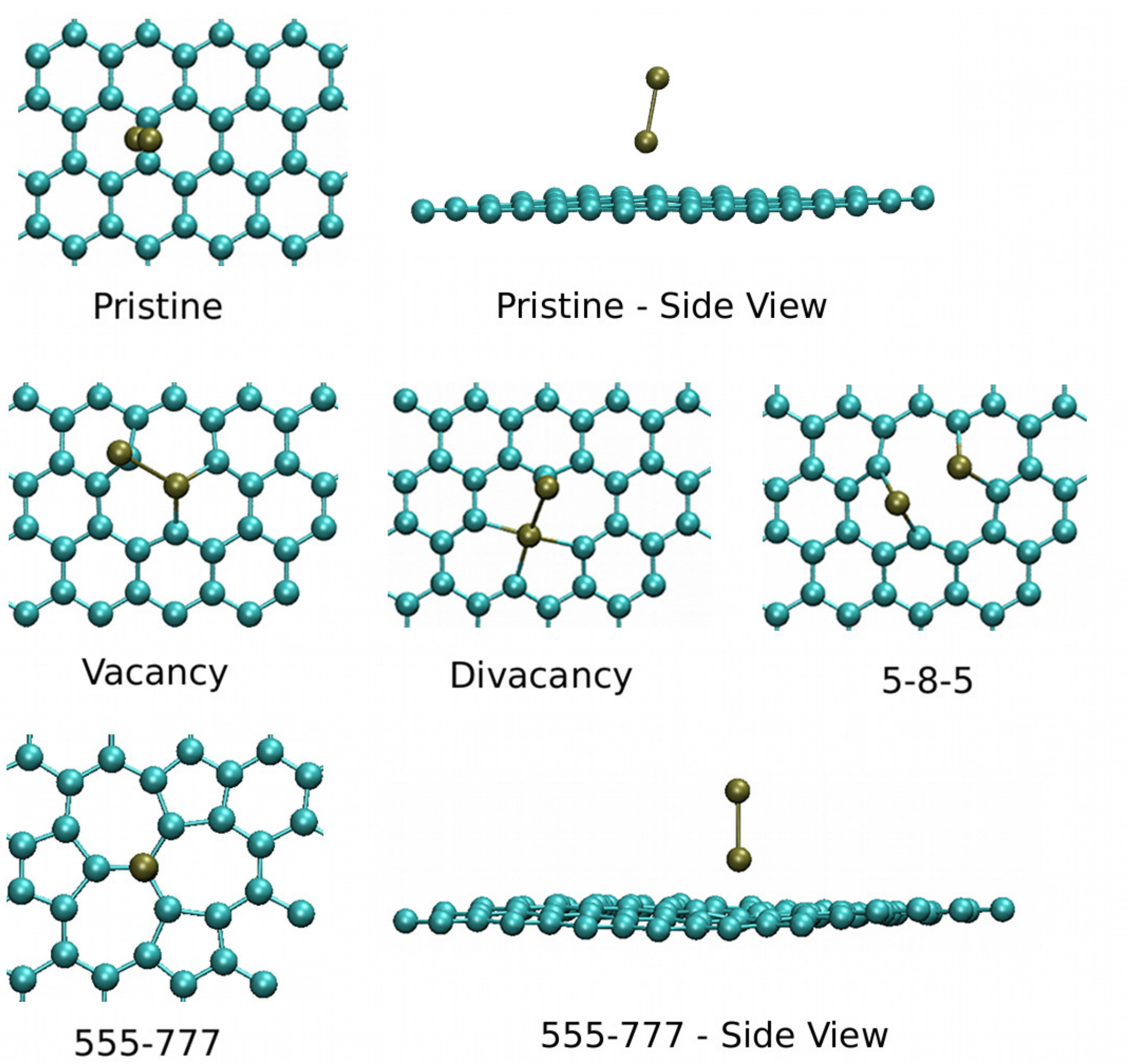

Figure 2.4: Low-energy DFT configurations for Pt dimers on graphene. Cyan and gold spheres represent C and Pt atoms, respectively.

the cluster is bound most strongly to the central C atom at only one vertex with a Pt-C bond length equal to 2.04 Å and adopts a tilted configuration with respect to the basal plane. As before, the empirical potential reverses the energetic ordering of binding at the vacancy and divacancy.[1] Finally, all structures are thermodynamically stable with respect to their individual components.

Table 2.3: Optimal adsorption energies, formation energies, average C-Pt bond lengths ($\langle d \rangle_{C-Pt}$), and average Pt-Pt bond lengths ($\langle d \rangle_{Pt-Pt}$) for Pt trimers on pristine graphene, single vacancy, unreconstructed divacancy, 5-8-5 reconstructed divacancy, and 555-777 reconstructed divacancy. EP values are in parentheses.

Substrate	E_{ad} (eV)	E_f (eV)	$\langle d \rangle_{C-Pt}$ (Å)	$\langle d \rangle_{Pt-Pt}$ (Å)
pristine	-1.35 (-2.54)	-8.64 (-10.06)	2.22 (2.06)	2.49 (2.61)
vacancy	-7.61 (-6.52)	-6.91 (-8.73)	1.96 (2.02)	2.54 (2.59)
divacancy	-6.33 (-7.95)	-5.94 (-8.38)	1.96 (2.01)	2.48 (2.64)
5-8-5	-5.54 (-7.50)	-6.00 (-9.59)	2.05 (1.99)	2.57 (2.73)
555-777	-5.15 (-2.05)	-5.34 (-5.02)	2.04 (2.07)	2.50 (2.50)

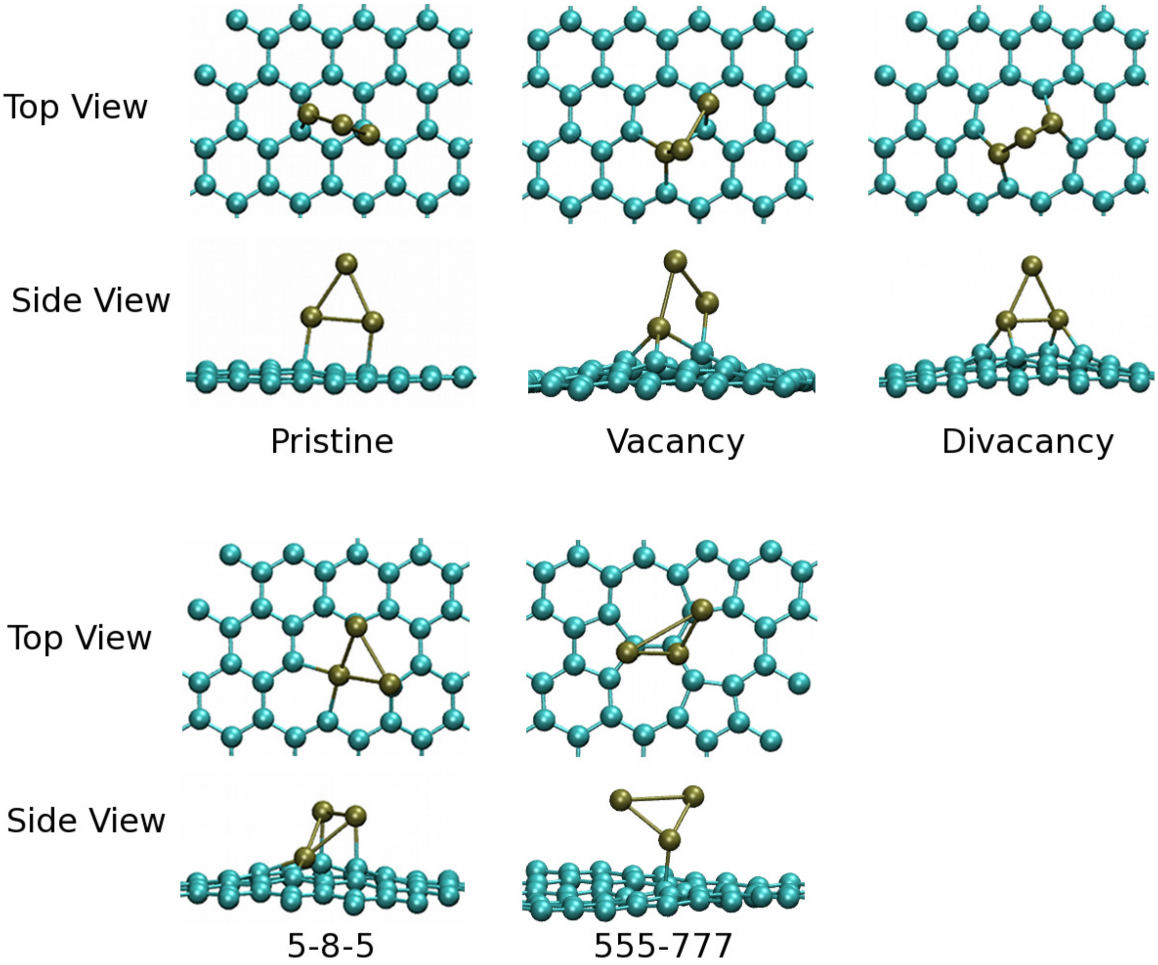

Figure 2.5: Low-energy DFT configurations for Pt trimers on graphene. Cyan and gold spheres represent C and Pt atoms, respectively.

2.3.4 Adsorption of Pt tetramers

For the Pt tetramer (Pt_4), we examined the planar and tetrahedral pyramidal structures as shown in Figure 2.1. Adsorption and formation energies and the average C-Pt and Pt-Pt bond lengths for the most stable structures are reported in Table 2.4 and their corresponding atomic structures (from DFT) displayed in Figure 2.6. Although the planar structure is energetically preferred in the gas phase (in agreement with Błoński and Hafner [19]) by 13 meV/atom, the tetrahedral geometry is found to be most strongly adsorbed on pristine graphene (in agreement with Okazaki-Maeda *et al.*,[129]). The same situation prevails at a vacancy, where the cluster binds as an inverted tetrahedron with one vertex occupying the same position as the missing C atom, albeit with an out-of-plane displacement as in the previous cases. When adsorbed at the divacancy as well as the 5-8-5 reconstruction, the cluster is more like a buckled rhombus with one vertex occupying a cross configuration and two other atoms occupying on-top sites. Note that the divacancy and 5-8-5 structures in Figure 2.6 are simply rotated by approximately 90° with respect to each other. The 5-8-5 reconstruction is once again broken by the cluster although this time the system does not seem to fall into a local minimum en route to the tetramer–divacancy configuration. At the 555-777 defect, the cluster resembles a buckled rhombus although the buckling is less severe than the divacancy and 5-8-5 cases. The tetramer is bound at only one vertex to the centermost C atom of the 555-777 reconstruction. Once again, the empirical potential reverses the energetic ordering of binding at the vacancy and divacancy. All structures are thermodynamically stable with respect to their individual components.

The Pt tetramer is particularly interesting as it presents the smallest cluster size for which there is a non-trivial interplay between cluster morphology and substrate structure. In contrast, the monomer and dimer are relatively trivial cases; the trimer always prefers triangular morphologies over linear ones. The Pt_4 cluster is remarkable in that the adsorbed morphologies are clearly derived from two distinct gas-phase isomers, namely, a planar rhombus and a tetrahedron, the preferred morphology being a function of substrate binding site. These site-dependent morphological preferences could play an important role in determining the catalytic activity of such small clusters.

Table 2.4: Optimal adsorption energies, formation energies, average C-Pt bond lengths ($\langle d \rangle_{C-Pt}$), and average Pt-Pt bond lengths ($\langle d \rangle_{Pt-Pt}$) for Pt tetramers on pristine graphene, single vacancy, unreconstructed divacancy, 5-8-5 reconstructed divacancy, and 555-777 reconstructed divacancy. EP values are in parentheses.

Substrate	E_{ad} (eV)	E_f (eV)	$\langle d \rangle_{C-Pt}$ (Å)	$\langle d \rangle_{Pt-Pt}$ (Å)
pristine	-1.13 (-1.63)	-12.07 (-13.12)	2.14 (2.07)	2.60 (2.62)
vacancy	-7.27 (-5.51)	-10.22 (-11.69)	1.97 (1.99)	2.61(2.59)
divacancy	-7.06 (-9.26)	-10.37 (-13.80)	2.03 (1.99)	2.53 (2.58)
5-8-5	-6.01 (-7.4)	-10.17 (-13.59)	2.01(2.04)	2.49 (2.52)
555-777	-5.33 (-3.35)	-9.23 (-10.43)	2.04 (2.10)	2.47 (2.50)

2.3.5 Adsorption of Pt_{13} clusters

Finally, we consider the case of a Pt_{13} cluster, which represents the smallest magic cluster according to the geometric shell model.[15, 157] Among its high-symmetry shapes are the icosahedron (I_h) and the cuboctahedron (O_h). These compact shapes are not global minima though, as has been shown by several authors; [25, 89, 113, 180] instead, there exist several low-symmetry, open structures that are more energetically preferred. The task of systematically finding low energy isomers is already a computationally tedious one for unsupported clusters, let alone supported ones. Rather than attempting to comprehensively catalog low-energy supported clusters, we will simply examine a few structures obtained here from MD annealing and contrast these with local minima obtained for adsorption of high-symmetry structures.

First, I_h and O_h clusters were introduced in the vicinity of the graphene sheet and the total energy minimized using a conjugate gradient algorithm so as to find a

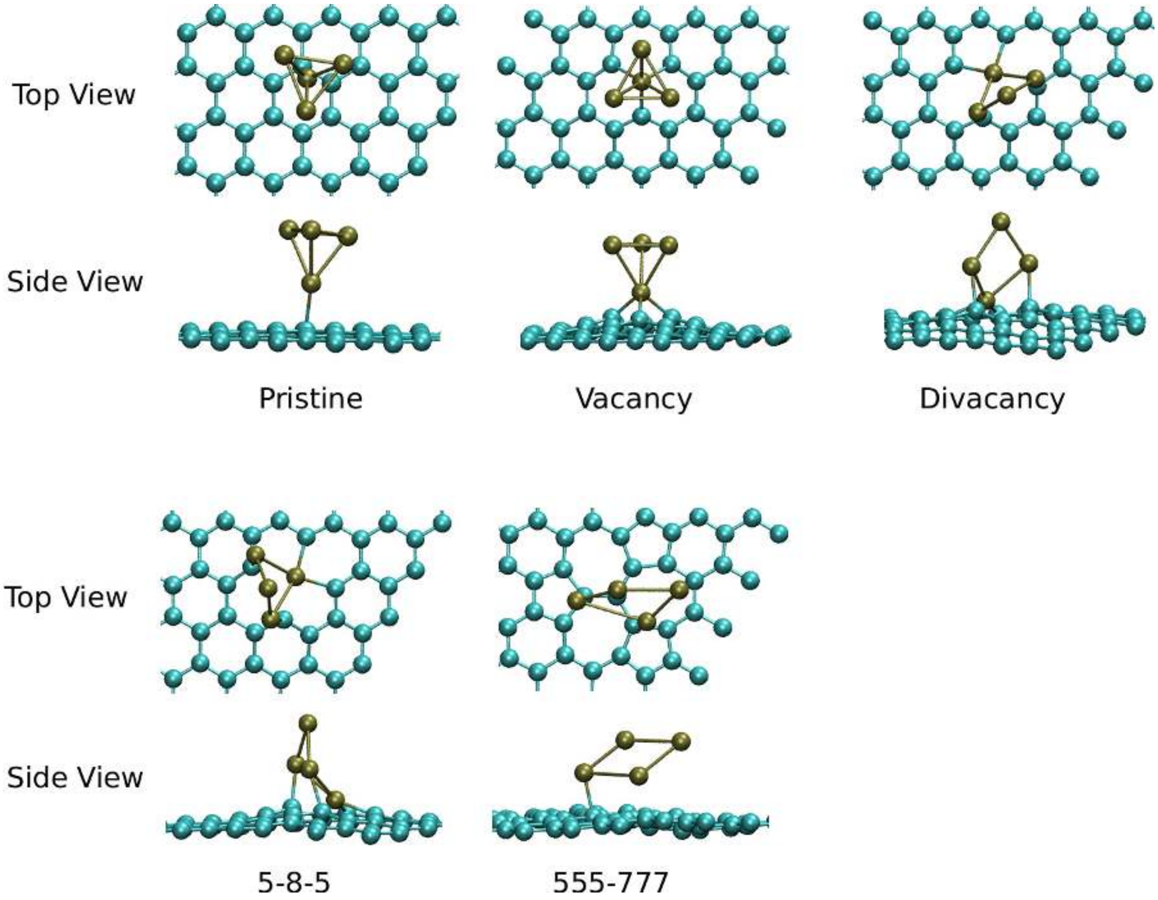

Figure 2.6: Low-energy DFT configurations for Pt tetramers on graphene. Cyan and gold spheres represent C and Pt atoms, respectively.

local minimum. Planar clusters were already shown by Okazaki-Maeda *et al.* [129] to be energetically unfavorable and are not considered here. (Test calculations were essentially in agreement with that work.) The clusters were introduced at different orientations with respect to the sheet (e.g., with a triangular or square face parallel to the sheet, a vertex closest to the sheet, etc.). The lowest energy structures that were obtained from energy minimization with DFT are displayed in Figure 2.7; adsorption and formation energies are reported in Table 2.5. As seen from these data, the Pt clusters bind most strongly to the unreconstructed divacancy followed by the 5-8-5 defect. The latter once again unreconstructs upon cluster adsorption. We note that for these two cases, the initial structure of the cluster was icosahedral, but the relaxed structure bears little resemblance to an icosahedron (see Figure 2.7), unlike the relaxed structures on other substrates where there is some resemblance to the starting structure (I_h or O_h as appropriate). Thus, even structural relaxation to a local minimum in the presence of certain substrate defects can induce severe morphological changes in the cluster. We also note that the DFT and EP data are now in qualitative agreement with respect to the relative ordering of adsorption energies. This gives us some confidence in using EP calculations as a preliminary step to generate low-energy candidates for additional investigation with DFT.

Table 2.5: Optimal adsorption energies, formation energies and average Pt-Pt bond lengths ($\langle d \rangle_{Pt-Pt}$) for Pt_{13} clusters on pristine graphene, single vacancy, unreconstructed divacancy, 5-8-5 reconstructed divacancy, and 555-777 reconstructed divacancy. Results are reported both for structural relaxation of high-symmetry clusters as well as annealed and relaxed clusters. EP results are in parentheses; for Annealing+Relaxation, the EP energies and bond lengths are averaged over eight different low energy structures.

	Relaxation alone			Annealing + Relaxation		
Substrate	E_{ad} (eV)	E_f (eV)	$\langle d \rangle_{Pt-Pt}$ (Å)	E_{ad} (eV)	E_f (eV)	$\langle d \rangle_{Pt-Pt}$ (Å)
pristine	0.25 (-3.11)	-49.18 (-54.67)	2.59 (2.61)	-0.84 (-3.72)	-49.96 (-55.20)	2.57 (2.53)
vacancy	-4.67 (-5.86)	-44.64 (-52.48)	2.58 (2.56)	-7.29 (-7.84)	-48.32 (-55.14)	2.56 (2.56)
divacancy	-6.59 (-9.58)	-48.50 (-54.89)	2.59 (2.58)	-7.28 (-10.20)	-49.07 (-55.67)	2.57 (2.59)
5-8-5	-6.28 (-7.33)	-49.03 (-54.30)	2.55 (2.56)	-6.56 (-8.09)	-49.31 (-55.36)	2.55 (2.54)
555-777	-2.07 (-4.66)	-44.40 (-50.93)	2.58 (2.59)	-2.79 (-5.85)	-45.20 (-53.15)	2.55 (2.55)

Thereafter, we took the relaxed clusters and subjected them to a MD annealing schedule as described in Section 2.2. Some of the morphologies of the clusters obtained from this procedure are displayed in Figure 2.8; the adsorption and formation energies after annealing and relaxation are displayed in Table 2.5. There are other near-degenerate structures that are not displayed here but are accounted for in constructing the plot of the adsorption energy versus the average Pt-Pt bond length in Figure 2.9 (discussed further below). It is immediately apparent that the clusters bear no resemblance to their high-symmetry I_h or O_h counterparts. Instead, these are low-

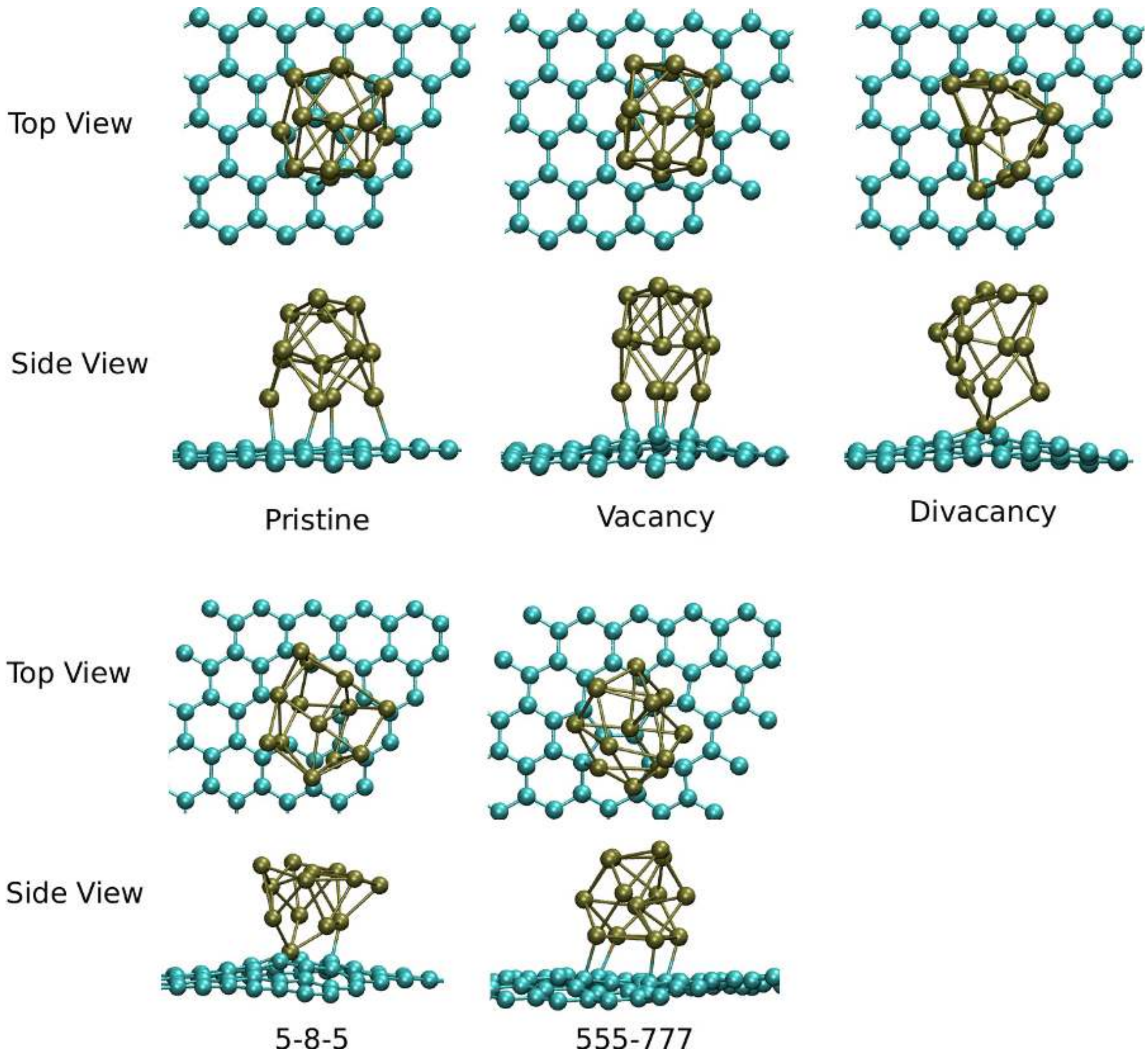

Figure 2.7: Low-energy configurations obtained by DFT structural relaxation of Pt_{13} clusters on graphene. Cyan and gold spheres represent C and Pt atoms, respectively.

symmetry, open shapes that are more strongly adsorbed (by several eV in some cases) and are thermodynamically more stable than the structures obtained from relaxation alone. The vacancy and the unreconstructed divacancy are seen to be the strongest binding defects, differing by only 0.01 eV in their binding energies. Interestingly, for both the vacancy and divacancy, the cluster has one vertex atom in a near-substitutional or cross configuration, respectively. The rest of the cluster is supported on this basal atom leaving a large number of under-coordinated Pt

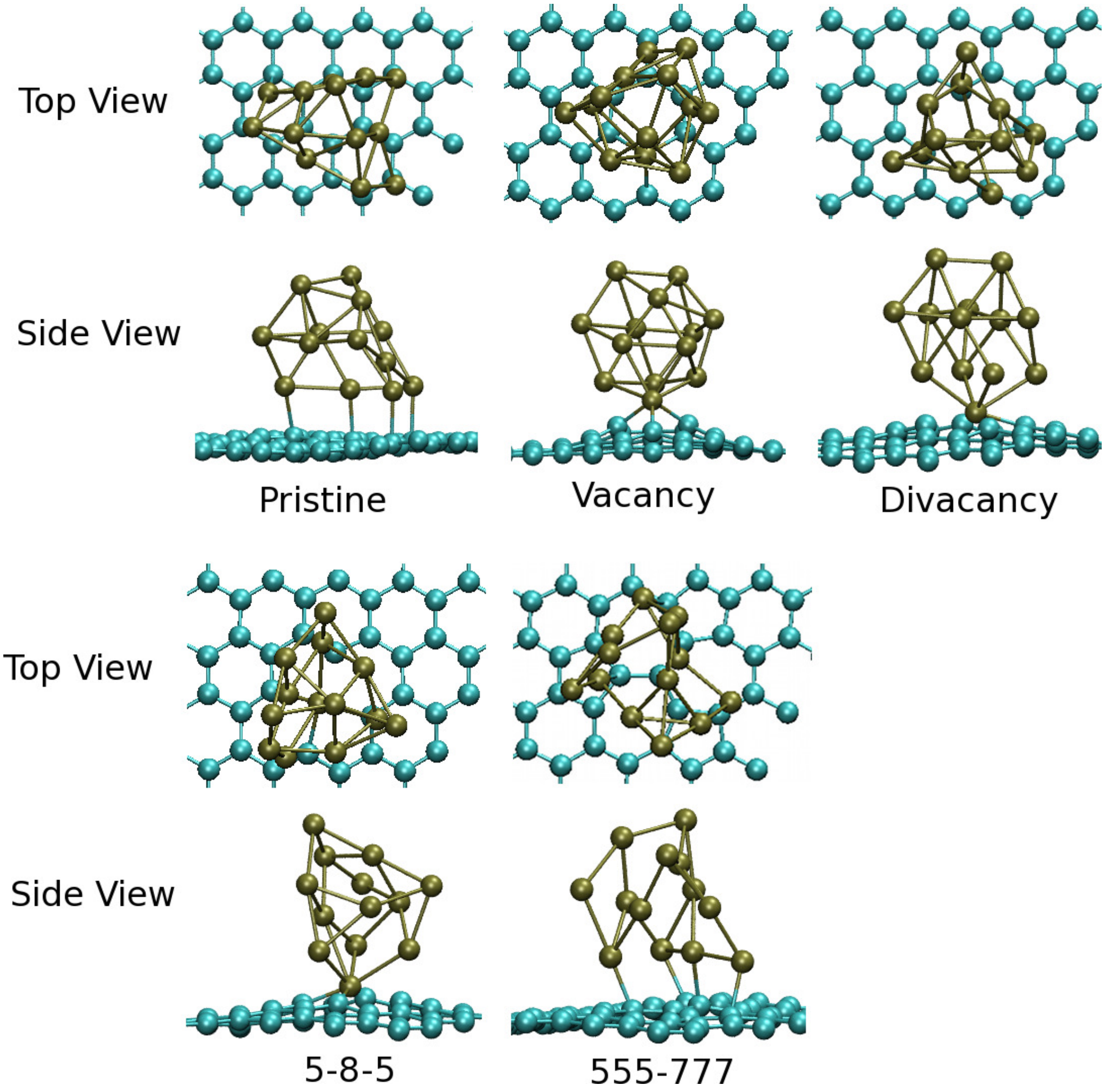

Figure 2.8: Selected low-energy configurations obtained by DFT structural relaxation of EP-based MD annealing of Pt_{13} clusters on graphene. Cyan and gold spheres represent C and Pt atoms, respectively.

atoms. For the other cases, in contrast, there are more Pt-C bonds, consequently, with fewer undercoordinated Pt atoms. The number of undercoordinated surface atoms is directly related to the number of active surface sites for catalytic reactions. Thus, these results establish one possible effect at the morphological level of the

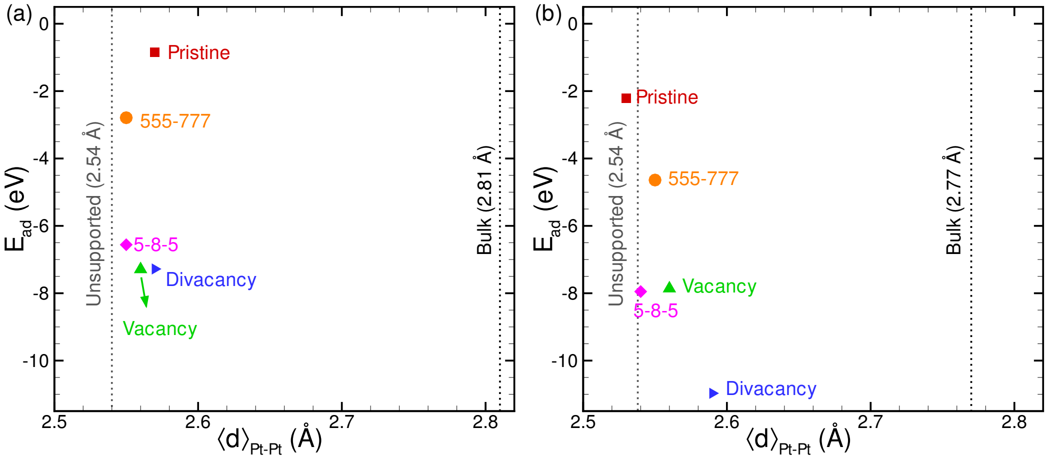

Figure 2.9: (a) Adsorption energy (E_{ad}) versus average bond length ($\langle d \rangle_{Pt-Pt}$) from DFT relaxation of the lowest-energy Pt_{13} clusters on graphene supports obtained after EP-based MD annealing. Vertical dotted lines indicate the average bond lengths for bulk Pt and for unsupported clusters (annealed clusters removed from graphene substrate and relaxed). (b) E_{ad} versus $\langle d \rangle_{Pt-Pt}$ obtained after averaging over eight different low energy structures obtained with the EP-based MD annealing schedule. (Error bars are much too small to be visible on this scale and are omitted.) The corresponding data are in Table 2.5.

substrate defect on potential catalytic activity of the cluster, namely, controlling the extent of undercoordination of Pt atoms.

To quantify the morphological changes in the low-symmetry clusters, we display in Figure 2.9 the adsorption energy versus the average Pt-Pt bond length of the Pt_{13} clusters adsorbed on the five different graphene substrates. The average bond lengths for bulk Pt and the unsupported clusters are also indicated in the figure; the smaller average bond length in the latter case is to be expected due to the significant degree of undercoordination of Pt atoms in these small clusters as compared to bulk Pt. The DFT data [Figure 2.9 (a)] are from relaxation of the lowest energy structures obtained from the initial EP-based MD annealing step; the EP data [Figure 2.9 (b)] are obtained by averaging[2] over eight different low-energy configurations sampled

---

[2] The energies $E_{C_m+Pt_n}$ and E_{Pt_n} should be replaced by their averages in Eqs. 1 and 2.

over the course of the annealing schedule. We see from Figure 2.9 that the supported clusters all have slightly larger average bond lengths than the unsupported ones. We attribute this to the formation of Pt-C bonds, which decreases the degree of undercoordination of at least a few Pt atoms. We do not have sufficient statistics from DFT calculations to make a conclusive connection between the average Pt-Pt bond length and the binding energy as a function of substrate defect although it would seem from the data that larger binding energies (more negative E_f) correlate with larger average Pt-Pt bond lengths. The EP data, which are obtained by averaging over a few different low-energy configurations, do seem to offer a more conclusive corroboration of this trend. In related work on adsorption of Pt_{100} clusters on edges of carbon platelets, Sanz-Navarro *et al.*[145] have shown that the Pt clusters tend to lose their initial partial fcc-like structure upon adsorption; this is accompanied by an increase in the average bond length of the adsorbed cluster by 1.4% over that of a free cluster. Previous DFT calculations of CO oxidation on Pt(111) surfaces have demonstrated the profound influence of lattice strain on reaction enthalpies and kinetics, with the potential to even change the rate-limiting step in the reaction network.[54] We expect that such effects could also be operative here, with the substrate defect (rather than a macroscopic externally applied strain field) influencing the extent of strain in the cluster bonds.

2.3.6 Electronic Structure of adsorbed Pt_{13} clusters

In this section, we turn our attention to the electronic structure of the previously described graphene-supported Pt clusters. The electronic structure of smaller Pt_n (n=1,2,3,4) clusters has been studied in detail previously [30, 33, 85, 172, 179] and is not revisited here. The electronic structure of Pt_{13} clusters, on the other hand, has only been considered in situations where the clusters have been relaxed from high-symmetry initial structures [32, 80, 105]; a detailed comparison with annealed clusters is therefore warranted. In the following, we present a detailed electronic structure analysis based on the projected density of states (PDOS), *d*-band shifts, and charge transfer for adsorbed clusters subjected to relaxation alone as well as a combination of annealing and relaxation.

First, we consider the case of graphene-supported Pt_{13} clusters, which were obtained by relaxation from initial high-symmetry shapes (Figure 2.7). The total density of states (DOS) was projected on to the *p* orbitals of C atoms and *d* orbitals of Pt atoms at the support–cluster interface that are involved in bond formation. The summed *p* and *d* DOS for these C and Pt atoms are displayed in Figures 2.10(b) and (c), respectively. To facilitate an understanding of how the *p* and *d* states are modified upon cluster adsorption, the *p* and *d* DOS from the same atoms in the unbound state of graphene-cluster are displayed in Figures 2.10(a) and (d), respectively. By comparing Figures 2.10(c) and (d) for the various cases, it is immediately apparent that the Pt *d*-band undergoes significant broadening upon cluster adsorption; the occupied *d* states, which were confined to an energy range of 4 eV below the Fermi level are now clearly visible up to about 7 eV below the Fermi level. At the same time, the sharp peaks in the vicinity of the Fermi level in Figure 2.10(a), arising from dangling C bonds at various point defects, disappear upon adsorption of the Pt cluster as seen in Figure 2.10(b) accompanied by an overall broadening of the *p* DOS; for the pristine support, where there are no dangling bonds to begin with, there is merely an overall broadening of occupied C *p*-states upon cluster adsorption. These observations are a clear sign of bond formation between the Pt cluster and the support. This is further supported by the charge density difference plots in Figure 2.10(e), which show significant redistribution of charge in the vicinity of the support-cluster interface.

A more quantitative analysis of the charge transfer to the support as well as the shifts in the cluster *d*-band is also possible. To quantify the total charge transfer, a Bader analysis [13, 70] was performed on the final structure (cluster + support).

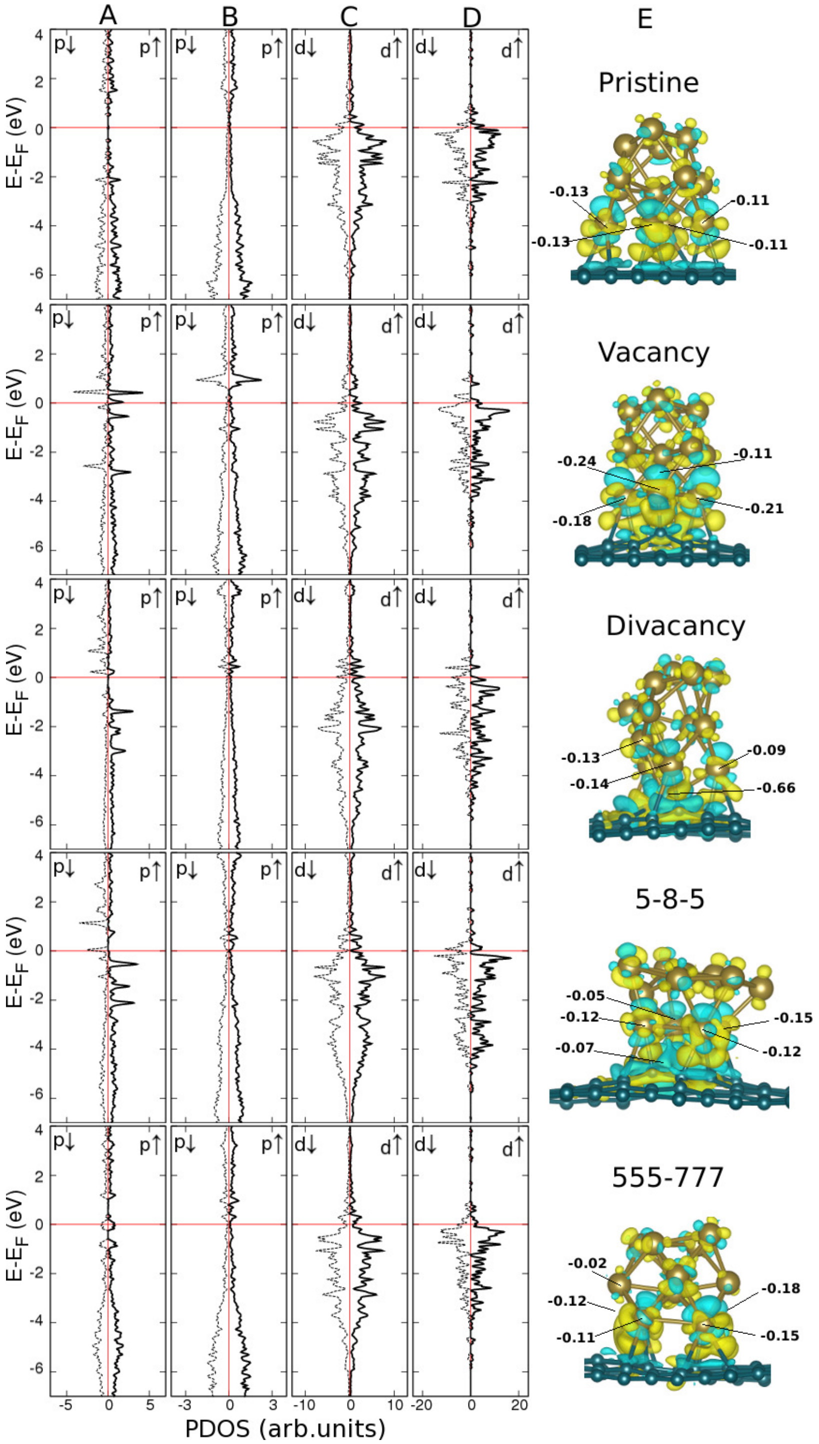

Figure 2.10: Projected density of states (PDOS) plots for clusters subjected to relaxation alone: (a) free graphene, (b) graphene after Pt_{13} adsorption, (c) adsorbed Pt_{13} cluster, (d) free Pt_{13} cluster. (e) Charge-density difference plot. Isosurfaces are at 0.027 e/Å^3); yellow (blue) color represents charge accumulation (depletion). The charge lost by Pt atoms bound to the substrate is indicated.

This procedure partitions the total charge density between atoms; by summing up the final charge density on the Pt_{13} cluster and the support atoms and comparing with the initial number of electrons in the cluster and support, we consistently find an appreciable net charge transfer from the Pt_{13} cluster to the graphene support (defective or otherwise). As seen from these charge-transfer data displayed in Table 2.6 as well as Figure 2.12(c), the stronger the binding of the cluster to the support the greater the charge transferred to the support. The shifts in the Pt *d*-band upon adsorption are quantified by determining the position of the *d*-band center in the adsorbed cluster. The filled *d* states of all Pt atoms in the cluster were used in this procedure. As seen from the data in Table 2.6 and Figure 2.12(a), the *d*-band centers undergo an appreciable downward shift, relative to their average position in the unsupported clusters, upon binding to the support. Once again, there is a positive correlation between the strength of binding and the downward shift of the *d*-band center. For the clusters with strongest binding (at a divacancy and 5-8-5 defect), the *d*-band center is shifted even further below that of the Pt(111) surface.

Table 2.6: *d*-band centers (ϵ_d) of adsorbed Pt_{13} clusters (relative to Fermi level) on various defective and defect-free graphene supports and charge transfer (Δq) *from* the Pt_{13} cluster *to* the support (electron charge taken to be negative).

	ϵ_d (eV)		Δq (e)	
	Relaxation alone	Annealing+Relaxation	Relaxation alone	Annealing+Relaxation
Pristine	-2.30	-2.34	-0.18	-0.08
Vacancy	-2.36	-2.53	-0.35	-0.48
Divacancy	-2.54	-2.49	-0.71	-0.81
5-8-5	-2.60	-2.58	-0.79	-0.72
555-777	-2.36	-2.51	-0.29	-0.30

A similar electronic structure analysis was performed for the clusters that were first subjected to MD annealing followed by DFT structural relaxation (Figure 2.8). Partial density of states plots as well as charge density difference plots for this case are displayed in Figure 2.11; the overall features qualitatively follow the discussion above. There is a broadening of the Pt *d*- and C *p*-bands, disappearance of sharp localized states near the Fermi level, and significant redistribution of charge at the cluster–support interface. There is, once again, transfer of electrons from the Pt_{13} cluster to the support and a downshift of the Pt *d*-band center upon adsorption. The extent of charge transfer and downshift of the *d*-band are positively correlated with the binding energy of the cluster [Table 2.6; Figures 2.12(b), (d)]. For all the cases of binding to defective supports, the *d*-band center is seen to shift below that of a Pt(111) surface.

The case of binding to the vacancy defect is particularly interesting. We recall that the Pt_{13} cluster has an adsorption energy of -4.67 eV when relaxed from a high-symmetry structure, which is significantly higher (weaker binding) than the adsorption energy of -7.29 eV found after the annealing procedure (Table 2.5): the latter structure being more strongly adsorbed, the *d*-band center is noticeably lowered (by 0.17 eV) relative to the former. Similarly, the annealed and relaxed structure transfers an additional 0.13 electrons to the support relative to the relaxed high-symmetry structure. This example underscores the need to search more extensively for low-symmetry, low-energy isomers of supported clusters when trying to make computational predictions of their catalytic activity. We also note that these observations of charge transfer from the Pt cluster to the graphene support accompanied by a shift of the Pt *d*-band away from the Fermi level in the presence of a vacancy are consistent with previous reports.[30, 105, 128, 179]

The data for binding to divacancies and divancy reconstructions reported here essentially complete the picture of binding of small Pt clusters to point defects in graphene. Overall, from the positions of the *d*-band centers in Table 2.6 and Figure 2.12, we conclude that point defects in graphene lower the *d*-band center of Pt_{13} clusters below that of a Pt(111) surface (and significantly below that of unsupported clusters). This lowering of the *d*-band center is expected to decrease the binding energy of CO molecules, among others, which provides a plausible explanation for experimental observations of increased CO-tolerance [101, 192] exhibited by reduced graphene oxide-Pt nanocomposites. Actual calculations of CO binding to these supported clusters are the main focus of Chapter 3.

2.4 Conclusions

In this chapter, we investigated the binding energetics and morphology of low-energy structures of Pt nanoclusters on defect-free and defective graphene substrates, using a combination of DFT and bond-order potential simulations. The primary conclusions of our study are as follows:

1. Point defects and their reconstructions in graphene act as strong binding traps for Pt clusters. Over the range of cluster sizes studied here, these defects bind Pt clusters more strongly than pristine graphene by several eV. Unreconstructed defects tend to be the strongest binding traps, although reconstructed defects can also serve as fairly strong traps. These observations provide a plausible explanation for the long-term stability toward sintering observed in Pt–graphene composites;[84, 101, 192] the graphene support in these composites is derived from graphene oxide, which is prone to defects.[14, 96, 131] Furthermore, the existence of defects in the graphene support could also provide an explanation for the greater stability towards sintering observed in Pt–graphene composites relative to Pt–carbon nanotube composites.[101] Thus, inducing pre-existing point defects in graphene supports could provide a facile route for synthesizing robust carbon-supported Pt nanocatalysts.

2. By employing a combination of empirical potential-based simulated annealing and DFT calculations, we have unambiguously shown that supported Pt clusters are neither high-symmetry structures nor are they readily derived from

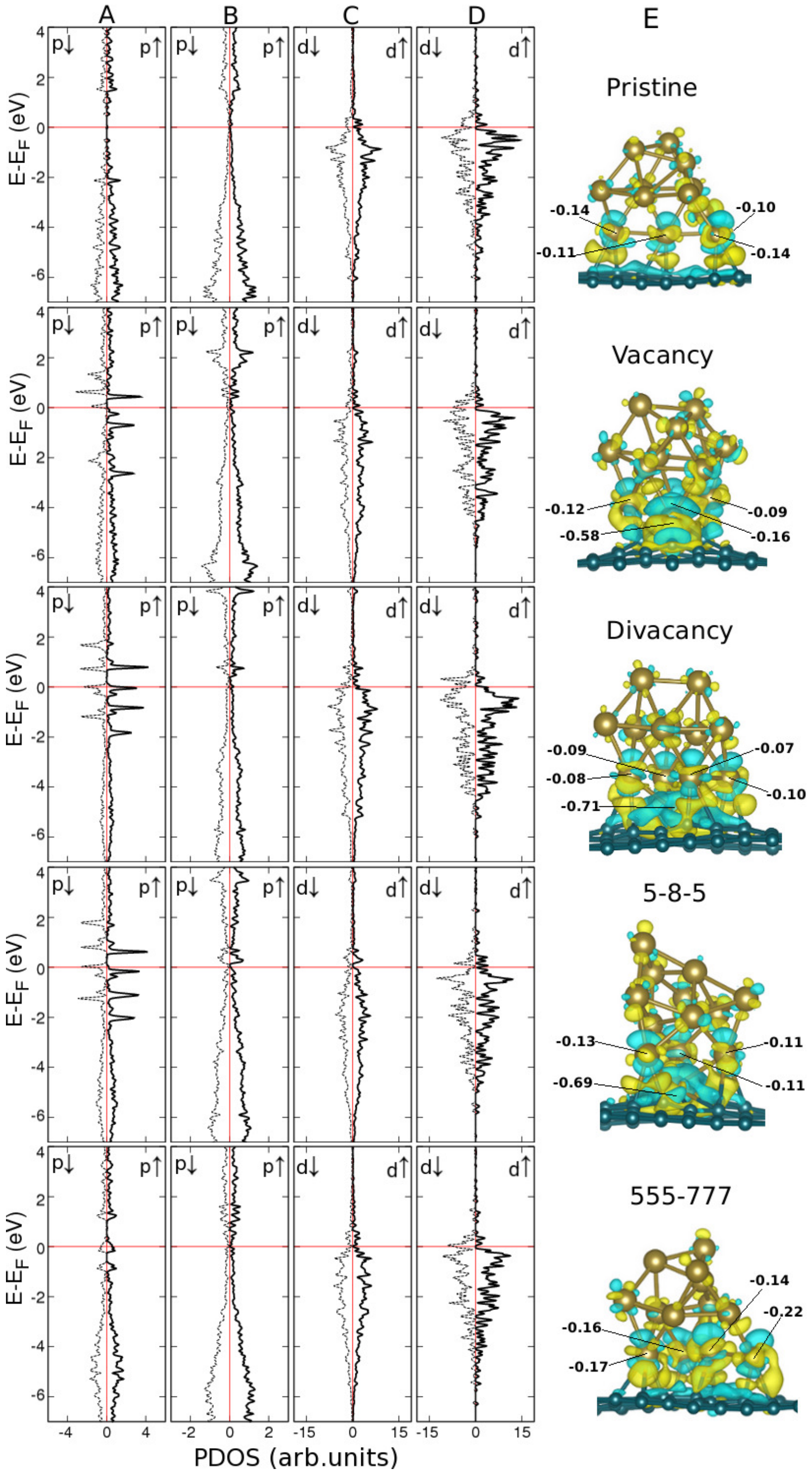

Figure 2.11: Projected density of states (PDOS) plots for annealed and relaxed clusters: (a) free graphene, (b) graphene after Pt_{13} adsorption, (c) adsorbed Pt_{13} cluster, (d) free Pt_{13} cluster. (e) Charge-density difference plot. Isosurfaces are at 0.034 e/Å^3); yellow (blue) color represents charge accumulation (depletion). The charge lost by Pt atoms bound to the substrate is indicated.

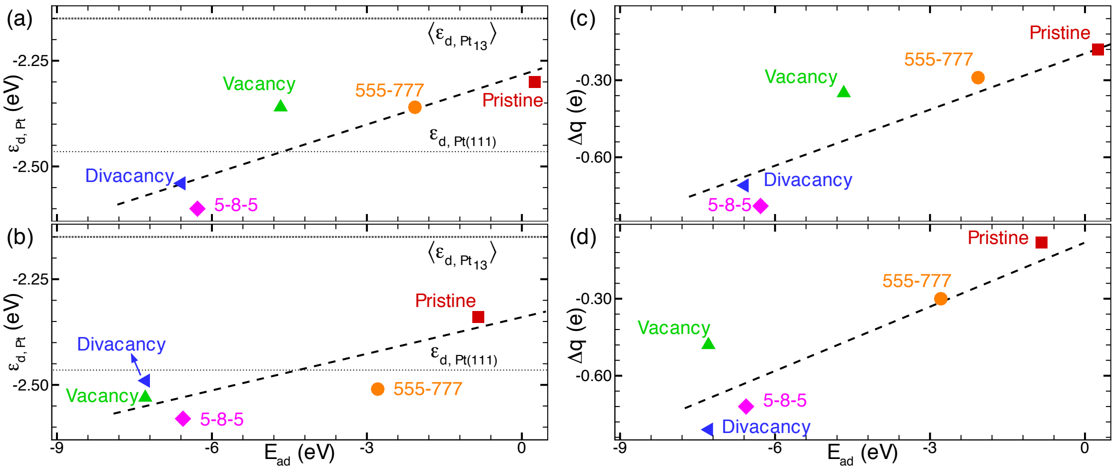

Figure 2.12: Position of d-band center ($\epsilon_{\mathrm{d,Pt}}$) relative to the Fermi level for supported Pt_{13} clusters subjected to (a) relaxation alone, and (b) annealing followed by relaxation. Horizontal dotted lines indicate the d-band center of the Pt(111) surface ($\epsilon_{\mathrm{d,Pt(111)}}$) and the average d-band center of the various free Pt_{13} clusters ($\langle \epsilon_{\mathrm{d,Pt_{13}}} \rangle$) considered here. Charge transfer from (c) relaxed, and (d) annealed and relaxed Pt_{13} clusters to the substrate. (The electron charge is taken to be negative here.) The dashed lines in all figures are merely a guide to the eye.

high-symmetry structures, as is often the assumption made in computational modeling. Instead, small clusters tend to adopt more open, low-symmetry morphologies similar to those observed in previous DFT studies of annealing of clusters in vacuum.[25, 89, 113, 180] Even though clusters that are nominally of high-symmetry in their initial state can undergo severe structural distortion upon relaxation and binding to a defect in the graphene support, their annealed, low-symmetry counterparts are consistently lower in energy, sometimes by *several* eV. These observations suggest that future investigations should first focus on determining at least a few candidate low-energy structures before addressing issues related to the catalytic activity of clusters. Without this initial step, the structures being sampled could simply be ones that are stuck in higher metastable minima, which could in turn corrupt further inferences related to binding energetics of molecules and energy barriers for reactions on the cluster.

3. The formation of strong bonds with the carbon substrate potentially influences the strain in a cluster: within the limited statistics available here, the average Pt-Pt bond length appears to increase with stronger binding to the substrate. We expect that this effect is of greater relevance for the small clusters considered here and this additional strain (or strain relief with respect to the bulk) in the bonds could affect the activity of the cluster. More comprehensive studies over several different cluster sizes are needed to make this connection clearer.

4. Electronic structure studies reveal a clear tendency for charge transfer from Pt clusters to the graphene substrate. Within the limited statistics available here, it would appear that there is a positive correlation between the strength of binding to the defect and the extent of charge transferred. Similarly, stronger binding of the cluster to the substrate appears to lead to a greater downshift of the cluster *d*-band center; in several instances, the cluster *d*-band center shifts further below that of a Pt(111) surface. This result suggests a decrease in the binding energy of CO to Pt clusters bound at point defects, which could offer a plausible explanation for reports [101, 192] of enhanced CO-tolerance of reduced graphene oxide-supported Pt nanoclusters. While this downshift in the *d*-band center might be desirable from the point of inhibiting catalyst poisoning, it should be noted that decreased binding of other molecular species might adversely impact the ability of the Pt clusters to catalyze reactions, which requires further investigation.

CHAPTER 3

CO ADSORPTION ON DEFECTIVE GRAPHENE–SUPPORTED PT$_{13}$ NANOCLUSTERS

3.1 Introduction

Graphene-supported transition-metal nanoparticles have attracted considerable interest as electrocatalysts in direct methanol fuel cells, proton exchange membrane fuel cells, and hydrogen fuel cells.[12, 77, 82, 84, 101, 135, 140, 148, 166, 192] For example, recent experiments in methanol fuel cells indicate that electrodes composed of Pt nanoclusters dispersed on chemically-converted graphene exhibit a lower tendency for sintering, accompanied by high catalytic activity and tolerance to CO poisoning, rivaling that of state-of-the-art Pt-Ru electrocatalysts.[84, 101, 146, 191, 192] Of these studies, several have also shown that defects in graphene supports play a key role in stabilizing the catalyst nanoclusters against sintering by providing strong anchoring sites.[83, 84, 176] This has been corroborated by computational studies that report a strong energetic preference for binding of Pt clusters at defect sites in graphene relative to a pristine graphene sheet [2, 45, 81, 83, 128, 176, 179] First-principles calculations also suggest that support defects can appreciably alter the morphology and electronic structure of clusters—most notably, causing a downshift of the Pt *d*-band center [30, 45, 105, 128, 179]—thereby improving their CO tolerance. The improved performance of Pt-graphene composite electrodes may then be attributed to several factors including: (a) stability towards sintering, which maintains high surface area over extended periods; (b) improved electrical conductivity of graphene supports relative to standard carbon black counterparts; and (c) fundamental modifications in the electronic structure of the supported nanoparticle as a result of strong binding to support defects. The relative importance of these factors and their potentially synergistic interaction is still not fully understood and remains a matter of current interest.

The purpose of this chapter is to systematically explore the interaction between various graphene point defects and Pt nanoclusters, and to quantify the effect of these interactions on the energetics of CO binding to the supported cluster. In the following, we focus on Pt_{13} nanoclusters and investigate, via first-principles density functional theory (DFT), the adsorption energetics of CO on free clusters as well as on clusters supported on pristine and defective graphene supports. The Pt_{13} clusters employed in our studies are optimized low-energy clusters with open, low-symmetry morphologies, that were derived via the annealing and quenching method reported in our previous study,[45] as described in Chapter 2. These clusters are thermodynamically more stable than the high-symmetry icosahedral or octahedral Pt_{13} clusters. To account for the inherent statistical variability in the local environment of adsorption sites (symmetry-inequivalent on-top, hollow, and bridge sites) encountered by a CO molecule on a low-symmetry Pt_{13} cluster, we randomly sample the CO binding energy at several distinct sites (ranging from 9 to 14 sites) per cluster–defect combination. Our studies show that Pt_{13} clusters supported on defective graphene bind CO more weakly than their unsupported counterparts, the strength of CO binding being inversely correlated with the strength of cluster–support binding. While CO binding on defect-supported clusters is still stronger than on an ideal Pt(111) surface, a more realistic comparison with binding at undercoordinated sites, such as vacancies or step edges on Pt surfaces, results in nearly comparable binding energies. Overall, our results clearly indicate the propensity of defective graphene substrates to reduce the binding energy of CO molecules on Pt_{13} clusters, which could be an important mechanism through which graphene-supported Pt nanoclusters exhibit increased CO tolerance in experiments.

This chapter is structured as follows. In Section 3.2 we present computational details of our DFT calculations. Results and discussion on CO adsorption energetics are presented in Section 3.3. Concluding remarks are provided in Section 3.4.

3.2 Computational Details

All calculations were performed with the plane-wave DFT method as implemented in the Vienna *Ab Initio* simulation package (VASP). [86, 87] The projector-augmented wave (PAW) method [18, 88] was used to describe the core and valence electrons. The Perdew-Burke-Ernzerhof [132] form of the Generalized-Gradient Approximation was employed to describe electron exchange and correlation. All calculations were performed on a 6×6 graphene supercell with periodic boundary conditions; periodic images were separated by vacuum in excess of 15 Å normal to the sheets to prevent spurious image interactions. A kinetic energy cutoff of 400 eV was used in all structural relaxation simulations of CO adsorption and the Brillouin zone was sampled using a 5 x 5 x 1 Γ-centered k-point mesh. Reference calculations for Pt(111) were performed on a four-layer, 4×4 slab with periodic boundary conditions in the plane of the surface. Atoms in the bottommost layer were fixed at their bulk positions while the top three layers were relaxed in all calculations. A kinetic energy cutoff of 400 eV was used in these slab calculations with a Γ-centered 7 x 7 x 1 k-point mesh for Brillouin-zone sampling. In all cases (slab and cluster), structural relaxations were performed using a conjugate gradient algorithm until forces on all atoms were below 0.01 eV/Å. To accelerate electronic convergence, a second-order Methfessel-Paxton[121] smearing of the Fermi surface was employed with a smearing width of 0.05 eV. All calculations were performed with spin-polarization.

For supported-cluster studies, we employed the lowest-energy structures of graphene supported Pt_{13} clusters derived via the annealing and quenching method as described in Chapter 2.[45] These structures also have lower energy, lower symmetry, and a more open morphology than the icosahedral or octahedral clusters that have commonly been used in DFT studies. To compare and contrast CO binding on supported versus free clusters, the low energy clusters were also removed from the graphene supports and employed in studies of CO adsorption (with full structural relaxation). This procedure allows us to directly address the effect of the support on CO binding.

Throughout this chapter, we employ the adsorption energy (E_{ad}) of CO on graphene-supported as well as free Pt_{13} clusters as a metric for the strength of binding between CO and Pt, which is defined as

$$E_{ad} = \begin{cases} E_{C_m+Pt_{13}+CO} - E_{C_m+Pt_{13}} - E_{CO}, & \text{supported clusters} \\ E_{Pt_{13}+CO} - E_{Pt_{13}} - E_{CO}, & \text{free clusters} \end{cases} \tag{3.1}$$

where $E_{C_m+Pt_{13}+CO}$, $E_{C_m+Pt_{13}}$, $E_{Pt_{13}+CO}$, and E_{CO} are the total energies of the graphene–Pt_{13}–CO system, the graphene–Pt_{13} system, the CO–Pt_{13} system and the CO molecule as obtained from DFT calculations. As defined here, more negative values of E_{ad} signify stronger binding.

3.3 Results and Discussion

3.3.1 CO adsorption on free and graphene–supported Pt_{13} clusters

First, we examine the adsorption of a single CO molecule on free and graphene–supported low energy Pt_{13} clusters. On a planar surface such as Pt(111), it is relatively straightforward to identify via symmetry arguments a minimal set of binding sites (on-top, bridge, hollow sites) for CO adsorption studies. While similar on-top/bridge/hollow binding sites can be identified on a Pt_{13} cluster such as the one displayed in Figure 3.1, reduced (or complete lack of) symmetry renders each of these sites unique; it is not feasible to sample each and every such site with DFT. To render this problem tractable while still accounting meaningfully for the inherent statistical variability in the nature of binding sites, we randomly sample between 9 to 14 different adsorption sites on every cluster. To further account for the influence of support defects on CO–Pt_{13} interactions, we sample over clusters supported on pristine graphene as well as on defective graphene containing a single vacancy, an unreconstructed divacancy, and a 555-777 divacancy reconstruction. Figure 3.1 shows some of the sampled CO adsorption sites for the case of a low-energy Pt_{13} cluster supported on graphene with single vacancy. Similar sampling procedures were followed for the other cases.

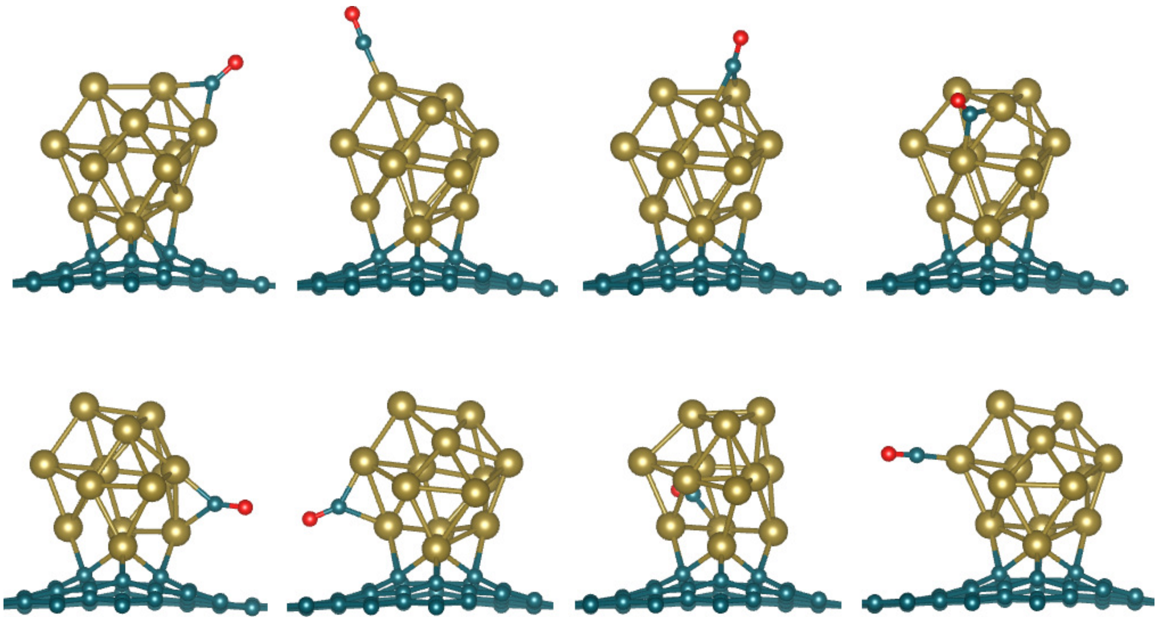

Figure 3.1: Sampled CO adsorption sites on a low-energy Pt_{13} cluster supported at a single vacancy in graphene. Cyan, gold, and red spheres represent C, Pt, and O atoms, respectively.

In Table 3.1, we report the average CO adsorption energy on graphene-supported and free Pt_{13} clusters, calculated according to Eq. 3.1. Statistical errors are estimated using a 95% confidence interval of the Student's t-distribution, which is appropriate for small-sample statistics. The average C-O bond lengths (d_{C-O}) for the adsorbed

Table 3.1: Average adsorption energy and bond lengths (d_{C-O}) for CO molecules adsorbed on low-symmetry Pt_{13} clusters supported on pristine and defective (single vacancy, unreconstructed divacancy, 555-777 reconstructed divacancy) graphene, as well as on free Pt_{13} clusters. CO adsorption energies on Pt(111) at an on-top (T) site, a vacancy site (V) and a vacancy line (V-line) are reported for comparison. For reference, the C-O bond length in an isolated molecule is calculated to be 1.17 Å.

Graphene substrate	E_{ad} (eV)	d_{C-O} (Å)
pristine	-2.54 ± 0.19	1.18 ± 0.01
vacancy	-2.33 ± 0.11	1.18 ± 0.01
divacancy	-2.02 ± 0.18	1.18 ± 0.01
555-777	-2.24 ± 0.17	1.19 ± 0.01
free clusters	-2.79 ± 0.30	1.17 ± 0.01
Pt(111)(T)	-1.66	1.16
Pt(111)(V)	-2.21	1.18
Pt(111)(V-line)	-2.27	1.19

CO molecule are also reported here along with their statistical errors. Among the different CO adsorption sites studied on the Pt_{13} clusters, we found on average that CO tends to bind more strongly to on-top sites of the clusters whereas adsorption is generally weaker on hollow sites of the clusters. We do not find any obvious correlation between the binding energy of CO to the cluster relative to the distance of the binding site from the graphene substrate (i.e., towards the bottom or top of the cluster). The fully relaxed atomic structures for one selected case each of CO adsorption on supported clusters and free clusters are displayed in Figure 3.2.

The CO adsorption energy results reported in Table 3.1 indicate that the presence of a point defect in the graphene substrate weakens the interaction of the CO molecule with the Pt_{13} clusters. In particular, for the three different defective graphene supports (single vacancy, unreconstructed divacancy and 555-777 divacancy reconstruction), the CO adsorption energy on the Pt_{13} cluster is lower by 0.21 eV, 0.52 eV, and 0.30 eV, respectively, compared to the average adsorption energy on Pt_{13} clusters supported on defect-free pristine graphene; the difference in binding energies relative to unsupported Pt_{13} clusters is even larger (0.46 eV, 0.77 eV, and 0.55 eV, respectively).

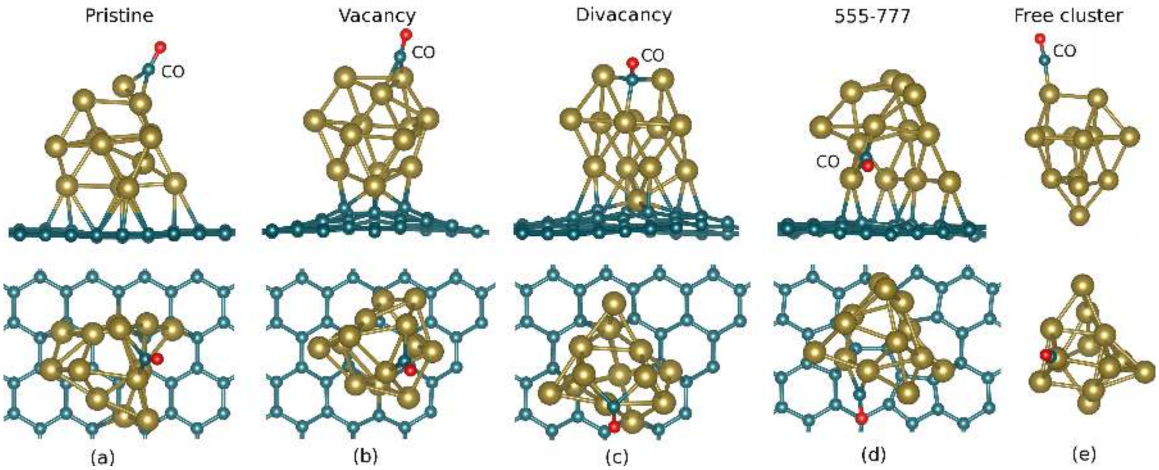

Figure 3.2: Side and top view of selected low energy DFT configurations for adsorption of a CO molecule on graphene-supported Pt_{13} clusters. Cyan, gold and red spheres represent C, Pt and O atoms, respectively.

Previous reports,[30, 45, 105, 128, 179] have correlated the presence of a point defect on the graphene support with stronger binding of the metal cluster. Here, another key role of the the point defect in the graphene substrates is revealed: CO adsorption is less favorable on Pt_{13} clusters supported at defective graphene substrates as compared to isolated Pt_{13} clusters. This result is particularly significant because it suggests that defect engineering of graphene substrates could improve the CO tolerance of extremely small Pt clusters. Examining the average C-O bond lengths (d_{C-O}) for the adsorbed CO molecule (Table 3.1), we notice that the C-O bond (1.17 Å for an isolated molecule) is slightly elongated by 0.01-0.02 Å for graphene-supported clusters relative to the unsupported ones.

The obvious question that needs to be addressed is how CO adsorption on Pt_{13} clusters compares with that on macroscopic Pt surfaces. We studied the adsorption of a single CO molecule at the experimentally preferred on-top (T) site of the Pt(111) surface[1] and computed an adsorption energy of -1.66 eV (Table 3.1); the CO

---

[1] The on-top site of the Pt(111) surface is the favored CO-adsorption site in reality, whereas DFT prefers adsorption at an FCC hollow site.[4, 34, 61, 62, 73, 127, 134] The DFT binding energy at

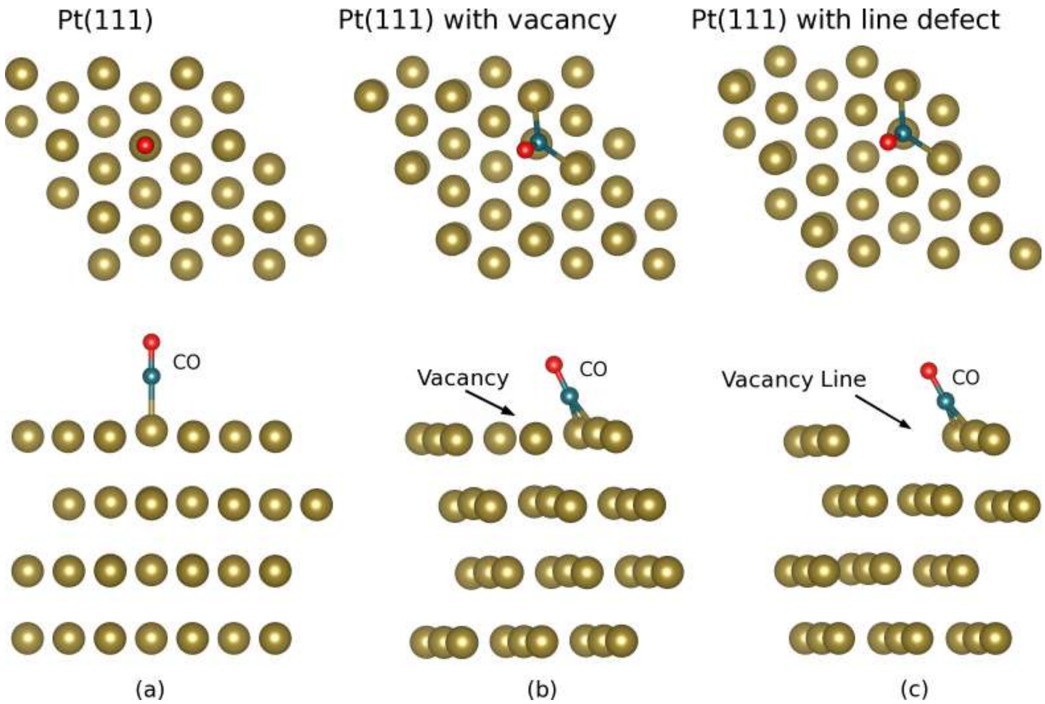

Figure 3.3: Side and top view of DFT configurations for adsorption of a CO molecule on Pt(111) surface slabs. Cyan, gold and red spheres represent C, Pt and O atoms, respectively.

molecule is thus more weakly bound to an ideal Pt(111) surface than to any Pt_{13} cluster (supported or otherwise). A more realistic estimate for a Pt electrode should, at the very least, account for the presence of surface defects (vacancies/adatoms/step-edges/kinks) as well as other crystalline orientations. To ascertain, at least approximately, the energetics of binding at undercoordinated sites, we also examined CO binding to a single vacancy and to a vacancy line (which is a rough approximation of a step-edge) on Pt(111) and computed adsorption energies of -2.21 eV and -2.27 eV, respectively. Binding to these surface defects is then energetically comparable to that on defective graphene-supported Pt_{13} clusters (Table 3.1). While detailed studies of CO adsorption on other crystalline facets is beyond the scope of this study, we note

---

the FCC hollow (1.80 eV) though is quite close to the experimental binding energy at the on-top site (1.68±0.12 eV [189]) for comparison some relevant studies from the literature. DFT studies report that CO binds more strongly to step-edges on Pt(211) surfaces as compared to terrace sites of both the Pt(211) as well as the flat Pt(111) surface,[31, 79] with adsorption energies in the range of -1.95 eV to -2.49 eV. Orita and Inada[130] found that CO binds preferentially at a step-edge on the Pt(211) surface with an adsorption energy of -2.41 eV, and at the step-edge of an unreconstructed Pt(311) surface with an adsorption energy of -2.43 eV. Yamagishi *et al.* [188] reported that CO binds at a step-edge on a Pt(410) surface with an adsoprtion energy of -2.49 eV and at a step-edge on a Pt(110) surface with adsorption energy of -2.36 eV. These studies, in conjunction with the two cases of a defective Pt(111) surface considered here, indicate that a CO molecule, on average, is adsorbed at least as strongly to undercoordinated Pt surface sites as to defective graphene-supported Pt_{13} clusters. Unsupported Pt_{13} clusters, however, bind CO more strongly than in any of the above cases. Thus, our results suggest that defective graphene supports can indeed play a role in mitigating CO poisoning of sub-nanometer Pt clusters.

3.3.2 Electronic structure of CO bound on graphene-supported and free Pt_{13} clusters

Next, we analyze the electronic structure of the graphene–Pt_{13} cluster–CO systems for the four different types of graphene supports as well as the free Pt_{13} cluster–CO systems. In the previous chapter, we showed a clear correlation between the position of the *d*-band center of the bound cluster and the nature of the support point defect. Specifically, stronger binding of the cluster to the defect (which is directly related to the number of dangling bonds at the defect) is accompanied by increased charge transfer from the cluster to the substrate and a shift of the cluster *d*-band center away from the Fermi level. In Figure 3.4, we correlate this *d*-band shift—which is effectively a surrogate for the type of binding defect—to the average

CO adsorption energy. As seen from this figure, the position of the cluster *d*-band center is well correlated with the CO adsorption energy: the further away the *d*-band center is from the Fermi level, the weaker is the CO adsorption energy.[57, 63–65] This could provide a credible explanation for experimental observations of increased CO tolerance [84, 101, 146, 191, 192] exhibited by Pt nanoparticles on chemically-converted graphene or graphene oxide supports, which are inherently defective unlike exfoliated graphene.

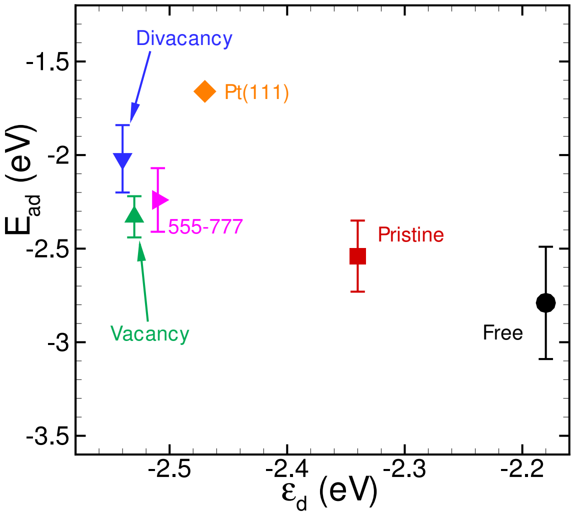

Figure 3.4: CO adsorption energy (E_{ad}) as a function of *d*-band center (ϵ_d) relative to the Fermi energy for supported Pt_{13} clusters, free Pt_{13} clusters, and Pt(111) surface. A downshift of the cluster *d*-band center with respect to the Fermi level (more negative ϵ_d) is directly correlated with weaker adsorption of CO on the cluster. Error bars indicate 95% confidence intervals obtained from sampling over multiple adsorption sites on the cluster.

For all the cases of CO adsorption on graphene-supported and free Pt_{13} clusters, a Bader analysis [13, 70] was performed, partitioning the total charge density between atoms, which then allowed us to quantify the total charge transfer between the cluster, CO molecule, and graphene support. The average charge transfer, Δq, between these constituents is reported in Table 3.2. We consistently find an appreciable net charge transfer from the Pt_{13} cluster to both the graphene support as well as the

CO molecule. There is also significant redistribution of charge within the cluster and CO molecule, as well as in the immediate vicinity of the cluster within the graphene sheet, as seen clearly in the charge-density difference plots for select cases (Figure 3.5). The yellow and blue regions in these plots indicate the areas of charge accumulation and depletion, respectively. The adsorption of the CO molecule itself induces fairly localized charge redistribution in the immediate vicinity of the adsorption site as seen from the case of CO adsorption on the free cluster. The amount of charge transferred from the Pt cluster to CO ($\sim 0.25\mathrm{e}^-$; $\sim 0.12\mathrm{e}^-$ to C and $\sim 0.13\mathrm{e}^-$ to O) is also essentially independent of the cluster interaction with graphene. The charge transferred from the Pt cluster to graphene is, however, quite sensitive to nature of the support. A cluster adsorbed on pristine graphene transfers some charge to the support ($\sim 0.1e^-$), but this is relatively small as compared to the charge transfer from a cluster to a defective substrate ($\sim 0.2 - 0.8$ eV). It is this substantial depletion of charge from the cluster to the defective support that leads to a downshift of the Fermi energy,[45] which in turn leads to weaker CO binding to the cluster as was alluded to in Chapter 2.

Table 3.2: Average charge transfer [Δq (e^-)] from the Pt_{13} cluster to CO and pristine graphene, single vacancy, unreconstructed divacancy and 555-777 reconstructed divacancy based on Bader analysis. (Positive/negative numbers indicate accumulation/depletion of electrons.)

	Δq (e^-)		
	substrate	cluster	CO
pristine	0.09 ± 0.02	-0.35 ± 0.04	0.25 ± 0.03
vacancy	0.44 ± 0.01	-0.70 ± 0.02	0.26 ± 0.02
divacancy	0.76 ± 0.02	-1.01 ± 0.04	0.25 ± 0.03
555-777	0.26 ± 0.03	-0.52 ± 0.03	0.26 ± 0.03
free clusters	–	-0.24 ± 0.03	0.24 ± 0.03

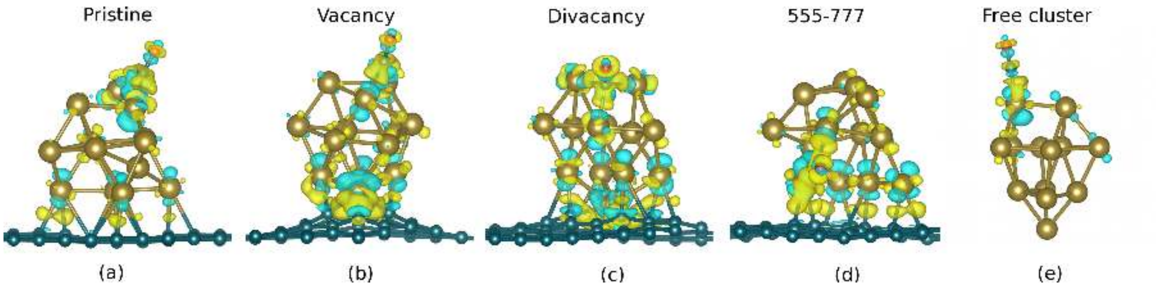

Figure 3.5: Charge-density difference plots for the selected DFT configurations of Figure 3.2. Isosurfaces are at 0.054 e/Å^3; yellow(blue) color represents charge accumulation(depletion).

3.4 Conclusions

In conclusion, DFT calculations were employed to investigate the adsorption of CO on Pt_{13} clusters supported on defect-free and defective graphene substrates, as well as unsupported clusters. Pt_{13} clusters were found to bind strongly to defects in graphene and correspondingly bind CO molecules more weakly as compared to clusters supported on pristine graphene. In all cases, graphene-supported Pt_{13} clusters were found to bind CO more weakly than unsupported Pt_{13} clusters. These observations were explained in terms of the downshift of the *d*-band center position of the clusters upon binding to defects: stronger binding leads to greater charge transfer from the cluster to the substrate accompanied by a greater downshift of the *d*-band center. Consequently, the probe CO molecule binds more weakly to the cluster. While an ideal Pt(111) surface was found to bind CO more weakly than any of the Pt_{13} clusters studied here (supported or unsupported), binding to defects to the Pt(111) and other low-index surfaces is of comparable magnitude to that on supported Pt_{13} clusters. Overall, our study suggests that defect-engineered graphene can not only serve as robust support that strongly binds and stabilizes clusters against sintering, but might also allow for optimizing catalytic properties through tuning of cluster–substrate interactions. Additional investigations of CO oxidation kinetics to verify that such cluster–substrate interactions can also substantially influence the removal of CO, are the main focus of Chapter 4.

CHAPTER 4

THE INFLUENCE OF SUPPORT EFFECTS ON CO OXIDATION KINETICS ON CO–SATURATED GRAPHENE–SUPPORTED PT$_{13}$ NANOCLUSTERS

4.1 Introduction

Platinum(Pt) catalysts are widely used as anode materials in fuel cells due to their high activity and selectivity for a variety of electrochemical reactions. Experimental observations demonstrate that sub-nanometer Pt nanoparticles supported on graphene exhibit increased stability, uniform dispersion, tolerance to CO poisoning and exceptionally high activity for oxidation reactions, making them attractive candidates as electrocatalysts in direct methanol fuel cells, proton exchange membrane fuel cells, and hydrogen fuel cells.[9, 38, 40, 68, 84, 90, 101, 102, 139, 140, 142, 148, 149, 151, 155, 164, 183, 185, 191, 192, 194, 196] More specifically, experimental studies attribute the improved performance of Pt-graphene nanocatalysts to the synergetic effect between the Pt catalyst and the graphene substrate, mainly due to the presence of defects and functional groups in the graphene substrate that are formed during the fabrication process, leading to a strong interaction between the cluster and the support.[49, 67, 68, 84, 101, 137, 144, 168, 183] Computational studies also report a strong binding of Pt clusters at defect sites in graphene relative to pristine graphene, leading to a significant modification of the morphology and the electronic structure of the clusters and having an immediate effect on their catalytic activity. [41, 45, 46, 80, 105, 106, 128, 170, 197]

CO oxidation is a reaction of practical relevance as CO poisoning of the catalyst remains a serious problem in the operation of fuel cells, significantly compromising anode performance even in trace amounts.[16, 29, 36, 66, 154, 173, 195] Therefore, CO oxidation on platinum has been studied extensively both experimentally and computationally.[3, 4, 6, 21, 27, 39, 43, 44, 47, 50, 52, 53, 72, 76, 111, 115, 120, 123, 156, 163, 186, 187, 189] Most of the previous Pt–CO oxidation studies have focused on different types of Pt surface models (i.e., Pt(111), Pt(110), steps and kinks in Pt surfaces) as well as on Pt nanoclusters. However, graphene–Pt nanoparticle systems are still relatively unexplored in this regard. Although a large number of experimental studies have shown the increased tolerance to CO poisoning for graphene–Pt nanoparticle systems,[9, 38, 68, 84, 101, 102, 139, 148, 149, 164, 183, 191, 192] only a few studies have addressed CO oxidation.[90, 191, 192, 194] Therefore, fundamental issues, such as the preferred kinetic mechanisms of CO-oxidation, and support and coverage effects on the reaction energetics still remain unclear and are topics of current interest. Only a few recent computational studies have focused on CO oxidation on graphene or graphene oxide–supported Pt catalysts.[167, 169, 171] Among these studies, Tang *et al.* [169] investigated the catalytic CO oxidation at a single Pt atom on pristine and single vacancy graphene substrates. In their study Tang *et al.* [169] first investigated a Langmuir–Hinshelwood (L–H) type mechanism for the CO oxidation reaction ($CO^* + O_2^* \rightarrow O\text{–}O^*\text{–}C\text{–}O \rightarrow CO_2 + O^*$) and they calculated energy barriers of 1.03 eV for oxygen activation on a Pt atom bound at a pristine graphene substrate and 0.58 eV for the single vacancy support, respectively. For the single vacancy substrate they also investigated a second step, where the preadsorbed O^* from the previous L–H step reacted with a CO molecule, via an Elay–Rideal (E–R) type mechanism ($O^* + CO \rightarrow CO_2$). The activation energy for this second step was calculated to be 0.59 eV. An E–R type mechanism was also investigated for the CO oxidation reaction at a Pt atom supported on pristine graphene, with preadsorbed O_2^* reacting with a CO molecule in the gas phase. The reaction proceeded with the formation of a stable carbonate–like intermediate, CO_3^*, ($CO^* + O_2^* \rightarrow CO_3^* \rightarrow$

CO_2 + O*), which endothermically dissociated into CO_2 + O* with a barrier of 0.77 eV. Tang *et al.* [169] thus concluded that the L–H mechanism is the preferred first step of the reaction, followed by an E–R second step. The Pt atom supported on a single vacancy showed higher catalytic activity compared to the Pt-pristine graphene system by approximately 0.5 eV.

Although the aforementioned studies provide a basis for the kinetics of CO oxidation on graphene–Pt–nanoparticle systems, at low temperatures, CO oxidation occurs at near saturation CO coverages, making conclusions from previously reported model experimental and theoretical studies at low–coverages difficult to extend to catalytic reactions on actual systems.[118] Near–saturation adsorbate coverages weaken cluster-adsorbate bonds, thereby significantly influencing the binding energies of adsorbed spices and their reactivity in cluster–catalyzed reactions. Recently Allian *et al.*, [6] investigated the kinetics of CO oxidation on CO–saturated Pt(111) surfaces and CO–saturated cuboctahedral Pt_{201} nanoclusters. The authors suggested that CO oxidation on such clusters nearly saturated with CO, occurs via a CO*–assisted O_2 activation on vacant sites within CO monolayers, without either the involvement of adsorbed O_2* precursors or O_2 dissociation, and it is favored over the L–H mechanism.[6] To the best of our knowledge, there haven't been any previous reports on CO oxidation catalysis on small graphene–supported Pt nanoclusters at nearly saturated CO coverages, conditions typical of their practical usage.

The goal of this chapter is to provide a systematic investigation of support effects on the kinetics of CO oxidation reaction on fully CO–saturated, low–energy, Pt_{13} nanoclusters supported on graphene, via first-principles density functional theory (DFT). Specifically, we study in detail the kinetic mechanism for CO oxidation proposed by Allian *et al.*, [6] at various surface sites on unsupported Pt_{13} nanoclusters as well as clusters bound at support point defects (vacancies/divacancies). Our studies show that the relevant kinetic mechanism for CO oxidation on these clusters proceeds via a CO*-assisted activation of the O_2 molecule, resulting in the formation of an O*–O–C*–O transition state that decomposes into CO_2 and a chemisorbed O* species. Our results clearly establish the role of the defective graphene supports in substantially reducing the barrier for CO oxidation reaction. At the same time, we also find that support defects are crucial in stabilizing the Pt_{13} clusters at high CO-coverages; in contrast, Pt_{13} clusters supported on defect-free graphene tend to desorb upon CO saturation leading to catalyst loss. Defective graphene–supported Pt_{13} clusters are therefore able to serve as efficient catalysts for the CO oxidation reaction with significantly lower energy barriers than unsupported clusters.

The remainder of this chapter is organized as follows. In Section 4.2 we present computational details of our DFT calculations. Results and discussion are presented in Section 4.3 and concluding remarks are provided in Section 4.4.

4.2 Computational Details

All calculations were carried out using the plane-wave DFT method as implemented in the Vienna *Ab Initio* simulation package (VASP). [86] The projector-augmented wave (PAW) method [18, 88] was used to describe the core and valence electrons. The Perdew-Burke-Ernzerhof [132] form of the Generalized-Gradient Approximation was employed to describe electron exchange and correlation. All calculations were performed on a 6×6 graphene supercell with periodic boundary conditions; periodic images were separated by vacuum in excess of 18 Å normal to the sheets to prevent spurious image interactions. A kinetic energy cutoff of 400 eV was used in all structural relaxation simulations of O adsorption and a 5 x 5 x 1 Γ-centered k-point mesh was used to sample the Brillouin zone. Structural relaxations were performed using a conjugate gradient algorithm until forces on all atoms were below 0.01 eV/Å. To accelerate electronic convergence, a second-order Methfessel-Paxton[121] smearing of the Fermi surface was employed with a smearing width of 0.05 eV. All calculations were spin-polarized.

For supported-cluster studies, we employed the lowest-energy structures of Pt_{13} clusters supported on graphene derived via the annealing and quenching method discussed in Chapter 2. To compare CO and O adsorption on supported versus free clusters, the low energy clusters were removed from the graphene supports and subjected to full structural relaxation. The adsorption energy of CO or O ($E_{ad,X}$; X=CO, O) on graphene–supported and free Pt_{13} nanoclusters is defined as

$$E_{ad,X} = \begin{cases} E_{C_m+Pt_{13}+X} - E_{C_m+Pt_{13}} - E_X, & \text{supported clusters} \\ E_{Pt_{13}+X} - E_{Pt_{13}} - E_X, & \text{free clusters} \end{cases} \tag{4.1}$$

where $E_{C_m+Pt_{13}+X}$, $E_{C_m+Pt_{13}}$, $E_{Pt_{13}+X}$ are the total energies of the graphene–Pt_{13}–X (X=CO,O) system, the graphene–Pt_{13} system, the Pt_{13}–X system and E_X represents the energy of the CO molecule or half the energy of the O_2 molecule in vacuum, as appropriate. As defined here, more negative adsorption energies signify stronger binding.

CO–saturated Pt_{13} clusters are then constructed, by binding 13 CO molecules to each cluster to achieve a 1:1 CO to Pt atom coverage. The systems were subsequently subjected to *ab initio* NVT molecular dynamics annealing simulations over 0.6 picoseconds at 1500K followed by quenching to 1K over 0.6 picoseconds, to ensure that the clusters are structurally stable. The quenched structures were then subjected to structural optimization until forces on all atoms were below 0.02 eV/Å. For unsupported Pt_{13} clusters the same procedure was followed in vacuum. To quantify the strength of binding of CO–saturated clusters to pristine and defective graphene supports, the adsorption energy of the cluster on the support ($E_{ad,cluster}$) was calculated,

$$E_{ad,cluster} = E_{C_m+Pt_{13}+13CO} - E_{C_m} - E_{Pt_{13}+13CO} \tag{4.2}$$

where $E_{C_m+Pt_{13}+13CO}$ is the total energy of the graphene–Pt_{13}+13-CO system after the annealing–relaxation procedure, and E_{C_m}, $E_{Pt_{13}+13CO}$ are the energies of the graphene substrate and the Pt_{13}+13-CO system, respectively, obtained from DFT calculations after separating the cluster from the graphene support and subjecting them to structural relaxation. The effect of CO coverage on the CO adsorption energy was quantified by calculating the adsorption energy per CO molecule, defined as

$$E_{ad/CO} = \begin{cases} \frac{1}{13}(E_{C_m+Pt_{13}+13CO} - E_{C_m+Pt_{13}} - 13E_{CO}), & \text{supported clusters} \\ \frac{1}{13}(E_{Pt_{13}+13CO} - E_{Pt_{13}} - 13E_{CO}), & \text{free clusters} \end{cases} \tag{4.3}$$

where $E_{C_m+Pt_{13}+13CO}$, $E_{C_m+Pt_{13}}$, and E_{CO} are the total energies of the graphene–Pt_{13}+13-CO system, the cluster–substrate relaxed structure before CO saturation, and the CO molecule in vacuum, respectively.

Subsequent to adsorption studies, the Climbing-Image Nudged-Elastic-Band (CINEB) method [71] was applied to locate transition states and minimum–energy pathways for the CO oxidation reaction on graphene–supported and free CO–saturated Pt_{13} clusters. All Pt atoms were allowed to relax, while the C atoms on the graphene support were kept fixed during the CINEB calculations. Due to the computational cost of these calculations, we employed a 3 x 3 x 1 Γ-centered k-point mesh, a 300 eV kinetic energy cutoff, and a force tolerance of 0.03 eV/Å for the relaxation of the initial and final states and the CINEB calculations. Selected tests reveal that these slightly less stringent criteria lead to changes of the order of 10 meV in the reaction barrier, which is within the accuracy of the calculation. Transition states were verified by calculating the Hessian matrix and identifying a single imaginary frequency.

4.3 Results and Discussion

4.3.1 Support effects on CO and O adsorption on graphene–supported Pt_{13} clusters

First, we examine the support effects on CO and O adsorption, the two species directly involved in the CO oxidation reaction. The CO adsorption was discussed in detail in Chapter 3, [46] and some of the results are reproduced here for the purposes of the discussion. O adsorption at graphene–supported and free Pt_{13} clusters is investigated via random sampling over several distinct binding sites. The details of the sampling procedure are similar to the CO adsorption sampling that was described in Chapter 3, Section 3.2. The average CO and O adsorption energy on graphene-supported and free Pt_{13} clusters, calculated according to Eq. 4.1, are reported in Table 4.1. Statistical errors are estimated using a 95% confidence interval of the Student's t-distribution, which is appropriate for small-sample statistics. The fully relaxed atomic structures for one selected case each of O adsorption on graphene-supported and free Pt_{13} clusters are displayed in Figure 4.1.

Table 4.1: Average adsorption energy for CO (from Ref. [46]) and O molecules adsorbed on low-symmetry Pt_{13} clusters supported on pristine and defective (single vacancy, unreconstructed divacancy) graphene, as well as on free Pt_{13} clusters. The position of *d*-band center (E_{d-band}) for the Pt_{13} clusters is reported in the last column.

Graphene substrate	$E_{ad,CO}$ (eV)	$E_{ad,O}$ (eV)	E_{d-band} (eV)
pristine	-2.54 ± 0.19	-1.66 ± 0.38	-2.34
vacancy	-2.33 ± 0.11	-1.48 ± 0.19	-2.53
divacancy	-2.02 ± 0.18	-1.42 ± 0.41	-2.54
free clusters	-2.79 ± 0.30	-1.76 ± 0.26	-2.18

The adsorption energy results in Table 4.1 indicate that the presence of a point defect in the graphene support weakens the interaction of CO and O atom with the supported Pt_{13} clusters. In particular, for the two defective graphene supports (single vacancy (SV) and divacancy (DV)) the CO adsorption energy on the Pt_{13} cluster is

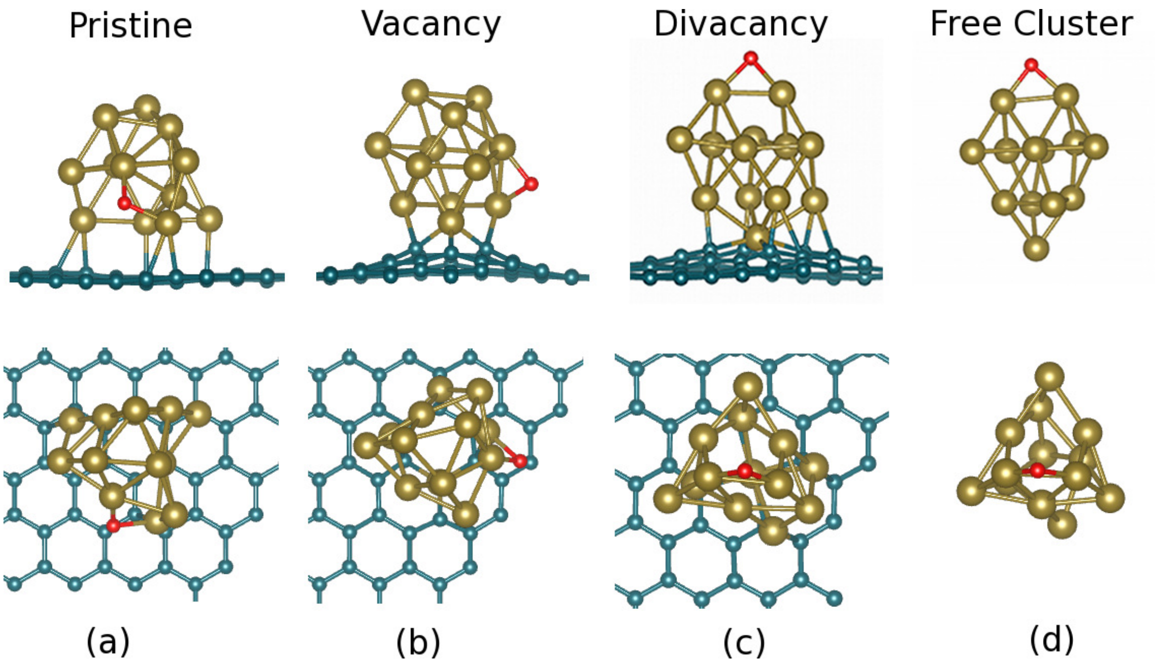

Figure 4.1: Side and top view of selected low energy DFT configurations for adsorption of an O atom on graphene-supported Pt_{13} clusters. Cyan, gold and red spheres represent C, Pt and O atoms, respectively.

lower by 0.21 eV and 0.52 eV, respectively, compared to the average adsorption energy on Pt_{13} clusters supported on defect-free pristine graphene; the difference in binding energies relative to unsupported Pt_{13} clusters is even larger (0.46 eV, and 0.77 eV, respectively). Similarly, the O adsorption energy on the Pt_{13} cluster supported on a SV and a DV is lower by 0.18 eV, and 0.24 eV, respectively, compared to pristine graphene and by 0.28 eV, and 0.34 eV relative to unsupported Pt_{13} clusters. The variability in the local atomic coordination of the low–energy Pt_{13} clusters results in variations in binding energy of $\sim 0.1 - 0.2$ eV for CO, and $\sim 0.2 - 0.4$ eV for O adsorption, an order of magnitude smaller than the binding energy. The remaining differences in O binding energies can then be attributed to the strong cluster–support interactions.

As discussed in Chapter 2, there exists a clear correlation between the position of the d-band center of the bound cluster and the nature of the support point defect.[45]

Specifically, stronger binding of the cluster to the defect (which is directly related to the number of dangling bonds at the defect) is accompanied by increased charge transfer from the cluster to the substrate and a shift of the cluster *d*-band center away from the Fermi level. In Figure 4.2, we correlate the *d*-band shift—which is effectively a metric of the cluster's tendency to form bonds with other adsorbates[124]—with the average CO and O adsorption energies. As seen from this figure, the position of the cluster *d*-band center is well correlated with both CO and O adsorption energies on graphene–supported Pt_{13} clusters: for defective substrates, the stronger cluster–support interaction compared to pristine graphene, leads to a downshift of the *d*-band center position which in turn weakens the CO and O adsorption on the cluster.

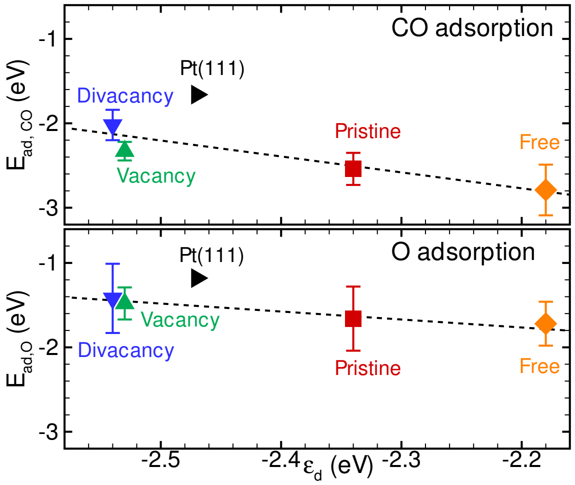

Figure 4.2: CO (top) and O (bottom) adsorption energy (E_{ad}) as a function of *d*-band center (ϵ_d) relative to the Fermi energy for supported Pt_{13} clusters, free Pt_{13} clusters, and Pt(111) surface. Error bars indicate 95% confidence intervals obtained from sampling over multiple adsorption sites on the clusters. CO adsorption energy results are adapted from Ref. [46].

Results from Bader analysis[13, 70] for O adsorption on graphene-supported and free Pt_{13} clusters are reported in Table 4.2 . Similarly to CO adsorption discussed in Chapter 3, there is an appreciable net charge transfer from the Pt_{13} cluster to both the graphene support and the O atom after O adsorption. The amount of charge transferred from the Pt cluster to O ($\sim 0.74e^-$) is found to be independent of the cluster interaction with graphene. The charge transferred from the Pt cluster to the support is, however, sensitive to the nature of the support; a cluster adsorbed on pristine graphene transfers only $\sim 0.06e^-$, compared to the significantly greater charge transfer from the cluster to a defective support ($\sim 0.44-0.73e^-$). As discussed in Chapter 2, it is this substantial depletion of charge from the cluster to the defective support that leads to a downshift of the *d*-band center relative to the Fermi level,[45, 46] which in turn results in weaker CO and O binding to the cluster.

Table 4.2: Average charge transfer [Δq (e$^-$)] from the Pt_{13} cluster to O and pristine graphene, single vacancy, and unreconstructed divacancy based on Bader analysis. (Positive/negative numbers indicate accumulation/depletion of electrons.)

	Δq (e$^-$)		
	substrate	cluster	O
pristine	0.06 ± 0.03	-0.81 ± 0.03	0.74 ± 0.02
vacancy	0.44 ± 0.03	-1.19 ± 0.04	0.76 ± 0.02
divacancy	0.73 ± 0.04	-1.47 ± 0.06	0.74 ± 0.02
free clusters	–	-0.74 ± 0.01	0.74 ± 0.01

4.3.2 Effect of CO-saturation on the stability of graphene–supported Pt_{13} clusters

The CO and O adsorption energy results reported in Table 4.1 revealed that CO binding to Pt_{13} nanoclusters is substantially stronger ($\sim 0.7 - 0.8$ eV) than O adsorption, both for graphene–supported and free Pt nanoclusters. Consequently, under normal operating conditions the Pt cluster is likely to be fully saturated by CO and subsequent reactions, including CO oxidation, will take place on CO-covered clusters. In this section, moving beyond the single CO molecule adsorption studies discussed in Chapter 3, we seek to investigate the support effects on the stability of CO–saturated Pt_{13} clusters on pristine and defective graphene. *Ab initio* molecular dynamics annealing and quenching simulations were performed for this purpose, as described in Section 4.2. The adsorption energy of the CO–saturated Pt_{13} clusters ($E_{ad,cluster}$) at each graphene substrate was calculated according to Equation 4.2 and a Bader analysis [13, 70] was performed, partitioning the total charge density between atoms, allowing to quantify the total charge transfer between the cluster, CO adsorbates, and the graphene support. The results are reported in Table 4.3. The fully relaxed atomic structures and the charge density difference plots for the graphene–supported and free CO–saturated Pt_{13} clusters are shown in Figure 4.3.

Table 4.3: Adsorption energy of the CO–saturated Pt_{13} clusters to the different graphene substrates is reported in the first column. Average charge transfer [Δq (e^-)] from the CO–saturated Pt_{13} cluster to the CO molecule and pristine graphene, single vacancy, and unreconstructed divacancy substrates based on Bader analysis. (Positive/negative numbers indicate accumulation/depletion of electrons.)

		Δq (e^-)		
	$E_{ad,cluster}$ (eV)	substrate	cluster	CO
pristine	-0.28	-0.35	-2.13	2.48
vacancy	-11.16	-0.23	-2.38	2.60
divacancy	-12.21	0.58	-3.05	2.48
free clusters		–	-2.23 ± 0.13	2.23 ± 0.13

The adsorption energy of CO–saturated Pt_{13} clusters in Table 4.3 and the relaxed atomic structures in Figure 4.3 reveal a very interesting outcome: for the case of a CO–saturated Pt_{13} cluster supported on pristine graphene that was subjected to the high temperature annealing–quenching and relaxation procedure, CO is found to intercalate between the cluster and the support and cause complete desorption of the cluster, potentially leading to catalyst loss. There is only a very weak interaction of the cluster with the pristine graphene support (E_{ad} = -0.28 eV) and the cluster is located 5.3 Å away from the support. Such cluster desorption does not occur when the Pt_{13} cluster is bound to a defective–graphene support; instead there is strong binding of the CO–saturated Pt_{13} cluster at a vacancy (E_{ad} = -11.16 eV) and a divacancy (E_{ad}

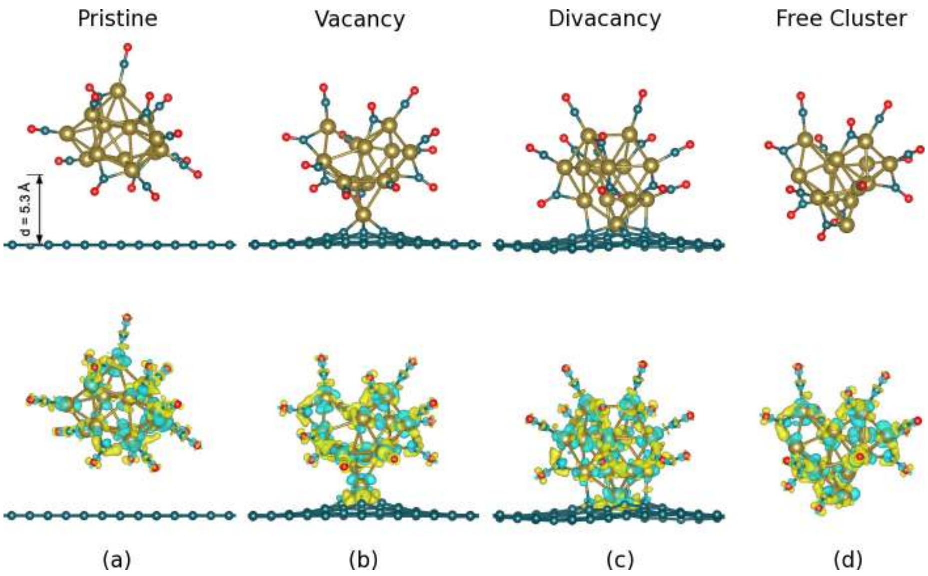

Figure 4.3: Fully relaxed atomic structures and charge-density difference plots for graphene–supported (a, b and, c) and free (d) CO–saturated Pt_{13} clusters. Isosurfaces are at 0.081 e/Å^3; yellow(blue) color represents charge accumulation(depletion). Cyan, gold and red spheres represent C, Pt and O atoms, respectively.

= -12.21 eV) in graphene. This observation further emphasizes the role of support defects in stabilizing catalyst clusters, even at CO saturation coverages, preventing sintering and/or catalyst loss.

From a different perspective, CO coverage is also expected to significantly influence the binding energies of the adsorbed species (CO molecules in this case). The adsorption energy per CO molecule ($E_{ad/CO}$) results for graphene–supported and free CO–saturated Pt_{13} clusters, calculated using Equation 4.3, are reported in Table 4.4. The single CO adsorption energy results from Chapter 3 (also reported in Table 4.1) are added here for direct comparison along with CO adsorption energy results on a Pt(111) surface.

Results from prior theoretical work on CO adsorption on Pt surfaces[6, 150] and large Pt clusters[6, 39] at different CO coverages essentially show that the adsorption energy decreases with increasing CO coverage, which is in agreement with our findings. More specifically, the study of Allian *et al.* [6] on a cuboctahedral Pt_{201} cluster,

Table 4.4: Adsorption energy per CO molecule on graphene–supported and free CO–saturated Pt_{13} clusters is reported in the first column. Single CO adsorption energy[46] on graphene–supported and free Pt_{13} clusters is reported in the second column. Results for CO adsorption at a Pt(111) surface are also included for comparison.

Graphene substrate	$E_{ad/CO}$ (eV)	$E_{ad_{CO}}$ (eV)
vacancy	-1.98	-2.33 ± 0.11
divacancy	-1.89	-2.02 ± 0.18
free clusters	-2.33	-2.79 ± 0.30
Pt(111)	-1.05	-1.80 (fcc), -1.66 (atop)

showed that the single CO adsorption energy (0 ML coverage) varies between -1.25 eV (on (111) terraces) and -1.79 eV (at corner sites) whereas at full CO–saturation, the adsorption energy per CO molecule decreases to -0.82 eV (on (111) terraces) and -1.49 eV (at corner sites). Large clusters such as the cuboctahedral Pt_{201} cluster, can be viewed as a combination of single crystal surfaces with high-coordinated adsorption sites (i.e., (111) and (100) terraces) and low-coordinated adsorption sites (i.e., steps and kinks). However, flat facets do not exist in ultra-small clusters, such as Pt_{13}; direct comparison is at best meaningful with low-coordination sites on the Pt_{201} cluster. In this regard, first, the prediction of stronger CO adsorption at atomic steps and kinks on Pt_{201} clusters compared to flat terraces is consistent with our observations, finding stronger CO adsorption on free Pt_{13} clusters compared to a single crystal Pt(111) surface. This was also pointed out in Chapter 3 for the case of single CO adsorption and it is now confirmed for higher CO coverages also. Second, both for free and graphene–supported Pt_{13} clusters the strength of CO adsorption weakens with increasing CO coverage, in agreement with prior computational studies. [6, 150] Compared with the single CO adsorption energy ($E_{ad_{CO}}$), the adsorption energy per CO molecule at CO–saturated Pt_{13} clusters is significantly lower (by, on average, 0.35, 0.13 and 0.46 eV for a vacancy substrate, a divacancy substrate and unsupported clusters, respectively). These differences reflect strong repulsive interactions between the adsorbed CO molecules on CO–saturated Pt_{13} clusters. Same behavior was observed on unsaturated and fully–CO–saturated Pt_{201} clusters.[6] Finally, further decrease of the CO adsorption on graphene–supported Pt_{13} clusters versus unsupported ones (both for a single CO and at full CO–coverage) can be attributed to the strong electronic interaction between the cluster and the point defects in graphene.[45, 46] Thus, weaker CO – cluster interaction for graphene–supported clusters at saturated CO coverages possibly suggests facile CO removal via CO oxidation on defective–graphene–supported Pt nanoclusters, which we consider next.

4.3.3 CO oxidation on defective-graphene supported and free CO–saturated Pt_{13} clusters

As shown in Section 4.3.2, CO–saturated Pt_{13} clusters bound at point defects in graphene are expected to remain strongly adsorbed to the support at full CO saturation. The significant defect-induced changes of the electronic structure of graphene–supported Pt_{13} clusters,[45, 46] are expected to have strong effects on the catalytic activity of these nanoclusters for the CO oxidation reaction. Therefore, the purpose of this section is to study in detail the kinetics of CO oxidation reaction with O_2 at CO–saturated Pt_{13} clusters supported at a single vacancy (SV) and a divacancy (DV) in graphene. The catalytic activity of graphene–supported clusters is then compared to the catalytic activity of CO–saturated free Pt_{13} clusters for the CO oxidation reaction.

Interestingly, there is a plethora of mechanisms described as most favorable in previous theoretical studies for the CO oxidation reaction with a single CO and O_2 molecule on metal–graphene systems.[95, 103, 114, 159, 193, 197] CO oxidation on defective–graphene–supported Au_8 and Pt_4 clusters was studied by Zhou *et al.*[197] via a L–H-type mechanism, with O_2 activation energies in the range of 0.1-0.2 eV.

Yuan *et al.*[193] found that CO oxidation on graphene–supported Pd–Au bimetallic clusters, proceeds via a two step mechanism ($CO^* + O_2^* \rightarrow O^*–O–C^*–O \rightarrow CO_2 + O^*$) that again involves the formation of a four-center metastable intermediate ($O^*–O–C^*–O$) with energy barriers of approximately 0.2 eV. Similar reaction mechanisms were found for CO oxidation on Au-embedded graphene[114] with an energy barrier of 0.31 eV and Cu-embedded graphene[159] with an activation energy of 0.25 eV. A different reaction path was identified on a theoretical study on Fe-embedded graphene[103] that showed the E–R mechanism to be the prevalent one, with a CO in the gas phase reacting with activated O_2^* ($CO + O_2^* \rightarrow CO_3^* \rightarrow CO_3^* + CO \rightarrow 2CO_2$) and the formation of a carbonate-like intermediate, CO_3^* with an activation energy of 0.58 eV. A similar E–R-type mechanism was identified as the most preffered reaction pathway for CO oxidation on Fe-anchored graphene oxide.[95] Finally, theoretical studies on CO oxidation at single Pt atom supported on defective graphene[170] and oxidized graphene[167] found that the reaction proceeds via a L–H-type mechanism ($CO^* + O_2^* \rightarrow O^*–O–C^*–O \rightarrow CO_2 + O^*$) as a first step, with energy barriers equal to 0.58 eV and 0.76 eV for defective graphene and oxidized graphene, respectively.

The theoretical studies discussed above are suggestive of the possible CO oxidation mechanisms encountered on metal–graphene systems. However, these refer to CO oxidation studies with a single CO and O_2 molecule. In our case, the most relevant kinetic mechanism that is found to prevail for CO–saturated clusters, is proposed by Allian *et al.*, [6] in which CO oxidation is expected to proceed via a CO*-assisted activation of the O_2 molecule. As described in Section 4.2, the CINEB method was employed to study the kinetics of CO oxidation reaction on graphene–supported and free CO–saturated clusters. In all cases, the initial state (IS) involves the presence of an O_2 molecule in the vicinity of the CO–saturated Pt_{13} cluster. Due to the variability in coordination of Pt atoms in the low–energy Pt_{13} clusters, there are several inequivalent sites for an O_2 molecule in the vicinity of the CO–saturated Pt_{13} cluster. Therefore we sampled several initial configurations for each graphene–supported and free CO–saturated Pt_{13} cluster. The final state (FS) corresponds to the formation of a CO_2 molecule in the gas phase and an oxygen chemisorbed on the cluster, O*.

First we discuss one case of the CO oxidation reaction at a CO–saturated Pt_{13} cluster supported at a single vacancy (SV) in graphene. The activation energy (E_a) is reported in Table 4.5 (SV - Case (a)). The corresponding atomic structure and the energy profile along the reaction coordinates are shown in Figure 4.4. The preferred reaction mechanism proceeds via the CO*– assisted O_2 activation in the vicinity of the CO–saturated Pt_{13} cluster. The O_2 activation is the rate limiting step, with an activation energy equal to 0.33 eV and the reaction follows a two-step scheme ($CO^* + O_2^* \rightarrow O^*\text{–}O\text{–}C^*\text{–}O \rightarrow CO_2 + O^*$) with the formation of a O*–O–C*–O complex which subsequently decomposes to CO_2 and an adsorbed O* species. The mechanism observed in the case of the CO–saturated Pt_{13} cluster supported at a single vacancy in graphene resembles the kinetic mechanism proposed by Allian *et al*[6] for CO oxidation at an unsupported cuboctahedral Pt_{201} cluster: neither the involvement of adsorbed O_2^* precursors nor O_2 dissociation are necessary; there is direct reaction of O_2 with pre-existing adsorbed CO* on the CO–saturated Pt_{13} cluster. The same reaction path was observed in separate sampled cases of CO oxidation at CO–saturated Pt_{13} clusters supported at a single vacancy, and the activation energy as calculated from the transition state calculations, was found in the range of 0.3–0.6 eV in all cases.

For completion, we discuss a different reaction mechanism that was also identified among the sampled cases of CO oxidation at CO–saturated Pt_{13} clusters supported at a single vacancy. The activation energy (E_a) for this case is reported in Table 4.5 (SV - Case (b)). The corresponding atomic structure and the energy profile along

Table 4.5: Activation energies (E_a) for the CO oxidation reaction on CO–saturated Pt_{13} clusters.

Graphene substrate	E_a (eV)
SV - Case (a)	0.33
SV - Case (b)	0.67
DV	0.43
Free cluster	1.97

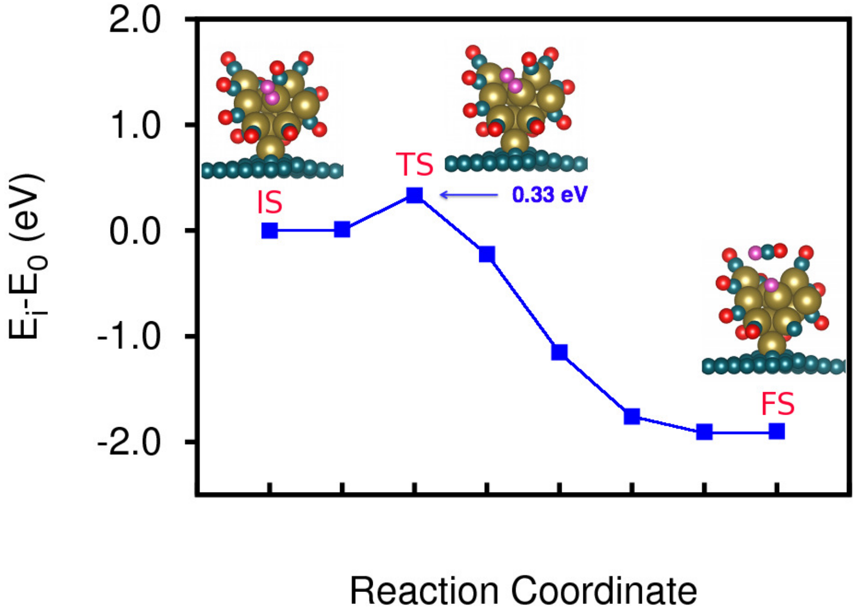

Figure 4.4: Minimum energy pathway and atomic structures for the CO oxidation reaction on a CO–saturated Pt_{13} cluster supported at a SV (Case (a)). Cyan, gold and red spheres represent C, Pt and O atoms, respectively. Pink spheres denote the O_2 molecule that participates in the reaction.

the reaction coordinates are shown in Figure 4.5. In this particular case the reaction proceeds via the formation of carbonate–like stable intermediate state, CO_3*. This mechanism is analogous to the mechanism observed in the study of CO oxidation at Fe-embedded graphene[103], Fe-anchored graphene oxide,[95] and a single Pt atom supported on pristine graphene,[170] with the distinction that the O_2 molecule in our case is activated with the assistance of pre-adsorbed CO*, instead of gas phase CO reacting with pre-adsorbed and activated O_2*, as in these prior reported studies.[95, 103, 170] Thus, the kinetic mechanism ($CO^* + O_2^* \rightarrow CO_3^* \rightarrow CO_2 + O^*$) involves the endothermic dissociation of the stable CO_3* intermediate into CO_2 and adsorbed O*. The energy barrier for the initial O_2 activation step was found equal to 0.67 eV, which is on the upper limit of the barriers calculated in the previously reported cases (0.3–0.6 eV) for CO oxidation at CO–saturated Pt_{13} clusters supported at a single vacancy in graphene. In addition, the requirement for overcoming a second energy barrier before dissociation to CO_2 and O* implies that this reaction mechanism is unlikely to be the preferred pathway for CO oxidation reaction at CO–saturated Pt_{13} clusters supported at a single vacancy.

Next, we discuss the preferred mechanism for CO oxidation at a CO–saturated Pt_{13} cluster supported at a divacancy (DV) in graphene. The activation energy (E_a) is reported in Table 4.5 (DV). The corresponding atomic structures along with the energy profile along the reaction coordinates are shown in Figure 4.6. In the case examined here, the reaction proceeds in a similar manner with the CO oxidation at a CO–saturated Pt_{13} cluster supported at a single vacancy in graphene; the rate limiting step involves the CO*– assisted O_2 activation with an energy barrier equal to 0.43 eV, followed by formation of a O*–O–C*–O complex that exothermically dissociates to chemisorbed O* and CO_2. The other sampled cases for CO oxidation at CO–saturated Pt_{13} clusters supported at a divacancy (DV) in graphene adopt the

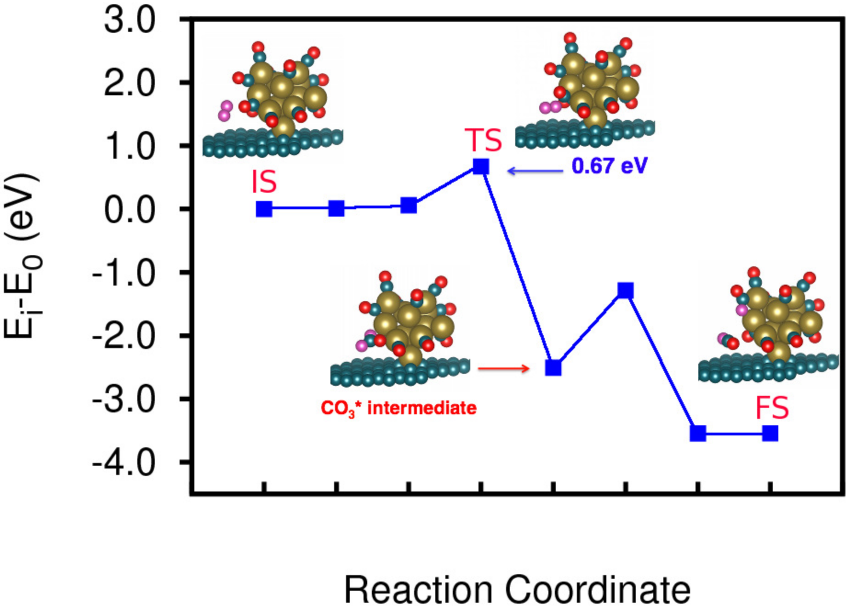

Figure 4.5: Minimum energy pathway and atomic structures for the CO oxidation reaction on a CO–saturated Pt_{13} cluster supported at a SV (Case (b)). Cyan, gold and red spheres represent C, Pt and O atoms, respectively. Pink spheres denote the O_2 molecule that participates in the reaction.

same reaction steps and the activation energies were calculated in the range of 0.4–0.6 eV in all cases.

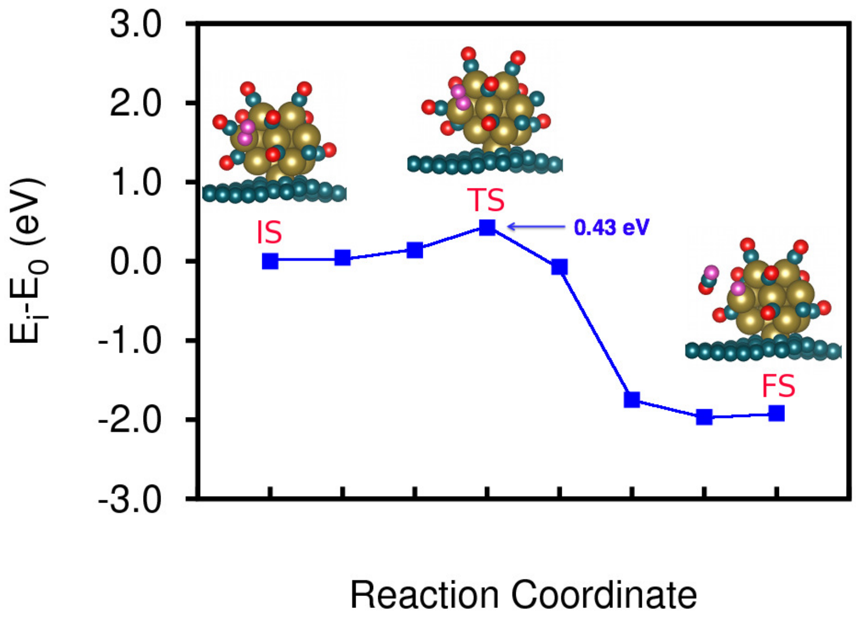

Figure 4.6: Minimum energy pathway and atomic structures for the CO oxidation reaction on a CO–saturated Pt_{13} cluster supported at a DV. Cyan, gold and red spheres represent C, Pt and O atoms, respectively. Pink spheres denote the O_2 molecule that participates in the reaction.

As a last part of this discussion, we focus on the CO oxidation on free CO–saturated Pt_{13} clusters. The activation energy (E_a) for the sampled case shown in Figure 4.7, is reported in Table 4.5. The observed mechanism for CO oxidation at unsupported CO–saturated Pt_{13} clusters again involves the CO*– assisted O_2 activation and formation of a O*–O–C*–O complex that dissociates to chemisorbed O* and CO_2. However, the reaction in this case requires significantly higher activation energies ($\sim 1.12 - 1.97$ eV) compared to CO–saturated Pt_{13} clusters bound at point defects in graphene. The results for unsupported CO–saturated Pt_{13} clusters can be qualitatively compared to the study of Allian *et al.* [6] on Pt_{201} clusters. The low-energy Pt_{13} clusters employed in our study are structurally different from cuboctahedral Pt_{201} clusters in that the latter contain a representative distribution of well-defined (111) and (100) terrace, corner and edge sites. However, our results for CO oxidation at unsupported CO–saturated Pt_{13} clusters are in overall agreement with their reported activation energies at edge (1.36 eV) and corner (1.48 eV) sites of Pt_{201} clusters.

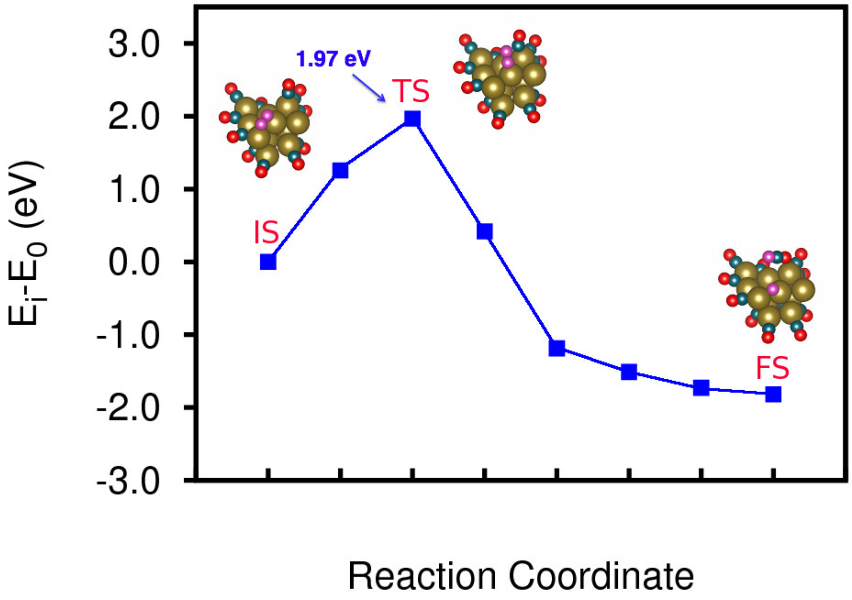

Figure 4.7: Minimum energy pathway and atomic structures for the CO oxidation reaction on an unsupported CO–saturated Pt_{13} cluster. Cyan, gold and red spheres represent C, Pt and O atoms, respectively. Pink spheres denote the O_2 molecule that participates in the reaction.

To summarize, in this section we identified the preferred reaction pathway for CO oxidation at defective–graphene–supported and free CO–saturated Pt_{13} clusters. Our simulations showed that O_2 activation occurs via CO*–assisted steps, without the requirement for adsorption or O_2 dissociation. The reaction proceeds with the formation of a O*–O–C*–O complex that exothermically dissociates to CO_2 and chemisorbed O* species. CO oxidation on unsupported CO–saturated Pt_{13} clusters requires significantly higher activation energies ($\sim 1.12 - 1.97$ eV) compared to CO–

saturated Pt_{13} clusters bound at point defects in graphene ($\sim 0.3 - 0.6$ eV). The outcome of these studies validates our initial expectation for the substrate effect on the catalytic activity of graphene-supported clusters: the strong interaction of CO–saturated Pt_{13} clusters with point defects in graphene and the modification of their electronic structure, greatly enhances their catalytic activity towards CO oxidation, at high CO coverage. Low–energy defective–graphene–supported CO–saturated Pt_{13} nanoclusters are identified as effective catalysts for CO reduction with significantly lower activation energies than unsupported clusters.

4.4 Conclusions

In conclusion, DFT calculations were employed to investigate the support effects on the catalytic CO–oxidation at CO–saturated graphene–supported Pt_{13} clusters. Defective graphene is found to enhance the stability of CO–saturated Pt_{13} clusters, preventing sintering and potential catalyst loss. The relevant kinetic mechanism for CO oxidation reaction with O_2 at CO–saturated graphene–supported Pt_{13} clusters was studied in detail: the rate limiting step involves the CO*– assisted O_2 activation, followed by formation of O*–O–C*–O reactive intermediates that decompose to chemisorbed oxygen and CO_2. The strong interaction of Pt_{13} clusters with point defects in graphene lowers the required activation energy for the CO oxidation reaction by more than 0.5 eV compared to unsupported clusters. Overall, our study suggests that defect-engineered graphene can not only serve as robust catalytic support that strongly binds and stabilizes clusters against sintering, but also allows for tuning of catalytic properties through cluster-substrate interactions.

CHAPTER 5

SUMMARY, CONCLUSIONS AND FUTURE WORK

5.1 Summary

The aim of this thesis was to obtain a fundamental and quantitative understanding of the complex phenomena that dominate the properties of Pt–graphene nanocomposites as electrocatalysts in fuel cells. Through a synergistic combination of computational techniques, we analyzed in detail the support effects on the structural, electronic and catalytic properties of Pt nanoclusters bound at various point defects in graphene. The most significant findings and the key contributions from this thesis are discussed in this chapter.

First, we investigated the binding energetics and the morphology of low-energy isomers of small Pt_n, (n=1,2,3,4,13), clusters on defect-free and defective graphene substrates. The results of our study showed that point defects in graphene act as strong anchoring sites for Pt nanoclusters. Additionally, low–energy isomers of graphene-supported Pt nanoclusters were identified via Molecular Dynamics annealing and structural relaxation. Supported Pt clusters were shown to adopt open, low-symmetry morphologies, as a result of support-induced morphological distortions after adsorption. Besides, the electronic structure analysis revealed a clear tendency for significant charge transfer from the Pt cluster to the graphene support upon adsorption. The strong electronic interaction between the Pt cluster and the point defect in graphene resulted in a downshift of the cluster *d*-band center position relative to the Fermi level, which is expected to further affect the catalytic activity of the cluster.

Next, the support effect on the CO and O adsorption on Pt_{13} clusters supported on defect-free and defective graphene substrates was investigated via detailed DFT calculations. Pt_{13} clusters that bind strongly to defects in graphene, were shown to subsequently bind CO and O more weakly as compared to clusters supported on pristine graphene or unsupported clusters. As a result, defective-graphene supported Pt clusters are expected to show increased tolerance to CO poisoning. These observations were explained in terms of the downshift of the cluster *d*-band center position with respect to the Fermi level, upon binding to defects: stronger binding leads to greater charge transfer from the cluster to the substrate accompanied by a greater downshift of the *d*-band center, which in turn weakens the CO and O adsorption. Comparison between CO and O adsorption results, indicated that CO adsorption prevails. Consequently, the effect of CO-saturation on the stability of graphene-supported Pt clusters was also considered and our results essentially showed that support defects are crucial in stabilizing the Pt_{13} clusters at high CO-coverages, preventing potential catalyst loss.

In the last part of our study, we addressed the support effects on the kinetics of CO oxidation on CO–saturated graphene–supported Pt_{13} clusters. Detailed DFT calculations were performed and the preferred reaction pathway for CO oxidation at defective–graphene–supported and free Pt_{13} clusters in the CO saturation regime was identified. Our simulations showed that the rate limiting step involves CO*–assisted O_2 activation, without the involvement of adsorbed O_2* precursors or O_2 dissociation, followed by the formation of O*–O–C*–O reactive intermediates that decompose to chemisorbed oxygen and CO_2. The reaction kinetics results clearly showed that defective graphene reduces the activation energy for the CO oxidation by more than 0.5 eV compared to unsupported clusters. Consequently, Pt_{13} clusters supported on defective graphene are found to show greatly enhanced catalytic activity towards CO oxidation, in the high CO coverage regime.

In summary, the findings presented in this thesis provide important insights into the role of graphene as a catalytic support for Pt nanoparticles. Our study established that defect-engineered graphene can serve as robust catalyst support that strongly binds and stabilizes Pt clusters against sintering, and also allows for optimizing catalytic properties through tuning of cluster–support interactions.

5.2 Conclusions

The urgent demand for new energy technologies has greatly exceeded the capabilities of existing materials and chemical processes. Computational modeling plays an essential role in simulating and accurately predicting the performance of advanced materials that are critical elements for progress in advanced energy systems. In this thesis, computational modeling of Pt-graphene nanocomposites provides useful insights into the structural, electronic and catalytic properties of these materials. More specifically, the main contributions of this thesis are summarized below:

- The presence of point defects in graphene supports greatly enhances the binding of Pt_{13} nanoclusters at the site of the defect. The strong interaction of Pt_{13} nanoclusters with defects in graphene can therefore inhibit cluster sintering and prevent catalytic active surface area loss.

- There are support-induced effects on the morphology of graphene–supported Pt_{13} nanoclusters as a result of adsorption at point defect sites in graphene. Determination of optimal cluster structure in our studies reveals information about the electronic structure and catalytic activity of realistic Pt clusters.

- There are support-induced effects on the electronic structure of graphene–supported Pt_{13} nanoclusters after adsorption; the strong binding of the cluster at the defect site, the formation of strong Pt-C bonds, and charge redistribution at the cluster-support interface are accompanied by a significant downshift of the cluster *d*-band center position relevant to the Fermi level. The correlation of the cluster *d*-band center position with the average CO and O adsorption energies on graphene-supported Pt nanolcusters, could explain the experimentally observed increased tolerance to poisoning for Pt nanoclusters on graphene supports.

- The relevant kinetic mechanism for CO oxidation on graphene–supported Pt_{13} nanoclusters in the high CO coverage regime was identified and detailed transition state calculations were performed. CO reduction on defective-graphene–supported Pt_{13} nanoclusters requires significantly lower activation energy than unsupported Pt_{13} nanoclusters, indicating that there are support-induced effects on the catalytic activity of graphene–supported Pt_{13} nanoclusters for the CO oxidation reaction.

In conclusion, the results of the computational studies presented in this thesis explain the effect of defective–graphene supports on various properties of graphene–supported subnanometer size Pt nanoclusters. Through systematic cluster optimization, electronic structure analyses and transition state calculations, we are able to explain the experimentally observed increased stability and catalytic activity of Pt nanoclusters on graphene. We expect that the results of our studies will guide the design of efficient graphene–supported Pt nanocatalysts with desired and tailored properties.

5.3 Future Directions

Graphene-based nanomaterials show great promise as electrocatalysts in fuel cells. However, the area of graphene-supported catalysis is still premature, albeit rapidly developing. Additional studies are necessary to establish a better understanding of the properties of graphene nanocomposites in catalysis, that will allow for their extensive use in commercial applications. In this Section we discuss some proposed future directions.

- **Computational Studies of CO oxidation on Pt nanoclusters supported on Graphene Oxide**

  As part of this dissertation we have explored the preferred kinetic mechanism for CO oxidation on small CO-saturated Pt nanoclusters supported on defective graphene. One interesting suggestion for future work is to extend our studies on graphene oxide supports. The role of functional groups is already highlighted in experiments, showing promise for graphene-oxide - based metal nanoparticles as electrocatalysts.[28, 84, 101, 153] Therefore, we would like to investigate in detail the effect of functional groups that are present in graphene oxide on the stability and catalytic activity of supported Pt nanoparticles for electrochemical reactions such as CO oxidation. The elementary steps of this study will account for small Pt nanoparticles and explore the support-induced effects in the morphology and electronic properties of the clusters. Subsequently, the study will proceed with a detailed investigation of the kinetic mechanism for CO oxidation on graphene-oxide supported Pt nanoclusters. Effects induced by CO and/or O coverage and the presence of functional groups will be also characterized.

- **Computational Studies of Methanol Decomposition on Graphene-supported Pt nanoclusters**

  Similar to CO oxidation, computational studies of methanol decomposition have focused mainly on Pt surfaces, assuming vapor-phase chemistry[55, 56] or an aqueous solution.[23] Our results on CO oxidation kinetics on small graphene-supported Pt nanoparticles could provide a useful guidance for other electrochemical reactions, that are encountered in a fuel cell environmnent. In particular, investigating in detail the kinetics of methanol decomposition on graphene-supported Pt nanoclusters, is of great interest and direct relevance to the development of superior electrocatalysts for DMFCs. As a first step, the study will focus on identifying the interplay between the energetics and kinetics of methanol decomposition with the morphology and electronic structure of the supported nanoparticle. Methanol decomposition involves several intermediate steps and the kinetics of all the individual steps need to be investigated. Therefore, combined with the distinct morphology of nanoparticles compared to single crystal surfaces, the level of complexity in the system is expected to rise significantly. Thereafter, the study should be extended to an aqueous solution environment, to account for additional effects due to the presence of ionic liquids. Completion of these studies could provide a detailed understanding of the support effects in the catalytic activity of supported nanoparticles for complex electrochemical reactions.

Undoubtedly, there are endless possibilities when it comes to new materials that could be explored for applications in catalysis. Although platinum and other noble metals are the materials of choice for several electrocatalytic reactions, the use of noble metals imposes limitations due to their high cost. Therefore, finding alternatives to noble metal nanoparticles as catalytic materials is of utmost importance. Investigating graphene-based hybrid materials with lower precious metal content and potentially improved catalytic activity, is another direction for future work.

APPENDIX A

EDGE STRESSES OF NON-STOICHIOMETRIC EDGES IN TWO-DIMENSIONAL CRYSTALS

APPLIED PHYSICS LETTERS **100**, 251906 (2012)

Edge stresses of non-stoichiometric edges in two-dimensional crystals

Junkai Deng,[1] Ioanna Fampiou,[2] J. Z. Liu,[3] Ashwin Ramasubramaniam,[2,a)]
and N. V. Medhekar[1,b)]
[1]*Department of Materials Engineering, Monash University, Clayton, Victoria 3800, Australia*
[2]*Department of Mechanical and Industrial Engineering, University of Massachusetts Amherst, Amherst, Massachusetts 01003, USA*
[3]*Department of Mechanical and Aerospace Engineering, Monash University, Clayton, Victoria 3800, Australia*

(Received 12 April 2012; accepted 4 June 2012; published online 20 June 2012)

The elastic properties of edges are among the most fundamental properties of finite two-dimensional (2D) crystals. Using a combination of the first-principles density functional theory calculations and a continuum elasticity model, we present an efficient technique to determine the edge stresses of non-stoichiometric orientations in multicomponent 2D crystals. Using BN and MoS_2 as prototypical examples of 2D binary monolayers with threefold in-plane symmetry, we unambiguously compute unique edge stresses of commonly observed non-stoichiometric edges. Our results show that the edge stresses for these structurally distinct orientations can differ significantly from the average values that have been typically reported to date. © *2012 American Institute of Physics*. [http://dx.doi.org/10.1063/1.4729940]

The recent experimental realization of atomically thin two-dimensional (2D) monolayers of graphene,[1] boron nitride,[2,3] and transition metal dichalogenides[4,5] has sparked extensive interest in characterizing the unique properties of these materials as well as their crystalline defects. In particular, edges in 2D monolayers display physical, chemical, and electronic properties that are distinct from the pristine monolayers.[6–8] The bonding environment for atoms at free edges differs significantly from the bonding environment in the bulk of the monolayer. Consequently, the edges of 2D monolayers are typically in a state of tensile or compressive stress whose magnitude intimately depends upon the atomic structure of the edge. Recent experiments[9–11] and theoretical calculations[12–15] have shown that edge stresses can lead to a spontaneous structural instability in the monolayer in the form of rippling and warping, which can potentially influence the electronic and chemical properties of the edges and their vicinity. It is therefore critical that the mechanical and electronic properties of thermodynamically stable edge orientations are accurately characterized.

For a 2D monolayer, the edge stress for a particular edge orientation θ is generally obtained by constructing a model nanoribbon terminated with two parallel edges oriented along θ and $\theta + 180°$.[12,13,15] When an in-plane strain ε is applied along the direction of the free edges of a nanoribbon of length L and width W, the potential energy of the nanoribbon up to the quadratic order in strain is given by

$$U(\varepsilon, W) = U_0 + \frac{1}{2}ELW\varepsilon^2 + (\tau_1 + \tau_2)L\varepsilon + \frac{1}{2}(E_{e1} + E_{e2})L\varepsilon^2, \tag{1}$$

where U_0 is the potential energy at zero strain, E is the bulk 2D elastic modulus of the monolayer, and $\tau_{1(2)}$ and $E_{e1(2)}$ denote the edge stress and edge elastic modulus of edge 1(2), respectively. The change in potential energy as a function of applied strain can be accurately calculated by first-principles methods to obtain various edge properties via fitting to Eq. (1). It is clear that this strategy can be employed to unambiguously determine edge properties when the two edges at θ and $\theta + 180°$ are structurally identical (e.g., graphene with zigzag or armchair edges[12–16]). However, for multicomponent 2D materials such as BN or transition metal dichalcogenides such as MoS_2 with threefold in-plane symmetry, the parallel edges with orientations θ and $\theta + 180°$ are, in general, non-stoichiometric and *structurally distinct* from each other. The stoichiometric BN zigzag nanoribbon with boron-terminated $(\bar{1}010)$ and nitrogen-terminated $(10\bar{1}0)$ zigzag edges provides a representative example. The electronic states at B and N edges differ significantly; therefore, the edge stresses can also be expected to differ substantially. In such situations, Eq. (1) only yields *average* values of edge stresses/moduli for orientations θ and $\theta + 180°$ rather than their distinct edge properties.[17] As a result of this limitation, only average values of edge stresses for zigzag edges of BN and SiC monolayers have been reported in the literature,[18–20] while the unique value of the edge stress for each distinct orientation remains unknown.

In this letter, we propose an effective technique using a combination of first principles calculations and a continuum elasticity model to unambiguously determine edge stresses for non-stoichiometric edge orientations in multi-component 2D monolayers. Taking zigzag edges of BN as a prototypical system, we have determined the individual edge stresses of B- and N-terminated edges. A comparison with the average edge stress of zigzag BN nanoribbon demonstrates the accuracy of our approach. Finally, we implement the approach developed here to determine edge stresses of commonly observed non-stoichiometric edges of monolayer MoS_2. Our results suggest that the edge stresses of individual non-stoichiometric orientations can be significantly different from the average values typically computed using a nanoribbon model.

[a)] Electronic mail: ashwin@engin.umass.edu.
[b)] Author to whom the correspondence should be addressed. Electronic mail: nikhil.medhekar@monash.edu.

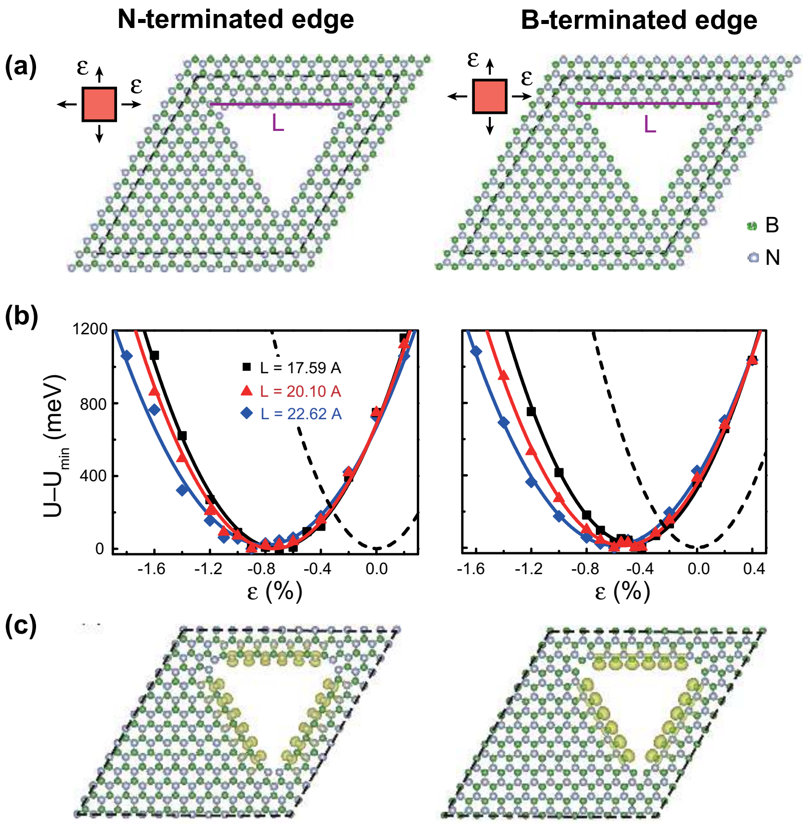

FIG. 1. (a) Schematic of monolayer BN with triangular holes with zigzag $(10\bar{1}0)$ N-edges (left) and $(\bar{1}010)$ B-edges (right). The dotted lines denote a 13×13 BN periodic supercell. (b) Variation of potential energy of the supercell with equibiaxial strain ε. The change in potential energy for a pristine BN monolayer BN (dashed lines) is also shown for comparison. (c) Localization of spin density at the N- and B-edges; yellow isosurfaces are plotted at a spin density of $0.005\, e^-/\mathrm{Bohr}^3$.

The key for unambiguous determination of the edge elastic properties of non-stoichiometric edges lies in constructing a model that *only* includes edges with the specific orientation of interest. For 2D monolayers with a threefold in-plane symmetry, such a model can be realized by a triangular-shaped flake (a triangular "quantum dot") or a planar sheet with a triangular hole terminated with identical edges. While either the triangular flake or hole can be used to determine surface energies,[21] the model with a triangular hole offers a unique advantage for determining edge stresses and edge moduli. In the model with a triangular hole, homogeneous strains can be conveniently applied while simultaneously allowing for complete atomic relaxation of the free edges. Therefore, we choose planar sheets containing triangular holes with different edge terminations as our model to determine edge elastic properties of non-stoichiometric edges. Figure 1 schematically illustrates one such periodic supercell of a BN monolayer with zigzag B and N edges.

When compared with the strained nanoribbon (Eq. (1)), the biaxially strained periodic supercell shown in Fig. 1 has three additional contributions to the total energy: (1) the strain dependence of the excess energy of the corners, (2) the elastic interaction energy due to the relaxation of the strain field near the edges and corners, and (3) the energy of elastic interaction between periodic images of the triangular hole. The total potential energy as a function of equibiaxial strain ε is

$$U(\varepsilon, A_{cell}, L) = U_0 + U_B(\varepsilon, A_{cell}, L) + 3(\tau L + E_C^{'})\varepsilon + \frac{3}{2}(E_e L + E_C^{''})\varepsilon^2, \quad (2)$$

where U_0 is the potential energy at zero strain, A_{cell} is the area of the periodic cell, L is the edge length of the equilateral triangular hole, τ is the edge stress, and E_e is the edge elastic modulus. The term U_B denotes the contribution from the elastic energy of the 2D bulk material and can be written as $U_B(\varepsilon, A_{cell}, L) = M(A_{cell} - \sqrt{3}L^2/4)\varepsilon^2 + U_{int}(\varepsilon, A_{cell}, L)$, where $M = E/(1-\nu)$ is the biaxial modulus of the monolayer, ν is Poisson's ratio, and U_{int} accounts for the elastic energy of interaction between defects. It should be noted that the energy U_B is independent of the atomic structure of the edge and depends only on the applied strain, geometrical parameters, and elastic properties of bulk 2D monolayer. Consequently, U_B can be calculated exactly for any configuration using a continuum elasticity model. The corners of the hole, being regions of stress concentration, are particularly susceptible to bond stretching and bond-angle distortions. These effects are not captured by the classical linear elastic terms in U_B and so we explicitly account for these higher-order effects by expanding the corner energy E_C to second order in strain. Once the total potential energy is obtained as a function of ε and L, the edge elastic properties can be readily computed via fitting to Eq. (2).

First, we apply this method to compute edge stresses for the zigzag $(\bar{1}010)$ B-edge and $(10\bar{1}0)$ N-edge of monolayer BN (Fig. 1). Our total energy calculations were performed using spin-polarized density functional theory (DFT) as implemented in the software package VASP.[22] Electron exchange and correlation were described using the generalized-gradient approximation of the Perdew-Burke-Ernzerhof form[23] and projector-augmented wave potentials were used to treat core and valence electrons.[24,25] In all cases, we employed a plane-wave kinetic energy cutoff of 400 eV. As shown in Fig. 1(a), two periodic 13 × 13 BN supercells containing triangular holes with B- and N-terminated zigzag edges were constructed at the optimized lattice parameter of $a = 2.513$ Å. In each case, a small in-plane biaxial strain ε was uniformly applied and all ionic positions were optimized until the Hellmann-Feynman forces were less than 0.01 eV/Å. For a particular hole size L and strain ε, the energy term U_B was then computed using a finite element model with 2D bulk elastic modulus $E = 19.86$ eV/Å^2 and Poisson's ratio $\nu = 0.17$ which were obtained from DFT calculations on a pristine monolayer BN. Our computed values for both the lattice parameter and the elastic properties of monolayer BN are in close agreement with experiments[3] and earlier DFT studies.[18,19] Finally, the edge stress τ was then extracted by fitting Eq. (2) to the variation of U–U_B versus hole size L.

Fig. 1(b) shows the variation in total energy as a function of applied strain for three different hole sizes. From thermodynamics, it follows that the potential energy of an infinite 2D monolayer at 0 K must have a minimum at zero strain. In contrast, as Fig. 1(b) shows, the potential energy displays a minimum at compressive strains of approximately −0.5% and −0.8% for sheets containing holes with zigzag B- and N-edges, respectively. A careful examination of Eq. (2) suggests that the magnitude and sign of the residual strain depends not only on the structure of the edge (equivalently the edge stress τ), but also on elastic interactions between holes ("defects") as well as the strain dependence of the corner energy. This is in distinct contrast to nanoribbons where the residual strain depends only on the structures of the edges and their effective elastic moduli. Table I shows the extracted values of the edge stresses for zigzag B- and N-edges obtained via fitting to Eq. (2). It is clear that the edge stresses for both the edges are compressive. The large compressive stress for $(10\bar{1}0)$ N-edge (−0.99 eV/Å) results from a distortion of BN hexagons near the free edges such that B-N bonds at the N-edge are shorter by ∼2% than the bonds in the interior domain. The BN hexagons with $(\bar{1}010)$ B-edges distort to a smaller extent (bonds are shorter by ∼1% than in the interior) than those at N-edges resulting in a lower edge stress for the B-edge. However, due to a large difference between the edge stresses of these distinct terminations, the average edge stress of −0.6 eV/Å is sufficiently different from that of either edge and does not accurately reflect the deformation of the BN lattice near the individual zigzag edges. Furthermore, it is interesting to note that the average value of edge stress for BN zigzag edges (−0.6 eV/Å) shown in Fig. 1 is close to the edge stress for the stoichiometric low-energy armchair edge orientation (−0.55 eV/Å[18]). In Fig. 1(c), we also present the spatial distribution of the spin density localized at the B- and N-edges. With a net magnetic moment of ∼1 μ_B per edge B or N atom, the magnitude for ferromagnetic ordering is identical for both B- and N-edges.

TABLE I. Edge stress τ for the N-terminated and B-terminated zigzag boron nitride edges obtained from the triangular hole model (Figure 1).

Edge stress τ (eV/Å)	
N-terminated zigzag edge	B-terminated zigzag edge
−0.99 ± 0.006	−0.22 ± 0.005

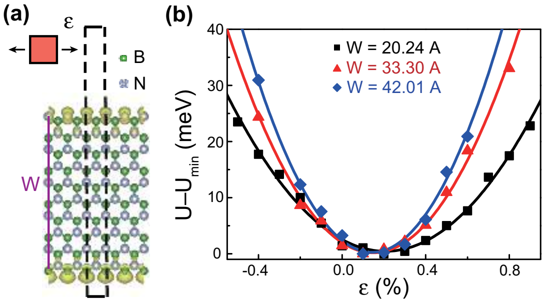

FIG. 2. (a) Schematic of a BN nanoribbon with zigzag N- and B-edges. The dashed lines indicate the periodic supercell. The localization of the spin density at the edges is also shown; yellow isosurfaces indicate spin density of 0.005 e^-/Bohr^3. (b) Variation of the potential energy of the BN nanoribbon with uniaxial strain ε for three different widths W.

To verify the accuracy of the method presented above for computing edge stresses for individual $(\bar{1}010)$ B-edges and $(10\bar{1}0)$ N-edges, we have also computed the average edge stress directly from a simulation of a zigzag BN nanoribbon (Fig. 2). The average edge energy is given by $\gamma = (U - N_{BN}E_{BN})/2L$, where U is the total energy at zero strain, N_{BN} the number of BN pairs, and E_{BN} is the potential energy per BN pair in a pristine BN monolayer. Our calculated average edge energy of 1.21 eV/Å agrees well with earlier reported results.[18,20] Fig. 2(a) also shows the distribution of spin density localized near the free edges. The nanoribbon is in a ferromagnetic state and the spin population analysis assigns a net magnetic moment of ∼1 μ_B per edge atom for both B- and N-edges. Therefore, both B and N atoms at the free edges in the triangular hole model (Fig. 1) and the nanoribbon model (Fig. 2) are in identical electronic and magnetic states, thus facilitating a meaningful comparison between the elastic properties obtained by the two approaches. For the nanoribbon model, a uniform strain ε was applied along the length of the ribbon, and the total energy was calculated using spin-polarized DFT. Fig. 2(b) shows the variation of the potential energy for different ribbon widths. It is clear that for all nanoribbon widths, the edge stress is compressive. By fitting to Eq. (1), the average edge stress for zigzag B- and N-edges was obtained as −0.52 ± 0.018 eV/Å. From the values listed in Table I, we see that the average edge stress for the BN zigzag nanoribbon (−0.52 eV/Å) agrees reasonably well with the average value of the edge stresses of individual edges obtained via the triangular hole model (−0.60 eV/Å). Finally, we have also computed the edge stress for the stoichiometric armchair BN edge using both a triangular hole model and a nanoribbon model. We find that the edge stress obtained using the triangular hole model ($-0.39\,\mathrm{eV/\AA}$) agrees well with the value obtained independently from the nanoribbon model ($-0.41\,\mathrm{eV/\AA}$), thus providing a self-consistent check supporting the accuracy of our approach.

A recent DFT study has pointed out the existence of a variety of non-equivalent magnetic configurations in bare zigzag BN nanoribbons.[26] These configurations include ferromagnetic ordering at both B- and N-edges (the case considered here), and antiferromagnetic ordering at the B-edge with ferromagnetic ordering at N-edge, among others. The energy differences of all magnetic configurations were reported to be within 7 meV/atom, thus suggesting that all configurations are thermally accessible at room temperature.[26] Using DFT simulations based on basis sets, Jun *et al.* reported an average tensile edge stress of $0.32\,\mathrm{eV/\AA}$ for nonmagnetic zigzag BN nanoribbons.[18,27] In another DFT study, Huang *et al.* reported an average tensile edge stress of $0.64\,\mathrm{eV/\AA}$ for a zigzag nanoribbon with ferromagnetic N-edge and antiferromagnetic B-edge.[20] In contrast to these studies, we find that the edge stress is compressive for both B- and N-terminated zigzag edges with ferromagnetic ordering being preferred. As shown in Figs. 1 and 2, the magnetic states at B- and N-edges for both triangular holes and nanoribbons are identical and yield a consistent sign and magnitude of edge stress. Thus, it is evident that both the magnitude and sign of the edge stress—and the resulting structural instabilities—crucially depend upon magnetic ordering at the edge.

Having verified the accuracy of our approach for determining edge stresses for individual non-stoichiometric edges in BN, we next focus our attention on commonly observed edges in MoS_2 monolayers.[6,28–30] So far, the edge elastic properties of single-layer MoS_2 have not yet been reported in the literature. In particular, we will investigate two non-stoichiometric high-symmetry edges: the $(\bar{1}010)$ sulfur edge (S edge) and the $(10\bar{1}0)$ molybdenum edge (Mo edge). The $(10\bar{1}0)$ Mo edge exposes a row of Mo atoms that are coordinated with only four S atoms rather than six as in the bulk. The bare $(10\bar{1}0)$ Mo edge with unsaturated bonds is energetically unstable and is usually not observed. It has been shown that the clean $(10\bar{1}0)$ Mo edge can be saturated with extra S atoms in two ways: with an S-dimer termination consisting of an additional row of dimerized S atoms or the S-monomer termination with half the number of S atoms reconstructed in-plane with a 2×1 periodicity (Fig. 3).[28–30]

For the pristine MoS_2 monolayer, we obtained an optimized lattice parameter $a = 3.19\,\mathrm{\AA}$, elastic modulus $E = 7.434\,\mathrm{eV/\AA^2}$, and Poisson's ratio $\nu = 0.25$. The optimized lattice parameter is in good agreement with earlier reported values.[30–32] As in the case of BN zigzag edges, the edge stresses for individual non-stoichiometric edges can be obtained in a straightforward manner by constructing periodic MoS_2 supercells with a triangular hole terminated with various edges of interest. However, as we explain next, the equivalence between the computation of edge elastic properties of the nanoribbon and the triangular hole offers a more convenient way of determining the edge stresses for all the edges of interest here with a minimal number of expensive DFT calculations. In this approach, the edge stress for the $(\bar{1}010)$ S edge is first obtained via the triangular hole method. Then, a nanoribbon terminated with one $(\bar{1}010)$ S edge and either a $(10\bar{1}0)$ Mo edge with S-monomer or S-dimer termination is constructed to obtain the average edge stress of the $(\bar{1}010)$ S edge and the $(10\bar{1}0)$ Mo edge with S-monomers/dimers. The nanoribbon calculation is computationally much cheaper than the hole in a large 2D sheet. Knowing the edge stress for one edge from the hole calculation, the edge stress for the remaining edge is readily obtained from the nanoribbon average value.

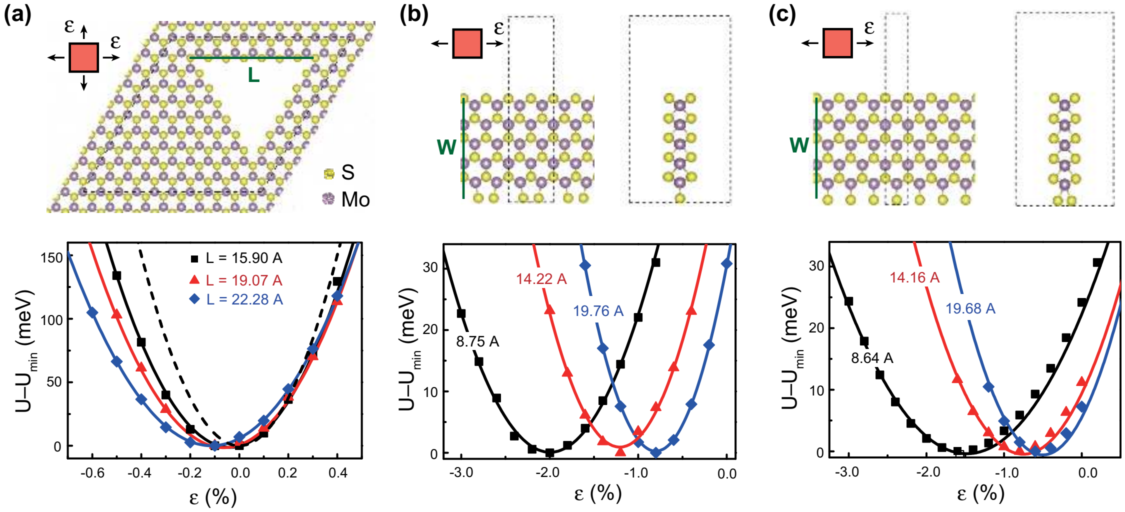

FIG. 3. (a) Variation of the potential energy with equibiaxial strain ε for monolayer MoS_2 containing a triangular hole with $(\bar{1}010)$ S edges. The change in potential energy for a pristine MoS_2 monolayer (dashed lines) is also shown for comparison. (b) and (c) Variation of the potential energy of the non-stoichiometric MoS_2 nanoribbon with uniaxial strain ε for three different ribbon widths W. In (b), the nanoribbon is terminated with $(\bar{1}010)$ S edge (top) and $(10\bar{1}0)$ Mo edge with S-monomers (bottom). In (c), the nanoribbon is terminated with $(\bar{1}010)$ S edge (top) and $(10\bar{1}0)$ Mo edge with S-dimers (bottom). In all cases, the dotted lines in the atomic models indicate the periodic supercell.

TABLE II. Edge stress τ for high-symmetry edges of monolayer MoS_2.

Edge stress τ (eV/Å)			
Zigzag $(\bar{1}010)$ S edge	Zigzag $(10\bar{1}0)$ Mo edge with S-monomers	Zigzag $(10\bar{1}0)$ Mo edge with S-dimers	Armchair stoichiometric $(11\bar{2}0)$ edge
0.25 ± 0.005	2.35 ± 0.005	0.65 ± 0.005	0.29 ± 0.017

Among the three edges of interest, the $(\bar{1}010)$ S edge offers an ideal choice for the triangular hole computation as the edge S atoms are in near perfect registry with the bulk lattice, resulting in very small deformation of Mo-S bonds along the edge as well as at the corner. Figure 3(a) shows a periodic MoS_2 supercell with a triangular hole with $(\bar{1}010)$ S edges as well as the variation of the potential energy with the biaxial strain ε for three different hole sizes. From Eq. (2), the edge stress for the $(\bar{1}010)$ S edge is obtained to be 0.25 eV/Å. Figures 3(b) and 3(c) show the atomic model as well as the variation of the potential energy with uniaxial strain for nanoribbons with $(\bar{1}010)$ S edge and S monomer/dimer-terminated $(10\bar{1}0)$ Mo edges. The average edge stresses for the nanoribbon models in Figs. 3(b) and 3(c) are 1.30 eV/Å and 0.45 eV/Å, respectively. The edge stresses for the individual edges are listed in Table II. For all three edges, we find that the edge stress is tensile. It is also evident that the magnitude of the edge stress is directly related to the deformation of Mo-S bonds at the edge—the $(10\bar{1}0)$ Mo edge with S-monomer reconstruction has a relatively large edge stress of 2.35 eV/Å. The large tensile edge stress for the $(10\bar{1}0)$ Mo edge with S-monomers is comparable to graphene armchair edges reconstructed with pentagon and heptagon pairs (2.44 eV/Å).[16] It is known that compressive edge stresses can lead to spontaneous twisting or warping of edges,[12,14,33] which decays with distance away from the edge. On the other hand, edges with tensile edge stresses can lead to large-scale curling of the 2D sheet.[34] Based on our computations, MoS_2 monolayers are likely to display the latter behavior, especially with exposed S-monomer terminated $(10\bar{1}0)$ Mo edges. For the sake of completeness, using the nanoribbon model, we have also computed the edge stress for stoichiometric armchair $(11\bar{2}0)$ MoS_2 edge (listed in Table II), which is nearly the same as the zigzag S-edge.

In conclusion, we have presented a facile approach for accurately and unambiguously determining the edge elastic properties for non-stoichiometric edges of 2D monolayers using a combination of DFT and continuum elasticity models. Based on this approach, we have computed the edge stresses for $(10\bar{1}0)$ and $(\bar{1}010)$ zigzag edges of hexagonal BN and MoS_2 monolayers. Our results show that the edge stresses for individual non-stoichiometric edges can differ significantly from the average values typically reported in the literature. The approach presented here is quite general and can be employed to determine edge stresses for non-stoichiometric edges of several other 2D or quasi-2D compound monolayers, e.g., transition metal oxides (MoO_3, WO_3, V_2O_5) and transition metal dichalcogenides (WS_2, $MoSe_2$, $MoTe_2$). Furthermore, with elementary modifications to the shape of the hole and Eq. (2), our approach can also be extended to crystal lattices with any general in-plane symmetry, where edges with orientation θ and $\theta + 180°$ are non-identical.

J.D. and N.M. gratefully acknowledge computational support fom Monash University Sun Grid and the National Computing Infrastructure funded by the Australian Government. I.F. and A.R. acknowledge startup support from the University of Massachusetts Amherst.

[1] K. S. Novoselov, A. K. Geim, S. V. Morozov, D. Jiang, Y. Zhang, S. V. Dubonos, I. V. Grigorieva, and A. A. Firsov, Science **306**, 666 (2004).
[2] M. Corso, W. Auwarter, M. Muntwiler, A. Tamai, T. Greber, and J. Osterwalder, Science **303**, 217 (2004).
[3] C. Jin, F. Lin, K. Suenaga, and S. Iijima, Phys. Rev. Lett. **102**, 195505 (2009).
[4] K. S. Novoselov, D. Jiang, F. Schedin, T. J. Booth, V. V. Khotkevich, S. V. Morozov, and A. K. Geim, Proc. Natl. Acad. Sci. U.S.A. **102**, 10451 (2005).
[5] J. N. Coleman, M. Lotya, A. O'Neill, S. D. Bergin, P. J. King, U. Khan, K. Young, A. Gaucher, S. De, R. J. Smith *et al.*, Science **331**, 568 (2011).
[6] M. V. Bollinger, J. V. Lauritsen, K. W. Jacobsen, J. K. Nørskov, S. Helveg, and F. Besenbacher, Phys. Rev. Lett. **87**, 196803 (2001).
[7] D. A. Areshkin, D. Gunlycke, and C. T. White, Nano Lett. **7**, 204 (2007).
[8] A. H. Castro Neto, F. Guinea, N. M. R. Peres, K. S. Novoselov, and A. K. Geim, Rev. Mod. Phys. **81**, 109 (2009).
[9] J. C. Meyer, A. K. Geim, M. I. Katsnelson, K. S. Novoselov, T. J. Booth, and S. Roth, Nature (London) **446**, 60 (2007).
[10] M. H. Gass, U. Bangert, A. L. Bleloch, P. Wang, R. R. Nair, and A. K. Geim, Nat. Nanotechnol. **3**, 676 (2008).
[11] J. Y. Huang, F. Ding, B. I. Yakobson, P. Lu, L. Qi, and J. Li, Proc. Natl. Acad. Sci. U.S.A. **106**, 10103 (2009).
[12] V. B. Shenoy, C. D. Reddy, A. Ramasubramaniam, and Y. W. Zhang, Phys. Rev. Lett. **101**, 245501 (2008).
[13] S. Jun, Phys. Rev. B **78**, 073405 (2008).
[14] K. V. Bets and B. I. Yakobson, Nano Res. **2**, 161 (2009).
[15] B. Huang, M. Liu, N. H. Su, J. Wu, W. H. Duan, B. L. Gu, and F. Liu, Phys. Rev. Lett. **102**, 166404 (2009).
[16] C. D. Reddy, A. Ramasubramaniam, V. B. Shenoy, and Y. W. Zhang, Appl. Phys. Lett. **94**, 101904 (2009).
[17] More precisely, Eq. (1) only yields combined values of the edge stresses $\tau_1 + \tau_2$ and edge moduli $E_{e1} + E_{e1}$.
[18] S. Jun, X. B. Li, F. C. Meng, and C. V. Ciobanu, Phys. Rev. B **83**, 153407 (2011).
[19] Y. Y. Liu, S. Bhowmick, and B. I. Yakobson, Nano Lett. **11**, 3113 (2011).
[20] B. Huang, H. Lee, B. L. Gu, F. Liu, and W. H. Duan, Nano Res. **5**, 62 (2012).
[21] S. B. Zhang and S. H. Wei, Phys. Rev. Lett. **92**, 086102 (2004).
[22] G. Kresse and J. Furthmuller, Phys. Rev. B **54**, 11169 (1996).
[23] J. P. Perdew, K. Burke, and M. Ernzerhof, Phys. Rev. Lett. **77**, 3865 (1996).
[24] G. Kresse and D. Joubert, Phys. Rev. B **59**, 1758 (1999).
[25] P. E. Blöchl, Phys. Rev. B **50**, 17953 (1994).
[26] V. Barone and J. E. Peralta, Nano Lett. **8**, 2210 (2008).
[27] With non-spin-polarized calculations, we obtained an average edge stress of 0.29 eV/Å, in good agreement with Ref. 18.
[28] L. S. Byskov, J. K. Norskov, B. S. Clausen, and H. Topsoe, J. Catal. **187**, 109 (1999).
[29] P. Raybaud, J. Hafner, G. Kresse, S. Kasztelan, and H. Toulhoat, J. Catal. **189**, 129 (2000).
[30] M. V. Bollinger, K. W. Jacobsen, and J. K. Nørskov, Phys. Rev. B **67**, 085410 (2003).
[31] T. Böker, R. Severin, A. Müller, C. Janowitz, R. Manzke, D. Voß, P. Krüger, A. Mazur, and J. Pollmann, Phys. Rev. B **64**, 235305 (2001).
[32] A. Ramasubramaniam, D. Naveh, and E. Towe, Phys. Rev. B **84**, 205325 (2011).
[33] A. Ramasubramaniam, P. Koskinen, O. O. Kit, and V. B. Shenoy, J. Appl. Phys. **111**, 054302 (2012).
[34] V. B. Shenoy, C. D. Reddy, and Y. W. Zhang, ACS Nano **4**, 4840 (2010).

APPENDIX B

ELASTIC PROPERTIES OF GRAPHENE NANOMESHES

APPLIED PHYSICS LETTERS **104**, 141911 (2014)

Elastic properties of graphene nanomeshes

Corinne Carpenter,[1] Augusto M. Christmann,[2] Lin Hu,[1] Ioanna Fampiou,[3] Andre R. Muniz,[2]
Ashwin Ramasubramaniam,[3] and Dimitrios Maroudas[1,a)]
[1]*Department of Chemical Engineering, University of Massachusetts, Amherst, Massachusetts 01003, USA*
[2]*Department of Chemical Engineering, Universidade Federal do Rio Grande do Sul, Rua Luiz Englert s/n, 90040-040 Porto Alegre, RS, Brazil*
[3]*Department of Mechanical and Industrial Engineering, University of Massachusetts, Amherst, Massachusetts 01003, USA*

(Received 11 March 2014; accepted 2 April 2014; published online 9 April 2014)

We study the elastic response of graphene nanomeshes based on molecular-statics and molecular-dynamics simulations of uniaxial tensile deformation tests. Elastic properties are determined as a function of the nanomesh architecture, namely, the lattice arrangement of the pores, pore morphology, material density (ρ), and pore edge passivation, and scaling laws for the density dependence of the elastic modulus M, $M(\rho)$, are established. We find that, for circular unpassivated pores, M scales with the square of ρ. Deviations from quadratic scaling are most strongly influenced by pore morphology and, to a lesser extent, by pore edge passivation and temperature. © *2014 AIP Publishing LLC*. [http://dx.doi.org/10.1063/1.4871304]

Graphene nanomeshes (GNMs) are graphene nanostructures consisting of a periodic arrangement of nano-scale holes or pores in the graphene lattice with neck widths less than 10 nm, mimicking dense arrays of ordered nanoribbons, which can open a band gap in graphene's electronic band structure making it semiconducting.[1] Such GNMs are typically prepared using block copolymer lithography and have been used in the fabrication of field-effect transistors with exceptional functionality.[1] Theoretical studies have explored the relationship between GNM structure and electronic properties,[2–4] including the opening of a band gap in the electronic band structure and the dependence of this gap on the GNM porosity and pore lattice symmetry.[5–7] Establishing rigorous structure-property-function relationships in such patterned graphene nanostructures is of utmost importance for their optimal design toward enabling a broad range of technological applications.

GNMs also constitute a class of two-dimensional (2D) ordered porous materials, which, together with other graphene materials such as crumpled graphene and graphene foam, have attracted a lot of interest due to their potential for applications stemming from their high intrinsic surface area in conjunction with the inherent remarkable electronic, thermal, and mechanical properties of graphene.[8] Increasing porosity decreases the porous material's density potentially causing dramatic deterioration of its mechanical properties, which emphasizes the importance of elastic modulus-density relations for materials design purposes. In natural porous or cellular materials, such as bone, the elastic modulus M scales with the square of the density ρ, $M \sim \rho^2$. However, nanostructured materials, such as ordered nanoporous silicas[9] fabricated to function as low-dielectric-constant insulators in microelectronic devices,[10] are less sensitive to porosity, exhibiting modulus-density scaling relations that are not as steep as those of natural cellular solids, with scaling exponents $p < 2$.[9,11] The influence on the mechanical properties of graphene of point defects, such as vacancies and Stone-Wales defects[12] as well as high vacancy concentrations due to irradiation,[13] have been studied using atomic-scale simulations. Nevertheless, in spite of their fundamental and technological importance, the mechanical properties of GNMs and their dependence on the GNM architectural parameters have not been studied systematically.

The purpose of this Letter is to establish relations for the elastic properties of GNMs as a function of the various parameters that fully define the nanomesh architecture, as well as of thermal and loading conditions. Toward this end, we conduct a systematic and comprehensive study of the elastic response of GNMs to uniaxial tensile straining based on atomistic simulations according to reliable many-body interatomic potentials. We derive scaling laws for the dependence of the GNM's elastic modulus on its density for various nanomesh architectures characterized by different pore lattice arrangements and pore sizes and determine the effects of pore morphology, pore edge passivation, and temperature on such modulus-density relations.

We constructed GNMs by introducing circular or elliptical pores in regular periodic arrangements (pore lattices) in single-layer graphene, as depicted in Fig. 1. Hexagonal (HEX), square (SQR), and honeycomb (HON) pore lattices were examined in this study. The center-to-center distance between neighboring pores was fixed at 24 C-C bond lengths. Both circular and elliptical pore morphologies were considered; elliptical pores were examined to study anisotropy effects for different loading directions. In GNMs with circular pores, the pore size was controlled by setting the pore radius. In GNMs with elliptical pores of semi-major and semi-minor (principal) axes a and b, respectively, the pore size was controlled by setting b and the aspect ratio $f \equiv a/b$. Controlling both the pore size and the pore center-to-center distance effectively controls the GNM density, ρ, and the GNM neck size (width), w. For all the GNM structures and morphologies examined, both unpassivated (dangling C bonds) and passivated (hydrogenated) pore edges were considered.

[a)] Author to whom correspondence should be addressed. Electronic mail: maroudas@ecs.umass.edu

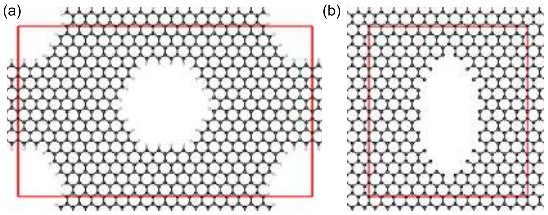

FIG. 1. Schematic representation of GNM architectures with (a) hydrogenated circular pores arranged in a hexagonal lattice and (b) unpassivated elliptical pores arranged in a square lattice in single-layer graphene. The red box denotes the nanomesh supercell.

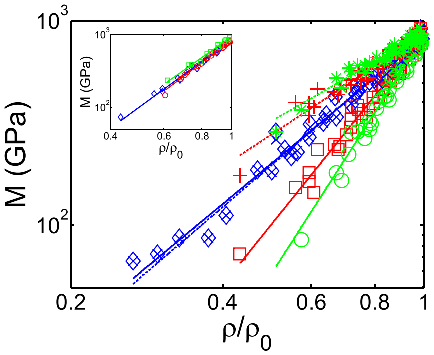

FIG. 2. Data for the dependence of the elastic modulus M on the scaled density ρ/ρ_0 derived from MS simulations of uniaxial tensile straining tests on GNMs with unpassivated pores. Data sets are organized according to the pore morphology, expressed by the pore aspect ratio f, and the straining direction (x or y). Open diamonds, squares, and circles represent the elastic response of GNMs consisting of pores with $f = 1$, 3/2, and 2, respectively, to straining along x, with ×-marks, crosses, and stars representing the elastic response of GNMs consisting of pores with $f = 1$, 3/2, and 2, respectively, to straining along y. The inset in the plot depicts the effect of the pore morphology on the $M(\rho/\rho_0)$ dependence for straining along x of GNMs consisting of pores with $f = 3/2$: open diamonds, circles, and squares represent the elastic response of GNMs with pores arranged in hexagonal, honeycomb, and square lattices, respectively. For each data set, the corresponding straight line in the log-log plot represents the optimal fit to the data based on nonlinear regression.

The generated GNMs were subjected to mechanical testing, namely, uniaxial tensile straining at constant temperature, which was simulated by employing molecular-statics (MS) and molecular-dynamics (MD) simulations, i.e., at $T = 0$ K and at non-zero temperatures, respectively. Both MS and MD simulations were performed using the LAMMPS software package.[14] In the simulations, interatomic interactions in GNMs were described according to the Adaptive Interatomic Reactive Empirical Bond-Order (AIREBO) potential.[15] In the MS simulations, strain increments of 0.01% were applied along the zigzag (henceforth denoted as x) and armchair (henceforth denoted as y) directions of the graphene lattice up to a maximum strain of 0.5% with full atomic relaxation performed at each strain level. It should be mentioned that for GNMs with elliptical pore morphologies, the major and minor axes of the pores are directed along y and x, respectively. These MS computations were carried out throughout the range of GNM architectural parameters (pore lattice, pore size, pore aspect ratio f, and pore passivation). At each point in parameter space, the GNM elastic modulus, M, was determined by a quadratic fit to the computed data for the potential energy, E, as a function of strain, ε, $E = M\varepsilon^2/2$, for each loading direction. MD simulations were used to compute M as a function of the GNM architectural parameters at non-zero temperatures; results at $T = 300$ K are reported here. The initial configurations for the MD simulations were GNMs fully relaxed at 0 K according to conjugate-gradient energy minimization with respect to the atomic coordinates; these configurations were then relaxed at $T = 300$ K and zero pressure employing the Berendsen thermostat and barostat.[16] Subsequently, each configuration was strained along either the x- or the y-direction up to a strain level of 1% using a time step of 0.5 fs and a strain rate of 1×10^{-4} ps^{-1}. As in the MS simulations, the supercell edge length in the directions normal to the applied strain was kept constant during the MD simulations. The modulus M was obtained from the slope of the resulting stress-strain curve in the low-strain limit, with atomic-level stresses computed according to the Virial theorem. Various supercell sizes were used for the MD simulations to confirm that the results are converged with respect to the supercell size.

Figure 2 shows the results of our MS simulations for the dependence of the elastic modulus M on the density ρ for GNMs with unpassivated pores under uniaxial straining. The results are given in a log-log plot, where M is plotted as a function of ρ/ρ_0 with ρ_0 being the normal density of perfect, pristine single-layer graphene. The various computed data sets shown in Fig. 2 are organized according to the pore morphology, given by f, and the straining direction, x or y. For each data set, the corresponding straight line in the log-log plot represents the optimal fit to the data. The excellent fits imply that the modulus-density relations of the GNMs obey the scaling law $M/M_0 = (\rho/\rho_0)^p$, with M_0 being the modulus of pristine graphene along the relevant direction of straining. For circular pores, $f = 1$, the elastic response of the GNM is isotropic, $M_x = M_y = M$, where the subscripts indicate the principal directions of straining, and the corresponding two data sets (open diamonds and ×-marks) practically overlap. However, for elliptical pores, $f > 1$, the elastic response of the GNM is anisotropic and the corresponding moduli (open squares and crosses for straining along x and y, respectively, at $f = 3/2$ and open circles and stars for straining along x and y, respectively, at $f = 2$) obey distinct scaling laws, $M_x \sim (\rho/\rho_0)^{p_x}$ and $M_y \sim (\rho/\rho_0)^{p_y}$, with scaling exponents $p_x \neq p_y$.

The results from the detailed statistical analysis of the data are listed in Table I focusing on the scaling exponents p_x and p_y for all pore morphologies, f, examined. The results of Table I also distinguish among the various pore lattice arrangements and indicate that the $M(\rho)$ relations (scaling laws) have a very weak (if any) dependence on the pore lattice structure. This also is evident from the results of Fig. 2, where a distinction among data sets with respect to the pore lattice arrangement in the GNMs has not been made. The extremely weak effect of the GNM's pore lattice structure on its $M(\rho)$ relation also is highlighted in the inset in Fig. 2 for straining along x at $f = 3/2$; the three data sets in the inset for GNMs with hexagonal, square, and honeycomb pore lattices and the corresponding straight lines from the fitting of these data sets practically overlap, confirming that the scaling exponent in the $M(\rho)$ relation is practically (within statistical

TABLE I. Values of scaling exponents p_x and p_y calculated from statistical analysis (nonlinear regression) of the computed data for the GNM elastic modulus dependence on density based on MS simulations and MD simulations at $T = 300$ K of uniaxial straining of GNMs along x and y, respectively. Results are presented from data analysis for different elliptical pore morphologies, expressed by the aspect ratio f, pore edge passivation, and various pore lattice arrangements, namely, HEX, SQR, and HON, as well as from analysis of all the data for the various pore lattice arrangements combined (ALL). N denotes the number of points in each data set analyzed.

	N	p_x	p_y	N	p_x	p_y	N	p_x	p_y
		Unpassivated pores, $f = 1, T = 0$ K			Unpassivated pores, $f = 3/2, T = 0$ K			Unpassivated pores, $f = 2, T = 0$ K	
ALL	45	2.04 ± 0.13	2.11 ± 0.13	50	3.07 ± 0.21	1.63 ± 0.13	43	3.84 ± 0.28	1.42 ± 0.14
HEX	23	2.08 ± 0.12	2.12 ± 0.12	18	3.05 ± 0.21	1.60 ± 0.17	17	3.82 ± 0.33	1.44 ± 0.17
HON	10	2.07 ± 0.19	2.16 ± 0.11	19	3.14 ± 0.17	1.64 ± 0.13	16	3.96 ± 0.33	1.40 ± 0.28
SQR	12	1.95 ± 0.27	2.04 ± 0.23	13	2.93 ± 0.32	1.65 ± 0.21	10	4.23 ± 0.53	1.66 ± 0.26
		H-passivated pores, $f = 1, T = 0$ K			H-passivated pores, $f = 3/2, T = 0$ K			H-passivated pores, $f = 2, T = 0$ K	
ALL	41	1.78 ± 0.11	1.86 ± 0.11	50	2.71 ± 0.21	1.45 ± 0.13	43	3.39 ± 0.27	1.27 ± 0.14
HEX	22	1.78 ± 0.06	1.81 ± 0.04	18	2.60 ± 0.19	1.29 ± 0.14	17	3.44 ± 0.27	1.23 ± 0.16
HON	9	2.06 ± 0.09	2.13 ± 0.11	19	2.91 ± 0.20	1.57 ± 0.13	16	3.70 ± 0.33	1.37 ± 0.27
SQR	10	1.82 ± 0.26	1.90 ± 0.19	13	2.55 ± 0.28	1.65 ± 0.14	10	3.52 ± 0.41	1.25 ± 0.42
		Unpassivated pores, $f = 1, T = 300$ K						Unpassivated pores, $f = 2, T = 300$ K	
HEX	8	2.40 ± 0.14	2.42 ± 0.12				12	3.71 ± 0.41	1.71 ± 0.16

error) independent of the GNM's pore lattice arrangement. Finally, we mention that the scaling exponents reported in Table I are statistical outcomes based on optimal fitting of the data according to nonlinear regression, as opposed to linear regression of the logarithms of the data, $\log M$ vs. $\log \rho$. In any case, the differences for p_x and p_y between the reported values and those derived from linear regression are systematic but very minor (within 5% of the reported scaling exponents).

Our results for GNMs with circular unpassivated pores, Fig. 2 and Table I, indicate that within statistical error, at $f = 1$, $p_x = p_y \approx 2$, i.e., $M \sim \rho^2$. This result is consistent with the elastic response of other cellular materials,[17–20] including graphene elastomers.[18] Interestingly, we also find that at moderate to high densities ($\rho/\rho_0 > 0.5$) the $M(\rho)$ scaling for circular pores is nearly optimal, closely following the Hashin-Shtrikman upper bound $M/M_0 \leq (\rho/\rho_0)/[3 - 2(\rho/\rho_0)]$.[21,22] However, the $M(\rho)$ relation for GNMs with $f > 1$ deviates strongly from this classical cellular response. Specifically, we find (Fig. 2 and Table I) that, within statistical errors less than 10% of the scaling exponent, at $f = 3/2$, $p_x \approx 3$, and $p_y \approx 5/3$; and at $f = 2$, $p_x \approx 4$, and $p_y \approx 3/2$. Generalizing these scaling laws gives $p_x \approx 2f$ and $p_y \approx (f+1)/f$, i.e., $M_x \sim \rho^{2f}$ and $M_y \sim \rho^{(f+1)/f}$ for the anisotropic elastic response of GNMs with unpassivated pores of elliptical morphology with aspect ratio f. Detailed theoretical analysis to fundamentally derive the above scaling laws is beyond the scope of the present study and will be pursued in a forthcoming publication. We only mention that as the value of f increases, effects of stress concentration at the tips of the elongated pores introduce additional complexity to the scaling analysis.

The effects of pore edge passivation on the $M(\rho)$ relations of GNMs are examined in Fig. 3, which shows results of MS simulations for the elastic response of GNMs with H-passivated pores in terms of modulus-density relations. The results are presented and organized in exactly the same manner as those for GNMs with unpassivated pores in Fig. 2. It is evident from the results of Fig. 3 that the elastic response in this class of GNMs also obeys the scaling laws $M_x \sim \rho^{p_x}$ and $M_y \sim \rho^{p_y}$, and the outcomes of the detailed statistical

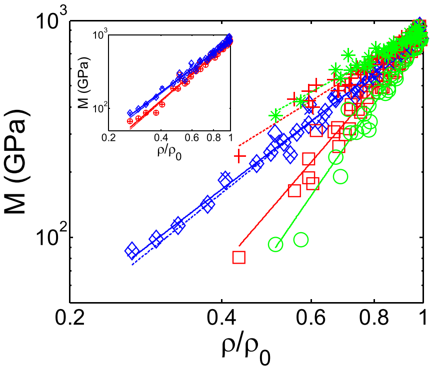

FIG. 3. Data for the dependence of the elastic modulus M on the scaled density ρ/ρ_0 derived from MS simulations of uniaxial tensile straining tests on GNMs with H-passivated pores. Data sets are organized according to the pore morphology, expressed by the pore aspect ratio f, and the straining direction (x or y). Open diamonds, squares, and circles represent the elastic response of GNMs consisting of pores with $f = 1$, 3/2, and 2, respectively, to straining along x, with ×-marks, crosses, and stars representing the elastic response of GNMs consisting of pores with $f = 1$, 3/2, and 2, respectively, to straining along y. For each data set, the corresponding straight line in the log-log plot represents the optimal fit to the data based on nonlinear regression. The inset in the plot depicts the effect of the pore edge passivation on the $M(\rho/\rho_0)$ dependence for straining along x and y of GNMs consisting of circular pores, $f = 1$: open circles and crosses represent the elastic response of GNMs with unpassivated pores to straining along x and y, respectively, with open diamonds and ×-marks representing the elastic response of GNMs with H-passivated pore edges to straining along x and y, respectively. Solid and dashed straight lines in the log-log plot represent optimal fits based on nonlinear regression to the data associated with straining along x and y, respectively.

analysis of the computed data also are included in Table I. Moreover, the results of Fig. 3 and Table I show that the effect of pore lattice arrangement on the $M(\rho)$ relations remains very weak in spite of the pore passivation. Comparing the results of Fig. 3 with those of Fig. 2 shows that M_x and M_y increase as a result of H passivation with respect to the corresponding elastic moduli of GNMs with unpassivated pore edges. This elastic modulus strengthening due to H passivation is shown most clearly in the inset in Fig. 3, where the data sets for GNMs with passivated and unpassivated circular pore edges are compared directly. This modulus strengthening due to pore edge passivation also is seen clearly through the lowering of the corresponding scaling exponents with respect to those for GNMs with unpassivated pores. In the isotropic case, $f = 1$, $p_x \approx p_y \approx 1.8 < 2$, which is the scaling exponent for GNMs with circular unpassivated pores. This lowering of the scaling exponent below 2 indicates that, as a result of GNM pore passivation, the elastic moduli become less sensitive to porosity than those of classical cellular materials. In the anisotropic cases examined, at $f = 3/2$, $p_x \approx 2.7 < 3$, and $p_y \approx 1.45 < 5/3$; and at $f = 2$, $p_x \approx 3.4 < 4$, and $p_y \approx 1.3 < 3/2$. In general, pore edge passivation strengthens the GNMs' elastic moduli and makes them less sensitive to porosity compared to those of GNMs with unpassivated pores.

Finally, the effects of temperature on the $M(\rho)$ relations of GNMs with $f = 1$ and $f = 2$ are examined in Fig. 4, which shows results of MD simulations for the elastic response of GNMs with unpassivated pores at $T = 300$ K. It is evident from the results of Fig. 4 that at non-zero temperature, the elastic response of GNMs continues to obey the scaling laws $M_x \sim \rho^{p_x}$ and $M_y \sim \rho^{p_y}$, and the outcomes of the statistical analysis of the smaller data sets in this case for the scaling exponents also are listed in Table I. As expected, raising the temperature softens the elastic moduli. At $f = 1$, for circular pores, the elastic response of the GNMs is isotropic (overlapping data sets in Fig. 4) with $M_x = M_y$ within the statistical error and $p_x = p_y \approx 2.4 > 2$, which indicates an increased sensitivity to porosity compared to that of classical cellular materials. For elliptical pores of $f = 2$, the elastic response of the GNMs remains anisotropic with $p_x \approx 3.7 < 4$ and $p_y \approx 1.7 > 3/2$, i.e., the scaling exponent p_x and p_y decreases and increases, respectively, with respect to their values in the static reference state ($T = 0$). Using the scaling exponent difference $p_x - p_y$ as a metric of the anisotropy in the GNM elastic response, it is evident that this elastic anisotropy weakens with increasing temperature.

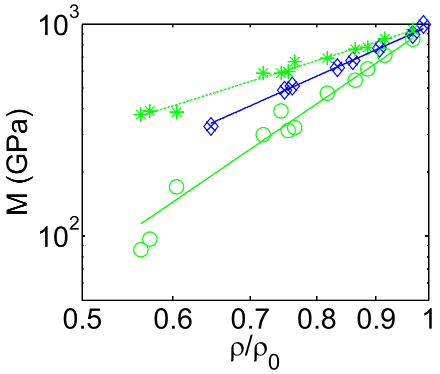

FIG. 4. Data for the dependence of the elastic modulus M on the scaled density ρ/ρ_0 derived from MD simulations of uniaxial tensile straining tests on GNMs with unpassivated pores at $T = 300$ K. Data sets are organized according to the pore morphology, expressed by the pore aspect ratio f, and the straining direction (x or y). Open diamonds and circles represent the elastic response of GNMs consisting of pores with $f = 1$ and 2, respectively, to straining along x, with ×-marks and stars representing the elastic response of GNMs consisting of pores with $f = 1$ and 2, respectively, to straining along y.

In summary, we conducted a systematic study of the elastic response of graphene nanomeshes to uniaxial straining along the zigzag (x) and armchair (y) directions and determined the dependence of the nanomesh's elastic modulus M on the nanomesh density ρ, pore lattice structure, pore morphology, and pore edge passivation. We found that, for given density and pore morphology, the elastic moduli are practically independent of pore lattice arrangement and established $M(\rho)$ relations that obey the scaling laws $M_x \sim \rho^{p_x}$ and $M_y \sim \rho^{p_y}$. At zero temperature, for circular unpassivated pores, the elastic response is isotropic, $M_x = M_y$, with $p_x = p_y = 2$. For elliptical pores with aspect ratio $f > 1$, the elastic response of the nanomeshes becomes anisotropic, $M_x < M_y$, with scaling exponents $p_x \approx 2f$ and $p_y \approx (f+1)/f$. Passivating the nanomesh pore edges with H atoms strengthens their elastic moduli and lowers their sensitivity to porosity through lowering of the scaling exponents. With increasing temperature, the elastic moduli of nanomeshes with circular pores soften and become more sensitive to porosity and the anisotropic elastic response of nanomeshes with elliptical pores of $f > 1$ becomes more isotropic. Our results for the $M(\rho)$ relations emphasize the strong dependence of the GNMs' elastic moduli on the GNMs' neck sizes and highlight the role of pore edge passivation and the need for neck size control to guarantee the structural integrity of the nanomeshes. Our findings also provide experimentally testable hypotheses for the mechanical behavior of GNMs, as an important class of patterned nanoporous 2D functional materials.

This work was supported by the National Science Foundation through the University of Massachusetts, Amherst Materials Research Science and Engineering Center (MRSEC) on Polymers under Award No. DMR-0820506. A.R.M. and A.M.C. acknowledge CESUP/UFRGS for using their computing facility.

[1] J. Bai, X. Zhong, S. Jiang, Y. Huang, and X. Duan, Nat. Nanotechnol. **5**, 190 (2010).
[2] T. G. Pedersen, C. Flindt, J. Pedersen, N. A. Mortensen, A.-P. Jauho, and K. Pedersen, Phys. Rev. Lett. **100**, 136804 (2008).
[3] H. Sahin and S. Ciraci, Phys. Rev. B **84**, 035452 (2011).
[4] J. Lee, A. K. Roy, J. L. Wohlwend, V. Varshney, J. B. Ferguson, W. C. Mitchel, and B. L. Farmer, Appl. Phys. Lett. **102**, 203107 (2013).
[5] R. Martinazzo, S. Casolo, and G. F. Tantardini, Phys. Rev. B **81**, 245420 (2010).
[6] R. Petersen, T. G. Pedersen, and A.-P. Jauho, ACS Nano **5**, 523 (2011).
[7] F. Ouyang, S. Peng, Z. Liu, and Z. Liu, ACS Nano **5**, 4023 (2011).
[8] L. Jiang and Z. Fan, Nanoscale **6**, 1922 (2014).
[9] H. Fan, C. Hartshorn, T. Buchheit, D. Tallant, R. Assink, R. Simpson, D. J. Kissel, D. J. Lacks, S. Torquato, and C. J. Brinker, Nature Mater. **6**, 418 (2007).
[10] R. A. Pai, R. Humayun, M. T. Schulberg, A. Sengupta, J.-N. Sun, and J. J. Watkins, Science **303**, 507 (2004).

[11] M. R. Gungor, J. J. Watkins, and D. Maroudas, Appl. Phys. Lett. **92**, 251903 (2008); **98**, 121902 (2011).

[12] N. Jing, Q. Xue, C. Ling, M. Shan, T. Zhang, X. Zhou, and Z. Jiao, RSC Adv. **2**, 9124 (2012).

[13] C. Carpenter, A. Ramasubramaniam, and D. Maroudas, Appl. Phys. Lett. **100**, 203105 (2012); C. Carpenter, D. Maroudas, and A. Ramasubramaniam, Appl. Phys. Lett. **103**, 013102 (2013).

[14] S. Plimpton, J. Comput. Phys. **117**, 1 (1995).

[15] S. J. Stuart, A. B. Tutein, and J. A. Harrison, J. Chem. Phys. **112**, 6472 (2000).

[16] H. J. C. Berendsen, J. P. M. Postma, W. F. Van Gunsteren, A. DiNola, and J. R. Haak, J. Chem. Phys. **81**, 3684 (1984).

[17] K. C. Cheung and N. Gershenfeld, Science **341**, 1219 (2013).

[18] L. Qiu, J. Z. Liu, S. L. Chang, Y. Wu, and D. Li, Nat. Commun. **3**, 1241 (2012).

[19] L. J. Gibson and M. F. Ashby, Proc. R. Soc. London A **382**, 43 (1982); L. J. Gibson and M. F. Ashby, *Cellular Solids: Structure and Properties*, 2nd ed. (Cambridge University Press, Cambridge, 1997).

[20] V. S. Deshpande, M. F. Ashby, and N. A. Fleck, Acta Mater. **49**, 1035 (2001).

[21] Z. Hashin and S. Shtrikman, J. Mech. Phys. Solids **11**, 127 (1963).

[22] S. Torquato, L. V. Gibiansky, M. J. Silva, and L. J. Gibson, Int. J. Mech. Sci. **40**, 71 (1998).

APPENDIX C

DENSITY-FUNCTIONAL TIGHT-BINDING SIMULATIONS OF CURVATURE-CONTROLLED LAYER DECOUPLING AND BAND-GAP TUNING IN BILAYER MOS$_2$

PRL **112,** 186802 (2014) PHYSICAL REVIEW LETTERS week ending 9 MAY 2014

Density-Functional Tight-Binding Simulations of Curvature-Controlled Layer Decoupling and Band-Gap Tuning in Bilayer MoS_2

Pekka Koskinen,[1,*] Ioanna Fampiou,[2] and Ashwin Ramasubramaniam[2,†]
[1]*NanoScience Center, Department of Physics, University of Jyväskylä, 40014 Jyväskylä, Finland*
[2]*Department of Mechanical and Industrial Engineering, University of Massachusetts Amherst, Amherst, Massachusetts 01003, USA*

(Received 15 November 2013; published 8 May 2014)

Monolayer transition-metal dichalcogenides (TMDCs) display valley-selective circular dichroism due to the presence of time-reversal symmetry and the absence of inversion symmetry, making them promising candidates for valleytronics. In contrast, in bilayer TMDCs both symmetries are present and these desirable valley-selective properties are lost. Here, by using density-functional tight-binding electronic structure simulations and revised periodic boundary conditions, we show that bending of bilayer MoS_2 sheets breaks band degeneracies and localizes states on separate layers due to bending-induced strain gradients across the sheets. We propose a strategy for employing bending deformations in bilayer TMDCs as a simple yet effective means of dynamically and reversibly tuning their band gaps while simultaneously tuning valley-selective physics.

DOI: 10.1103/PhysRevLett.112.186802 PACS numbers: 73.22.-f

Transition-metal dichalcogenides (TMDCs)—notably, the Group-VI dichalcogenides—have been the subject of much recent interest for nanoscale electronics and photonics [1–5]. Single- and few-layer MX_2 ($M =$ Mo, W; $X =$ S, Se, Te) compounds, unlike graphene, display appreciable electronic band gaps [4–7], making them promising candidates for nanoscale digital electronics [8,9]. Upon thinning multilayer sheets to monolayer thickness, TMDCs undergo an indirect-to-direct gap transition leading to strong and stable photoluminescence, which is attractive for optoelectronic applications [4,6,7,10]. In addition, recent experiments and simulations have shown that the electronic and optical properties of few-layer TMDCs can be controllably modified by external fields [11,12] and mechanical strains [13–18]. The combination of chemical composition, dimensionality, and external perturbations thus provides a rich space of parameters for designing optimized TMDC nanostructures for device applications.

TMDCs also allow for more complex manipulation of their electronic properties. The band edges of monolayer Group-VI TMDCs lie at the corners of their hexagonal Brillouin zones, conventionally called K and K' points, or valleys. Since the monolayer lacks inversion symmetry, the K and K' valleys are related only by time-reversal symmetry, which, in conjunction with spin-orbit splitting of the band edges, associates a distinct magnetic moment with each valley [19]. This property enables selective excitation of each valley by circularly polarized light, as demonstrated on MoS_2 [20–22] and WSe_2 [23] monolayers. In contrast, bilayer TMDCs lose this valley-selective circular dichroism because of the presence of both inversion and time-reversal symmetries. As these symmetries are retained under homogeneous mechanical strains, such strains cannot be used to break the valley degeneracy. This is unfortunate since strain has been shown to alter the band gap by as much as ~ 120 meV/% strain in bilayer MoS_2 [14]. Finding a way to break valley degeneracy in strained bilayers would be desirable, as it would enable reversible and simultaneous control over the optical band gap and valley-selective phenomena.

Fortunately, there are options for breaking inversion symmetry in bilayer TMDCs. The first trick is to apply a perpendicular electric field; this enables external control over the valley magnetic moment [24,25], while giving the charge carriers an additional degree of freedom, a pseudospin, corresponding to separate layers in the sheet [25–27]. While calculations suggest that the external field can also tune the band gap [11], experimental realization might be difficult as the required fields are rather large. Mechanical strains, however, need only be modest to induce appreciable band-gap tuning. Hence, in this Letter we introduce a second trick, breaking the symmetry by inhomogeneous strains due to uniform bending. From elementary Euler-Bernoulli kinematics, bending imposes a linear variation in strain normal to the layers [28]. Should interlayer coupling be absent, each layer would then be an independent monolayer whose band gap would correlate directly with the strain in that layer. In this ideal picture, the K and K' valleys of each layer could be independently excited with photons of specific energy and helicity.

Could this idealized scenario be realized in layered materials such as MoS_2 with weak but certainly nonzero interlayer coupling? We address this question in detail via density-functional tight-binding simulations that employ revised periodic boundary conditions to model the presence of curvature in bilayer MoS_2. We show that curvature can induce complete decoupling of layers around $K(L')$ and $K'(L)$ points, meaning that bands localize on separate layers and their energy shifts are governed by layer-specific strains. Each bent layer then effectively behaves as an independent monolayer, suggesting that distinct valleys in distinct layers could indeed be excited independently. These results suggest that curvature could provide a simple yet effective strategy for simultaneous control over band gaps and valley polarizations in few-layer TMDCs.

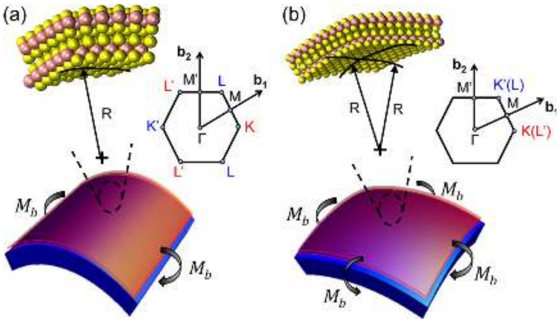

FIG. 1 (color online). Schematic of bilayer $\mathrm{MoS_2}$ (purple sheets) on a flexible substrate with (a) cylindrical and (b) spherical curvature, as induced by applied moments M_b. Insets show the corresponding Brillouin zones and high-symmetry points in reciprocal space. K and L', and K' and L valleys are equivalent, differing by a reciprocal lattice vector.

To model the electronic structure, we used the density-functional tight-binding (DFTB) method with an established set of Mo and S parameters [29,30]. The electronic structures of TMDCs are known to be computationally challenging due to their prominent spin-orbit and quasiparticle features [10,31], and thus they are difficult to model even with density-functional theory (DFT). However, it has been shown that the movement of band edges upon strain follows the same electromechanical trends, regardless of the level of theory, be it DFT or beyond [32]. Most important, these very same electromechanical trends are also reproduced by DFTB [30,33], and validated against DFT even for transport properties [34]. Therefore, DFTB suffices well for the purpose of our work, which is not dependent on high accuracy of numbers but on correct electromechanical trends. For completeness, however, we further validated the method by comparing it explicitly to DFT results for the strain-dependence of the true gap (indirect) and direct gap (at K and K') for bilayer $\mathrm{MoS_2}$ under equibiaxial strain (see Supplemental Material [35]).

Efficient simulation of the bending deformations themselves was enabled by revised periodic boundary conditions [36–39]. Conventionally, a flat sheet would be simulated by the minimal unit cell spanned by vectors $\mathbf{a}_1$ and $\mathbf{a}_2$ (in the xy plane), where $|\hat{a}_1 \times \hat{a}_2| = \sin(\pi/3)$ and lattice constant $a = |\mathbf{a}_i| = 3.16$ Å. Here, instead of creating periodic images by the usual translations along $\mathbf{a}_1$ and $\mathbf{a}_2$, rotations were also used. First, cylindrical deformation was modeled by taking one translation (by $\mathbf{a}_1$) and one rototranslation (translation by $\mathbf{a}_1 \cos(\pi/3)$ followed by rotation of an angle $\alpha = a \sin(\pi/3)/R$ around $\hat{a}_1$, where R is the radius of curvature). Second, spherical deformation was modeled by taking two distinct rotations with respect to axes $\hat{b}_1$ and $\hat{b}_2$ by an angle $\alpha = a/R$, where $\hat{b}_i \times \hat{z} = \hat{a}_i$ [40]. Apart from the symmetry operations, the simulations proceeded as for conventional periodic slabs. We note that in the limit of small curvature, a is small compared to R and the unit cell properties can thus be viewed as local properties. We therefore emphasize that a notion about an overall geometrical structure such as "cylinder" or "sphere" is irrelevant [41]. The deformations are illustrated in Fig. 1.

The curvature is quantified by the dimensionless parameter $\Theta = H/(2R)$, where $H = 6.2$ Å is the distance between Mo-Mo planes in the bilayer. This parameter is convenient because it equals the average tensile strain in the outer layer ($\varepsilon_{\mathrm{out}} = \Theta$) and the average compressive strain in the inner layer ($\varepsilon_{\mathrm{in}} = -\Theta$), independent of sheet thickness [42]. Finally, for each enforced Θ, the structures were optimized using 10×10 κ points and a maximum force criterion of 0.01 eV/Å [40].

Let us first consider the effect of bending on the electronic structure of bilayer $\mathrm{MoS_2}$. The first central result of this work is that bending not only alters the band gap but also breaks the band degeneracy as a result of broken layer symmetry [Fig. 2]. This is in sharp contrast to the homogeneous in-plane strains which, as noted earlier, can only change the band gap but cannot break the layer degeneracy [Fig. 2 (top row)]. The bending-induced changes can be understood by considering the orbital composition of the bands. States at the valence band (VB) maximum at Γ are dominated by Mo d_{z^2} and S p_z orbitals while those at the conduction band (CB) minimum at K/K' are mostly comprised of Mo d_{z^2} with some mixing of S p_x and p_y [11,43,44]. Stacking of $\mathrm{MoS_2}$ layers confines the diffuse, out-of-plane Mo d_{z^2} and S p_z states and increases their energy, causing the direct-to-indirect gap transition from monolayer to multilayer $\mathrm{MoS_2}$ [45]. It is precisely these Mo d_{z^2}-dominated regions near the Γ point of the VB and $K(L')/K'(L)$ points of the CB that yield the greatest sensitivity to strain-induced lifting of degeneracy upon bending (Fig. 2). On the other hand, due to primary composition of in-plane Mo $d_{x^2-y^2}$ and Mo d_{xy} orbitals together with a small mixture of S p_x and p_y orbitals [11,43,44], the VB maxima at $K(L')/K'(L)$ are more resilient against bending. Moreover, the effect of bending for given Θ is larger for spherical bending than for cylindrical bending, in agreement with analogous effects seen in equibiaxial versus uniaxial in-plane strains in monolayer $\mathrm{MoS_2}$ [16,46].

In addition to orbital composition, it is instructive to investigate the spatial natures of the states. As the second

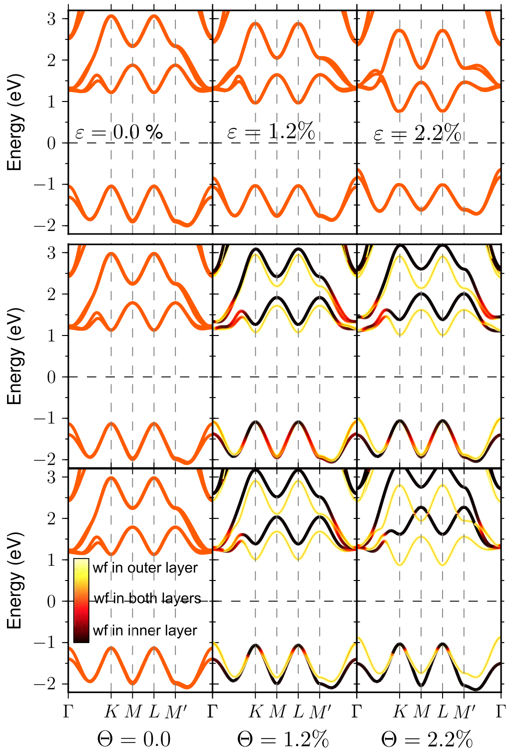

FIG. 2 (color online). Effect of stretching and bending on bilayer MoS_2 band structure. Flat bilayer under equibiaxial strains ε (top row), bilayer under cylindrical bending (middle row), and bilayer under spherical bending (bottom row) at values of Θ indicated at bottom. Bands are colored by the degree of wave function localization to outer or inner layers, as obtained from Mulliken population analysis.

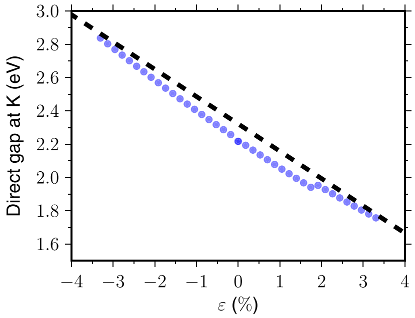

FIG. 3 (color online). Calculated layer-specific direct band gaps (filled symbols) at $K(L')/K'(L)$ as a function of equibiaxial strain within each layer of bilayer MoS_2 subjected to spherical bending. The outer and inner layers experience equibiaxial tensile and compressive strains of magnitude $\epsilon = \pm\Theta$, respectively, as noted in the text. The dashed line is the DFTB direct gap at K/K' of monolayer MoS_2 under equibiaxial strain (no curvature).

central result we find that, although initially states are delocalized across both layers, upon bending most of them localize on separate layers (Fig. 2 middle and bottom rows). The localization is particularly pronounced near the CB edge at $K(L')/K'(L)$ where also the strain-induced energy splittings are significant. Note that localization can still be observed near the VB edge at $K(L')/K'(L)$ regardless of negligible energy splitting. This means that it is now possible to define layer-specific direct band gaps [at $K(L')/K'(L)$] and layer-specific indirect band gaps (between the VB at Γ and CB at $K(L')/K'(L)$), both of which systematically decrease and increase with tensile and compressive layer-specific strains. The computed layer-specific direct gaps at $K(L')/K'(L)$ are displayed in Fig. 3; as seen, the gaps in each layer are in close quantitative agreement with the DFTB direct gap at the K/K' point of a monolayer under in-plane, equibiaxial strain. Thus, these results reveal that bending not only alters the fundamental band gap of the bilayer but also decouples the layers at the $K(L')/K'(L)$ valleys and consequently allows for tuning of the gaps of each layer simultaneously.

Based on the observed robustness of bending-induced decoupling, we now propose a strategy to control valley polarization in bent bilayer MoS_2 (Fig. 4). For monolayer MoS_2, it is well known that optical transitions at the K and K' valleys are governed by the selection rule $\Delta m_j = \pm 1$ and, as the rule is valid over a wide region of the surrounding reciprocal space, it also carries over to the band-edge (spin-orbit split) A and B excitons [21,22]. While in a monolayer spin and valley are coupled, in a bilayer they are decoupled due to inversion symmetry, and excitation by circularly polarized light can only control the net spin but not the valley population [21]. This lack of control will persist in bilayers under in-plane equibiaxial strain, where only the overall band gap changes [Figs. 4(a) and 4(b)]; this band-gap change is manifested experimentally as a shift in the absorption and photoluminescence peaks [13,14]. However, now that bending breaks inversion symmetry and decouples the layers, could valley-selective physics be realized in these decoupled monolayers? The answer depends on spin-orbit (SO) splitting of the band edges, which is absent in our implementation of DFTB. It is nevertheless possible to advance general arguments to address this issue by using previous works. First, for monolayer MoS_2, strain-induced changes in SO splitting of the VB edge at K/K' have been shown to be more than an order of magnitude smaller than changes in the band gaps [47]. Our own DFT studies corroborate this finding for both strained monolayers and bilayers (see Supplemental Material [35]). Second, previous DFT calculations by one of us [11] have shown electronic decoupling of layers in bilayer MoS_2 under an external electric field, with similar inversion-symmetry breaking. An examination of the SO splitting of the VB edge shows that with decreasing

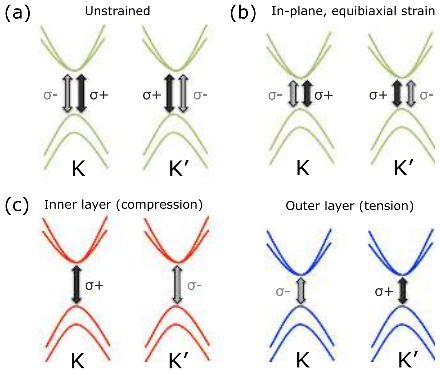

FIG. 4 (color online). Schematic of the proposal to control valley polarization in bilayer MoS_2. By optical selection rules, (a) in the absence of strain and (b) in the presence of in-plane, equibiaxial tensile strain, circularly polarized light ($\sigma-$ and $\sigma+$) populates both K and K' valleys. (c) Bending breaks the inversion symmetry and layer degeneracies; hence, time-reversal symmetry again couples spin and valley in each individual layer and circularly polarized light can be used to excite a given valley (by choosing the photon helicity σ) in a given layer (by choosing the photon energy). Spin-orbit splitting of the band edges has been indicated here as a perturbation to the strained band structure.

interlayer coupling (i.e., increasing electric field), the SO splitting of the VB edge for each layer at K/K' approaches that of a monolayer (see Supplemental Material [35]). We therefore infer, albeit indirectly, that SO splitting of the VB edge at $K(L')/K'(L)$ will likely persist under the combination of in-plane strains and layer decoupling as induced by bending, leading to the reappearance of valley polarization in each layer. Unlike the case of symmetry breaking by external electric fields where the states from each layer are nearly rigidly translated in opposite directions [11], the band edges of each layer in the bent bilayers move towards or away from each other depending upon the layer-specific strain. Thus, it should further be possible to address a specific layer and a specific valley by selecting both the helicity and the energy of the photon [Fig. 4(c)]. In practice, larger curvatures should induce larger energy differences between layer-specific transitions, thus allowing for the absorption peaks of circularly polarized light to become more pronounced and differentiable. Our proposal is complementary to the approach of Castellanos-Gomez *et al.* [48] where interlayer coupling in folded MoS_2 was reduced by stacking disorder that includes regions of orientational twist between adjacent MoS_2 layers. These twisted regions were shown to exhibit enhanced photoluminescence in conjunction with both neutral and charged excitons, characteristic of monolayer MoS_2 [49].

In summary, we have shown that bending-induced strain gradients can induce complete decoupling of layers around $K(L')$ and $K'(L)$ valleys in bilayer MoS_2, thus rendering individual sheets as electronically independent monolayers at these valleys with properties governed by layer-specific strains. We propose that this phenomenon could allow for selective pumping of individual K and K' valleys of specific layers by selecting the helicity and energy of the exciting laser. Because the electronic structures and electromechanics are similar across the entire family of Group-VI TMDCs, we expect our results and proposals on MoS_2 to be broadly applicable and realizable in other Mo and W dichalcogenides.

P. K. acknowledges the Academy of Finland for funding and the Finnish IT Center for Science (CSC) for computational resources. I. F. and A. R. acknowledge support from the National Science Foundation through the University of Massachusetts, Amherst Materials Research Science and Engineering Center (MRSEC) on Polymers under Award No. DMR-0820506.

---

[*] pekka.koskinen@iki.fi
[†] ashwin@engin.umass.edu

[1] K. S. Novoselov, D. Jiang, F. Schedin, T. J. Booth, V. V. Khotkevich, S. V. Morozov, and A. K. Geim, Proc. Natl. Acad. Sci. U.S.A. **102**, 10451 (2005).
[2] H. S. S. Ramakrishna Matte, A. Gomathi, A. K. Manna, D. J. Late, R. Datta, S. K. Pati, and C. N. R. Rao, Angew. Chem., Int. Ed. Engl. **49**, 4059 (2010).
[3] M. Chhowalla, H. Shin, G. Eda, L. Li, K. Loh, and H. Zhang, Nat. Chem. **5**, 263 (2013).
[4] Q. H. Wang, K. Kalantar-Zadeh, A. Kis, J. N. Coleman, and M. S. Strano, Nat. Nanotechnol. **7**, 699 (2012).
[5] A. K. Geim and I. V. Grigorieva, Nature (London) **499**, 419 (2013).
[6] K. F. Mak, C. Lee, J. Hone, J. Shan, and T. F. Heinz, Phys. Rev. Lett. **105**, 136805 (2010).
[7] A. Splendiani, L. Sun, Y. Zhang, T. Li, J. Kim, C. Chim, G. Galli, and F. Wang, Nano Lett. **10**, 1271 (2010).
[8] B. Radisavljevic, A. Radenovic, J. Brivio, V. Giacometti, and A. Kis, Nat. Nanotechnol. **6**, 147 (2011).
[9] B. Radisavljevic, M. B. Whitwick, and A. Kis, ACS Nano **5**, 9934 (2011).
[10] A. Ramasubramaniam, Phys. Rev. B **86**, 115409 (2012).
[11] A. Ramasubramaniam, D. Naveh, and E. Towe, Phys. Rev. B **84**, 205325 (2011).
[12] L. Kou, T. Frauenheim, and C. Chen, J. Phys. Chem. Lett. **4**, 1730 (2013).
[13] K. He, C. Poole, K. Mak, and J. Shan, Nano Lett. **13**, 2931 (2013).
[14] H. J. Conley, B. Wang, J. I. Ziegler, R. F. Haglund, Jr., S. T. Pantelides, and K. I. Bolotin, Nano Lett. **13**, 3626 (2013).
[15] E. Scalise, M. Houssa, G. Pourtois, V. Afanas'ev, and A. Stesmans, Nano Res. **5** 43 (2012).
[16] P. Johari and V. B. Shenoy, ACS Nano **6** 5449 (2012).
[17] H. Peelaers and C. G. van de Walle, Phys. Rev. B **86**, 241401 (2012).
[18] M. Ghorbani-Asl, N. Zibouche, M. Wahiduzzaman, A. F. Oliveira, A. Kuc, and T. Heine, Sci. Rep. **3**, 2961 (2013).

[19] D. Xiao, G.-B. Liu, W. Feng, X. Xu, and W. Yao, Phys. Rev. Lett. **108**, 196802 (2012).
[20] H. Zeng, J. Dai, W. Yao, D. Xiao, and X. Cui, Nat. Nanotechnol. **7**, 490 (2012).
[21] K.-F. Mak, K. He, J. Shan, and T. F. Heinz, Nat. Nanotechnol. **7**, 494 (2012).
[22] T. Cao *et al.*, Nat. Commun. **3**, 887 (2012).
[23] A. M. Jones *et al.*, Nat. Nanotechnol. **8**, 634 (2013).
[24] S. Wu *et al.*, Nat. Phys. **9**, 149 (2013).
[25] Z. Gong, G.-B. Liu, H. Yu, D. Xiao, X. Cui, X. Xu, and W. Yao, Nat. Commun. **4**, 1 (2013).
[26] P. San-Jose, E. Prada, E. McCann, and H. Schomerus, Phys. Rev. Lett. **102**, 247204 (2009).
[27] H. K. Min, G. Borghi, M. Polini, and A. H. MacDonald, Phys. Rev. B **77**, 041407(R) (2008).
[28] L. D. Landau and E. M. Lifshitz, *Theory of Elasticity* (Oxford, New York, 1986), 3rd ed.
[29] D. Porezag, T. Frauenheim, T. Köhler, G. Seifert, and R. Kaschner, Phys. Rev. B, **51**, 12947 (1995).
[30] G. Seifert, H. Terrones, M. Terrones, G. Jungnickel, and T. Frauenheim, Phys. Rev. Lett. **85**, 146 (2000).
[31] D. Y. Qiu, F. H. da Jornada, and S. G. Louie, Phys. Rev. Lett. **111**, 216805 (2013).
[32] H. Shi, H. Pan, Y.-W. Zhang, and B. I. Yakobson, Phys. Rev. B **87**, 155304 (2013).
[33] N. Zibouche, A. Kuc, and T. Heine, Eur. Phys. J. B **85**, 49 (2012).
[34] M. Ghorbani-Asl, S. Borini, A. Kuc, and T. Heine, Phys. Rev. B **87**, 235434 (2013).
[35] See Supplemental Material at http://link.aps.org/supplemental/10.1103/PhysRevLett.112.186802, which includes Refs. [50–53].
[36] T. Dumitrică, and R. D. James, J. Mech. Phys. Solids **55**, 2206 (2007).
[37] P. Koskinen and O. O. Kit, Phys. Rev. Lett. **105**, 106401 (2010).
[38] P. Koskinen and V. Mäkinen, Comput. Mater. Sci. **47**, 237 (2009).
[39] I. Milošević, B. Nikolić, E. Dobardžić, M. Damnjanović, I. Popov, and G. Seifert, Phys. Rev. B, **76**, 233414 (2007).
[40] O. O. Kit, L. Pastewka, and P. Koskinen, Phys. Rev. B **84**, 155431 (2011).
[41] P. Koskinen and O. O. Kit, Phys. Rev. B **82**, 235420 (2010).
[42] P. Koskinen, Phys. Rev. B **82**, 193409 (2010).
[43] L. Mattheiss, Phys. Rev. B **8** 3719 (1973).
[44] A. Kormányos, V. Zólyomi, N. Drummond, P. Rakyta, G. Burkard, and V. Fal'ko, Phys. Rev. B **88** 045416 (2013).
[45] T. Li, J. Galli, J. Phys. Chem. C **111**, 16192 (2007).
[46] The effect from curvature alone is negligible because even the smallest radii of curvatures are above ~100 Å.
[47] T. Cheiwchanchamnangij, W. R. L. Lambrecht, Y. Song, and H. Dery, Phys. Rev. B **88**, 155404 (2013).
[48] A. Castellanos-Gomez, H. S. van der Zant, and G. A. Steele, arXiv:1309.4433.
[49] K. F. Mak, K. He, C. Lee, G. H. Lee, J. Hone, T. F. Heinz, and J. Shan, Nat. Mater. **12**, 207 (2013).
[50] G. Kresse and J. Furthmüller, J. Comput. Math. Sci. Teach. **6**, 15 (1996); Phys. Rev. B **54**, 11169 (1996).
[51] J. Klimeš, D. R. Bowler, and A. Michaelides, Phys. Rev. B **83**, 195131 (2011).
[52] P. E. Blöchl, Phys. Rev. B **50**, 17953 (1994).
[53] G. Kresse and D. Joubert, Phys. Rev. B **59**, 1758 (1999).

BIBLIOGRAPHY

[1] Acharya, C. K., Sullivan, D. I., and Turner, C. H. Characterizing the interaction of Pt and PtRu clusters with Boron-Doped, Nitrogen-Doped, and Activated Carbon: Density Functional Theory Calculations and Parameterization. *The Journal of Physical Chemistry C 112*, 35 (2008), 13607–13622.

[2] Acharya, C.K., and Turner, C.H. CO oxidation with Pt(111) supported on pure and boron-doped carbon: A DFT investigation. *Surface Science 602*, 23 (2008), 3595 – 3602.

[3] Ackermann, M. D., Pedersen, T. M., Hendriksen, B. L. M., Robach, O., Bobaru, S. C., Popa, I., Quiros, C., Kim, H., Hammer, B., Ferrer, S., and Frenken, J. W. M. Structure and reactivity of surface oxides on pt(110) during catalytic co oxidation. *Physical Review Letters 95* (2005), 255505.

[4] Alavi, A., Hu, P., Deutsch, T., Silvestrelli, P. L., and Hutter, J. CO oxidation on Pt(111): An *Ab Initio* Density Functional Theory Study. *Physical Review Letters 80* (1998), 3650–3653.

[5] Albe, K., Nordlund, K., and Averback, R. S. Modeling the metal-semiconductor interaction: Analytical bond-order potential for platinum-carbon. *Physical Review B Rev. B 65* (2002), 195124.

[6] Allian, A. D., Takanabe, K., Fujdala, K. L., Hao, X., Truex, T. J., Cai, J., Buda, C., Neurock, M., and Iglesia, E. Chemisorption of CO and mechanism of CO oxidation on Supported Platinum Nanoclusters. *Journal of the American Chemical Society 133*, 12 (2011), 4498–4517.

[7] Anderson, J.R., and Boudart, M. *Catalysis: science and technology.* Catalysis: Science and Technology. Springer-Verlag, 1996.

[8] Antolini, E. Carbon supports for low-temperature fuel cell catalysts. *Applied Catalysis B: Environmental 88*, 1–2 (2009), 1 – 24.

[9] Antolini, E. Graphene as a new carbon support for low-temperature fuel cell catalysts. *Applied Catalysis B: Environmental 123–124* (2012), 52 – 68.

[10] Antolini, E., Cardellini, F., Giacometti, E., and Squadrito, G. Study on the formation of Pt/C catalysts by non-oxidized active carbon support and a sulfur-based reducing agent. *Journal of Materials Science 37*, 1 (2002), 133–139.

[11] Arai, H., and Machida, M. Thermal stabilization of catalyst supports and their application to high-temperature catalytic combustion. *Applied Catalysis A: General 138*, 2 (1996), 161 – 176.

[12] Auer, E., Freund, A., Pietsch, J., and Tacke, T. Carbons as supports for industrial precious metal catalysts. *Applied Catalysis A: General 173*, 2 (1998), 259 – 271.

[13] Bader, R. F. W. A quantum theory of molecular structure and its applications. *Chemical Reviews 91*, 5 (1991), 893–928.

[14] Bagri, A., Mattevi, C., Acik, M., Chabal, Y. J, Chhowalla, M., and Shenoy, V. B. Structural evolution during the reduction of chemically derived graphene oxide. *Nature Chemistry 2*, 7 (2010), 581–7.

[15] Baletto, F., and Ferrando, R. Structural properties of nanoclusters: Energetic, thermodynamic, and kinetic effects. *Review of Modern Physics 77* (2005), 371–423.

[16] Baschuk, J. J., and Li, Xianguo. Carbon monoxide poisoning of proton exchange membrane fuel cells. *International Journal of Energy Research 25*, 8 (2001), 695–713.

[17] Bessel, C. A., Laubernds, K., Rodriguez, N. M., and Baker, R. Terry K. Graphite nanofibers as an electrode for fuel cell applications. *The Journal of Physical Chemistry B 105*, 6 (2001), 1115–1118.

[18] Blöchl, P. E. Projector augmented-wave method. *Physical Review B 50* (1994), 17953–17979.

[19] Blonski, P., and Hafner, J. Geometric and magnetic properties of Pt clusters supported on graphene: Relativistic density-functional calculations. *The Journal of Chemical Physics 134*, 15 (2011), 154705.

[20] Bong, S., Kim, Y.-R., Kim, I., Woo, S., Uhm, S., Lee, J., and Kim, H. Graphene supported electrocatalysts for methanol oxidation. *Electrochemistry Communications 12*, 1 (2010), 129 – 131.

[21] Bonzel, H.P, and Burton, J.J. CO oxidation on a Pt(110) surface: Solution of a reaction model. *Surface Science 52*, 1 (1975), 223 – 229.

[22] Cabria, I., López, M. J., and Alonso, J. A. Theoretical study of the transition from planar to three-dimensional structures of palladium clusters supported on graphene. *Physical Review B 81* (2010), 035403.

[23] Cao, D., Lu, G.-Q., Wieckowski, A., Wasileski, S. A., and Neurock, M. Mechanisms of methanol decomposition on platinum: a combined experimental and ab initio approach. *The Journal of Physical Chemistry B 109*, 23 (2005), 11622–11633. PMID: 16852427.

[24] Carmo, M., Paganin, V.A., Rosolen, J.M., and Gonzalez, E.R. Alternative supports for the preparation of catalysts for low-temperature fuel cells: the use of carbon nanotubes. *Journal of Power Sources 142*, 1–2 (2005), 169 – 176.

[25] Chang, C. M., and Chou, M. Y. Alternative Low-Symmetry Structure for 13-Atom Metal Clusters. *Physical Review Letters 93* (2004), 133401.

[26] Chang, H., Joo, S. H., and Pak, C. Synthesis and characterization of mesoporous carbon for fuel cell applications. *Journal of Material Chemistry 17* (2007), 3078–3088.

[27] Chen, M.S., Cai, Y., Yan, Z., Gath, K.K., Axnanda, S., and Goodman, D. Wayne. Highly active surfaces for CO oxidation on Rh, Pd, and Pt. *Surface Science 601*, 23 (2007), 5326 – 5331.

[28] Chen, Xiaomei, Wu, Genghuang, Chen, Jinmei, Chen, Xi, Xie, Zhaoxiong, and Wang, Xiaoru. Synthesis of "clean" and well-dispersive pd nanoparticles with excellent electrocatalytic property on graphene oxide. *Journal of the American Chemical Society 133*, 11 (2011), 3693–3695.

[29] Cheng, X., Shi, Z., Glass, N., Zhang, L., Zhang, J., Song, D., Liu, Z.-S., Wang, H., and Shen, J. A review of PEM hydrogen fuel cell contamination: Impacts, mechanisms, and mitigation. *Journal of Power Sources 165*, 2 (2007), 739 – 756.

[30] Chi, D. H., Cuong, N. T., Tuan, N. A., Kim, Y.-T., Bao, H. T., Mitani, T., Ozaki, T., and Nagao, H. Electronic structures of Pt clusters adsorbed on (5,5) single wall carbon nanotube. *Chemical Physics Letters 432*, 1–3 (2006), 213 – 217.

[31] Creighan, S.C., Mukerji, R.J., Bolina, A.S., Lewis, D.W., and Brown, W.A. The Adsorption of CO on the Stepped Pt211 Surface: A Comparison of Theory and Experiment. *Catalysis Letters 88*, 1-2 (2003), 39–45.

[32] Cuong, N. T., Fujiwara, A., Mitani, T., and Chi, D. H. Effects of carbon supports on Pt nano-cluster catalyst. *Computational Materials Science 44*, 1 (2008), 163 – 166.

[33] Cuong, N. T, Sugiyama, A., Fujiwara, A., Mitani, T., and Chi, D. H. Density functional study of Pt_4 clusters adsorbed on a carbon nanotube support. *Physical Review B 79* (2009), 235417.

[34] Curulla, D., Clotet, A., Ricart, J. M., and Illas, F. Ab initio cluster model study of the chemisorption of CO on low-index platinum surfaces. *The Journal of Physical Chemistry B 103*, 25 (1999), 5246–5255.

[35] Dai, X.-Q., Tang, Y.-N., Zhao, J.-H., and Dai, Y.-W. Absorption of Pt clusters and the induced magnetic properties of graphene. *Journal of Physics: Condensed Matter 22*, 31 (2010), 316005.

[36] Das, S. K., Reis, A., and Berry, K.J. Experimental evaluation of CO poisoning on the performance of a high temperature proton exchange membrane fuel cell. *Journal of Power Sources 193*, 2 (2009), 691 – 698.

[37] Ding, J., Chan, K.-Y., Ren, J., and Xiao, F.-S. Platinum and platinum–ruthenium nanoparticles supported on ordered mesoporous carbon and their electrocatalytic performance for fuel cell reactions. *Electrochimica Acta 50*, 15 (2005), 3131 – 3141.

[38] Divya, P., and Ramaprabhu, S. Platinum-graphene hybrid nanostructure as anode and cathode electrocatalysts in proton exchange membrane fuel cells. *Journal of Material Chemistry A 2* (2014), 4912–4918.

[39] Dobrin, S. CO oxidation on Pt nanoclusters, size and coverage effects: a density functional theory study. *Physical Chemistry Chemical Physics 14* (2012), 12122–12129.

[40] Dong, L., Gari, R. R. S., Li, Z., Craig, M. M., and Hou, S. Graphene-supported platinum and platinum–ruthenium nanoparticles with high electrocatalytic activity for methanol and ethanol oxidation. *Carbon 48*, 3 (2010), 781 – 787.

[41] Durbin, D. J. D., and Malardier-Jugroot, C. Density Functional Theory Analysis of Metal/Graphene Systems as a Filter Membrane to Prevent CO Poisoning in Hydrogen Fuel Cells. *The Journal of Physical Chemistry C 115*, 3 (2011), 808–815.

[42] E., Antolini. Formation of carbon-supported PtM alloys for low temperature fuel cells: a review. *Materials Chemistry and Physics 78*, 3 (2003), 563 – 573.

[43] Eichler, A. CO oxidation on transition metal surfaces: reaction rates from first principles. *Surface Science 498*, 3 (2002), 314 – 320.

[44] Eichler, A., and Hafner, J. Reaction channels for the catalytic oxidation of CO on Pt(111). *Physical Review B 59* (1999), 5960–5967.

[45] Fampiou, I., and Ramasubramaniam, A. Binding of Pt Nanoclusters to Point Defects in Graphene: Adsorption, Morphology, and Electronic Structure. *The Journal of Physical Chemistry C 116*, 11 (2012), 6543–6555.

[46] Fampiou, I., and Ramasubramaniam, A. Co adsorption on defective graphene-supported pt13 nanoclusters. *The Journal of Physical Chemistry C 117*, 39 (2013), 19927–19933.

[47] Farkas, A., Zalewska-Wierzbicka, K., Bachmann, C., Goritzka, J., Langsdorf, D., Balmes, O., Janek, J., and Over, H. High pressure carbon monoxide oxidation over Platinum (111). *The Journal of Physical Chemistry C 117*, 19 (2013), 9932–9942.

[48] Fraga, M.A., Jordão, E., Mendes, M.J., Freitas, M.M.A., Faria, J.L., and Figueiredo, J.L. Properties of Carbon-supported Platinum Catalysts: Role of carbon surface sites. *Journal of Catalysis 209*, 2 (2002), 355 – 364.

[49] Gan, Y., Sun, L., and Banhart, F. One- and Two-Dimensional Diffusion of Metal Atoms in Graphene. *Small 4*, 5 (2008), 587–591.

[50] García-Diéguez, M., and Iglesia, E. Structure sensitivity via decoration of low-coordination exposed metal atoms: CO oxidation catalysis on Pt clusters. *Journal of Catalysis 301* (2013), 198 – 209.

[51] Gattia, D. M., Antisari, M. V., Giorgi, L., Marazzi, R., Piscopiello, E., Montone, A., Bellitto, S., Licoccia, S., and Traversa, E. Study of different nanostructured carbon supports for fuel cell catalysts. *Journal of Power Sources 194*, 1 (2009), 243 – 251.

[52] Gerrard, A. L., and Weaver, J. F. Kinetics of co oxidation on high-concentration phases of atomic oxygen on pt(111). *The Journal of Chemical Physics 123* (2005), 224703.

[53] Gong, X.-Q., Liu, Z.-P., Raval, R., and Hu, P. A systematic study of CO oxidation on metals and metal oxides: density functional theory calculations. *Journal of the American Chemical Society 126*, 1 (2004), 8–9.

[54] Grabow, L., Xu, Y., and Mavrikakis, M. Lattice strain effects on CO oxidation on Pt (111). *Physical Chemistry Chemical Physics 8* (2006), 3369–3374.

[55] Greeley, J., and Mavrikakis, M. A first-principles study of methanol decomposition on Pt(111). *Journal of the American Chemical Society 124*, 24 (2002), 7193–7201.

[56] Greeley, J., and Mavrikakis, M. Competitive paths for methanol decomposition on Pt(111). *Journal of the American Chemical Society 126*, 12 (2004), 3910–3919. PMID: 15038745.

[57] Greeley, J., Nørskov, J. K., and Mavrikakis, M. Electronic structure and catalysis on metal surfaces. *Annual Review of Physical Chemistry 53*, 1 (2002), 319–348.

[58] Guha, A., Lu, W., Zawodzinski, T. A., and Schiraldi, D. A. Surface-modified carbons as platinum catalyst support for PEM fuel cells. *Carbon 45*, 7 (2007), 1506 – 1517.

[59] Guo, D.-J., and Li, H.-L. Electrocatalytic oxidation of methanol on Pt modified single-walled carbon nanotubes. *Journal of Power Sources 160*, 1 (2006), 44 – 49.

[60] Ha, H.-W., Kim, I. Y., Hwang, S.-J., and Ruoff, R. S. One-pot synthesis of Platinum nanoparticles Embedded on Reduced Graphene Oxide for Oxygen Reduction in Methanol Fuel Cells. *Electrochemical and Solid-State Letters 14*, 7 (2011), B70–B73.

[61] Hammer, B., Morikawa, Y., and Nørskov, J. K. CO Chemisorption at Metal Surfaces and Overlayers. *Physical Review Letters 76* (1996), 2141–2144.

[62] Hammer, B., Nielsen, O.H., and Nørskov, J. K. Structure sensitivity in adsorption: CO interaction with stepped and reconstructed Pt surfaces. *Catalysis Letters 46*, 1-2 (1997), 31–35.

[63] Hammer, B., and Nørskov, J. K. Electronic factors determining the reactivity of metal surfaces. *Surface Science 343*, 3 (1995), 211 – 220.

[64] Hammer, B., and Nørskov, J. K. Why gold is the noblest of all the metals. *Nature 376*, 6537 (1995), 238–240.

[65] Hammer, B., and Nørskov, J. K. Theoretical surface science and catalysis—calculations and concepts. In *Impact of Surface Science on Catalysis*, vol. 45 of *Advances in Catalysis*. Academic Press, 2000, pp. 71 – 129.

[66] Haug, A. T., White, R. E., Weidner, J. W., and Huang, W. Development of a Novel CO Tolerant Proton Exchange Membrane Fuel Cell Anode. *Journal of The Electrochemical Society 149*, 7 (2002), A862–A867.

[67] He, C.-L., Jiang, Y.-X., Rao, L., Wang, Q., Zhang, B.-W., Li, Y.-Y., and Sun, S.-G. Synthesis of ultrafine size Platinum nanoparticles on defective graphene with enhanced performance towards methanol electro-oxidation. *Fuel Cells 13*, 5 (2013), 873–880.

[68] He, D., Cheng, K., Li, H., Peng, T., Xu, F., Mu, S., and Pan, M. Highly active Platinum nanoparticles on graphene nanosheets with a significant improvement in stability and CO tolerance. *Langmuir 28*, 8 (2012), 3979–3986.

[69] He, Z., Chen, J., Liu, D., Zhou, H., and Kuang, Y. Electrodeposition of Pt–Ru nanoparticles on carbon nanotubes and their electrocatalytic properties for methanol electrooxidation. *Diamond and Related Materials 13*, 10 (2004), 1764 – 1770.

[70] Henkelman, G., Arnaldsson, A., and Jónsson, H. A fast and robust algorithm for Bader decomposition of charge density. *Computational Materials Science 36*, 3 (2006), 354 – 360.

[71] Henkelman, G., Uberuaga, B. P., and Jonsson, H. Jónsson. A climbing image nudged elastic band method for finding saddle points and minimum energy paths. *The Journal of Chemical Physics 113*, 22 (2000), 9901–9904.

[72] Hopster, H., Ibach, H., and Comsa, G. Catalytic oxidation of carbon monoxide on stepped platinum(111) surfaces. *Journal of Catalysis 46*, 1 (1977), 37 – 48.

[73] Jennison, D. R., Schultz, P. A., and Sears, M. P. Ab Initio Ammonia and CO Lateral Interactions on Pt (111). *Phys. Rev. Lett. 77* (Dec 1996), 4828–4831.

[74] Jha, N., Reddy, A. L. M., Shaijumon, M. M., Rajalakshmi, N., and Ramaprabhu, S. Pt–Ru/multi-walled carbon nanotubes as electrocatalysts for direct methanol fuel cell. *International Journal of Hydrogen Energy 33*, 1 (2008), 427 – 433.

[75] Jiang, S. P., and Shen, P. K. *Nanostructured and Advanced Materials for Fuel Cells.* Advances in Materials Science and Engineering. Taylor & Francis, 2013.

[76] Jiang, T., Mowbray, D. J., Dobrin, S., Falsig, H., Hvolbæk, B., Bligaard, T., and Nørskov, J. K. Trends in CO oxidation rates for metal nanoparticles and close-packed, stepped, and kinked surfaces. *The Journal of Physical Chemistry C 113*, 24 (2009), 10548–10553.

[77] Jin, Z., Nackashi, D., Lu, W., Kittrell, C., and Tour, J. M. Decoration, Migration, and Aggregation of Palladium Nanoparticles on Graphene Sheets. *Chemistry of Materials 22*, 20 (2010), 5695–5699.

[78] Kangasniemi, K. H., Condit, D. A., and Jarvi, T. D. Characterization of Vulcan electrochemically oxidized under simulated PEM fuel cell conditions. *Journal of The Electrochemical Society 151*, 4 (2004), E125–E132.

[79] Karmazyn, A.D., Fiorin, V., Jenkins, S.J., and King, D.A. First-principles theory and microcalorimetry of CO adsorption on the 211 surfaces of Pt and Ni. *Surface Science 538*, 3 (2003), 171 – 183.

[80] Kim, G., and Jhi, S.-H. Carbon Monoxide-Tolerant Platinum Nanoparticle Catalysts on Defect-Engineered Graphene. *ACS Nano 5*, 2 (2011), 805–810.

[81] Kong, K.-J., C., Youngmin, Ryu, B.-H., Lee, J.-O, and Chang, H. Investigation of metal/carbon-related materials for fuel cell applications by electronic structure calculations. *Materials Science and Engineering: C 26*, 5–7 (2006), 1207 – 1210.

[82] Kongkanand, A., Kuwabata, S., Girishkumar, G., and Kamat, P. Single–Wall Carbon Nanotubes Supported Platinum Nanoparticles with Improved Electrocatalytic Activity for Oxygen Reduction Reaction. *Langmuir 22*, 5 (2006), 2392–2396.

[83] Kou, R., Shao, Y., Mei, D., Nie, Z., Wang, D., Wang, C., Viswanathan, V. V., Park, S., Aksay, I. A., Lin, Y., Wang, Y., and Liu, J. Stabilization of Electrocatalytic Metal Nanoparticles at Metal-Metal Oxide-Graphene Triple Junction Points. *Journal of the American Chemical Society 133*, 8 (2011), 2541–2547.

[84] Kou, R., Shao, Y., Wang, D., Engelhard, M. H., Kwak, J. H., Wang, J., Viswanathan, V. V., Wang, C., Lin, Y., Wang, Y., Aksay, I. A., and Liu, J. Enhanced activity and stability of Pt catalysts on functionalized graphene sheets for electrocatalytic oxygen reduction. *Electrochemistry Communications 11*, 5 (2009), 954 – 957.

[85] Krasheninnikov, A. V., Lehtinen, P. O., Foster, A. S., Pyykkö, P., and Nieminen, R. M. Embedding Transition-Metal Atoms in Graphene: Structure, Bonding, and Magnetism. *Physical Review Letters 102* (2009), 126807.

[86] Kresse, G., and Furthmüller, J. Efficiency of ab-initio total energy calculations for metals and semiconductors using a plane-wave basis set. *Computational Materials Science 6*, 1 (1996), 15 – 50.

[87] Kresse, G., and Furthmüller, J. Efficient iterative schemes for *ab initio* total-energy calculations using a plane-wave basis set. *Physical Review B 54* (1996), 11169–11186.

[88] Kresse, G., and Joubert, D. From ultrasoft pseudopotentials to the projector augmented-wave method. *Physical Review B 59* (1999), 1758–1775.

[89] Kumar, V., and Kawazoe, Y. Evolution of atomic and electronic structure of Pt clusters: Planar, layered, pyramidal, cage, cubic, and octahedral growth. *Physical Review B 77* (2008), 205418.

[90] Kundu, P., Nethravathi, C., Deshpande, P. A., Rajamathi, M., Madras, G., and Ravishankar, N. Ultrafast microwave-assisted route to surfactant-free ultrafine Pt nanoparticles on graphene: Synergistic CO-reduction mechanism and high catalytic activity. *Chemistry of Materials 23*, 11 (2011), 2772–2780.

[91] Lee, G.-D., Wang, C. Z., Yoon, E., Hwang, N.-M., and Ho, K. M. Vacancy defects and the formation of local haeckelite structures in graphene from tight-binding molecular dynamics. *Physical Review B 74* (2006), 245411.

[92] Lee, G.-D., Wang, C. Z., Yoon, E., Hwang, N.-M., Kim, D.-Y., and Ho, K. M. Diffusion, Coalescence, and Reconstruction of Vacancy Defects in Graphene Layers. *Physical Review Letters 95* (2005), 205501.

[93] Lee, J. H., Shin, D. W., Makotchenko, V. G., Nazarov, A. S., Fedorov, V. E., Kim, Y. H., Choi, J.-Y., Kim, J. M., and Yoo, J.-B. One-step exfoliation synthesis of easily soluble graphite and transparent conducting graphene sheets. *Advanced Materials 21*, 43 (2009), 4383–4387.

[94] Lee, Kunchan, Zhang, Jiujun, Wang, Haijiang, and Wilkinson, David P. Progress in the synthesis of carbon nanotube- and nanofiber-supported pt electrocatalysts for pem fuel cell catalysis. *Journal of Applied Electrochemistry 36*, 5 (2006), 507–522.

[95] Li, F., Zhao, J., and Chen, Z. Fe-Anchored Graphene Oxide: A Low-Cost and Easily Accessible Catalyst for Low-Temperature CO Oxidation. *The Journal of Physical Chemistry C 116*, 3 (2012), 2507–2514.

[96] Li, J.-L., Kudin, K. N., McAllister, M. J., Prud'homme, R. K., Aksay, I. A., and Car, R. Oxygen-Driven Unzipping of Graphitic Materials. *Physical Review Letters 96* (2006), 176101.

[97] Li, L., and Xing, Y. Electrochemical durability of carbon nanotubes in noncatalyzed and catalyzed oxidations. *Journal of The Electrochemical Society 153*, 10 (2006), A1823–A1828.

[98] Li, W., Liang, C., Qiu, J., Zhou, W., Han, H., Wei, Z., Sun, G., and Xin, Q. Carbon nanotubes as support for cathode catalyst of a direct methanol fuel cell. *Carbon 40*, 5 (2002), 791 – 794.

[99] Li, W., Liang, C., Zhou, W., Qiu, J., Sun, G., and Xin, Q. Preparation and characterization of multiwalled carbon nanotube-supported platinum for cathode catalysts of direct methanol fuel cells. *The Journal of Physical Chemistry B 107*, 26 (2003), 6292–6299.

[100] Li, W., Waje, M., Chen, Z.i, Larsen, P., and Yan, Y. Platinum nanopaticles supported on stacked-cup carbon nanofibers as electrocatalysts for proton exchange membrane fuel cell. *Carbon 48* (2010), 995–1003.

[101] Li, Y., Gao, W., Ci, L., Wang, C., and Ajayan, P. M. Catalytic performance of Pt nanoparticles on reduced graphene oxide for methanol electro-oxidation. *Carbon 48*, 4 (2010), 1124 – 1130.

[102] Li, Y., Tang, L., and Li, J. Preparation and electrochemical performance for methanol oxidation of Pt/graphene nanocomposites. *Electrochemistry Communications 11*, 4 (2009), 846 – 849.

[103] Li, Y., Zhou, Z., Yu, G., Chen, W., and Chen, Z. CO catalytic oxidation on iron-embedded graphene: Computational quest for low-cost nanocatalysts. *The Journal of Physical Chemistry C 114*, 14 (2010), 6250–6254.

[104] Lim, D.-H., Negreira, A. S., and Wilcox, J. DFT studies on the interaction of defective graphene-supported Fe and Al nanoparticles. *The Journal of Physical Chemistry C 115*, 18 (2011), 8961–8970.

[105] Lim, D.-H., and Wilcox, J. DFT-based study on Oxygen adsorption on defective graphene-supported Pt nanoparticles. *The Journal of Physical Chemistry C 115*, 46 (2011), 22742–22747.

[106] Lim, D.-H., and Wilcox, J. Mechanisms of the oxygen reduction reaction on defective graphene-supported pt nanoparticles from first-principles. *The Journal of Physical Chemistry C 116*, 5 (2012), 3653–3660.

[107] Lindström, B., and Pettersson, L. J. A brief history of catalysis. *CATTECH 7*, 4 (2003), 130–138.

[108] Liu, J., Zhou, Z., Zhao, X., Xin, Q., Sun, G., and Yi, B. Studies on performance degradation of a direct methanol fuel cell (DMFC) in life test. *Physical Chemistry Chemical Physics 6* (2004), 134–137.

[109] Liu, X., Li, L., Meng, C., and Han, Y. Palladium Nanoparticles/Defective Graphene Composites as Oxygen Reduction Electrocatalysts: A First-Principles Study. *The Journal of Physical Chemistry C 116*, 4 (2012), 2710–2719.

[110] Liu, Z., Lin, X., Lee, J. Y., Zhang, W., Han, M., and Gan, L. M. Preparation and characterization of platinum-based electrocatalysts on multiwalled carbon nanotubes for proton exchange membrane fuel cells. *Langmuir 18*, 10 (2002), 4054–4060.

[111] Liu, Z.-P., and Hu, P. General trends in the barriers of catalytic reactions on transition metal surfaces. *The Journal of Chemical Physics 115* (2001), 4977–4980.

[112] Logsdail, A. J., and Akola, J. Interaction of Au_{16} Nanocluster with Defects in Supporting Graphite: A Density-Functional Study. *The Journal of Physical Chemistry C 115*, 31 (2011), 15240–15250.

[113] Longo, R. C., and Gallego, L. J. Structures of 13-atom clusters of fcc transition metals by *ab initio* and semiempirical calculations. *Phys. Rev. B 74* (2006), 193409.

[114] Lu, Y.-H., Zhou, M., Zhang, C., and Feng, Y.-P. Metal-Embedded Graphene: A Possible Catalyst with High Activity. *The Journal of Physical Chemistry C 113*, 47 (2009), 20156–20160.

[115] M., Kinne, T., Fuhrmann, F., Zhu J., M., Whelan C., R., Denecke, and H.-P., Steinrück. Kinetics of the co oxidation reaction on Pt(111) studied by in situ high-resolution x-ray photoelectron spectroscopy. *The Journal of Chemical Physics 120* (2004), 7113–7122.

[116] Maillard, F., Simonov, P. A., and Savinova, E. R. *Carbon Materials as Supports for Fuel Cell Electrocatalysts*. John Wiley Sons, Inc., 2008, pp. 429–480.

[117] Maiti, A., and Ricca, A. Metal–nanotube interactions – binding energies and wetting properties. *Chemical Physics Letters 395*, 1–3 (2004), 7 – 11.

[118] Mason, S. E., Grinberg, I., and Rappe, A. M. Adsorbate-adsorbate interactions and chemisorption at different coverages studied by accurate b initio calculations:CO on transition metal surfaces. *The Journal of Physical Chemistry B 110*, 8 (2006), 3816–3822.

[119] Matsumoto, T., Komatsu, T., Nakano, H., Arai, K., Nagashima, Y., Yoo, E., Yamazaki, T., Kijima, M., Shimizu, H., Takasawa, Y., and Nakamura, J. Efficient usage of highly dispersed Pt on carbon nanotubes for electrode catalysts of polymer electrolyte fuel cells. *Catalysis Today 90*, 3–4 (2004), 277 – 281.

[120] McClure, S. M., and Goodman, D. W. New insights into catalytic CO oxidation on Pt-group metals at elevated pressures. *Chemical Physics Letters 469*, 1–3 (2009), 1 – 13.

[121] Methfessel, M., and Paxton, A. T. High–precision sampling for Brillouin–zone integration in metals. *Physical Review B 40* (1989), 3616–3621.

[122] Morrow, B. H., and Striolo, A. Platinum nanoparticles on carbonaceous materials: the effect of support geometry on nanoparticle mobility, morphology, and melting. *Nanotechnology 19*, 19 (2008), 195711.

[123] Nakai, I., Kondoh, H., Amemiya, K., Nagasaka, M., Nambu, A., Shimada, T., and Ohta, T. Reaction-path switching induced by spatial-distribution change of reactants: CO oxidation on Pt(111). *The Journal of Chemical Physics 121* (2004), 5035–5038.

[124] Nørskov, J. K., Abild-Pedersen, F., Studt, F., and Bligaard, T. Density functional theory in surface chemistry and catalysis. *Proceedings of the National Academy of Sciences 108*, 3 (2011), 937–943.

[125] Novoselov, K. S., Geim, A. K., Morozov, S. V., Jiang, D., Katsnelson, M. I., Grigorieva, I. V., Dubonos, S. V., and Firsov, A. A. Two-dimensional gas of massless dirac fermions in graphene. *Nature 438*, 7065 (2005), 197–200.

[126] Novoselov, K. S., Geim, A. K., Morozov, S. V., Jiang, D., Zhang, Y., Dubonos, S. V., Grigorieva, I. V., and Firsov, A. A. Electric field effect in atomically thin carbon films. *Science 306*, 5696 (2004), 666–669.

[127] Ohnishi, S., and Watari, N. Cluster-model study of CO adsorption on the Pt(111) surface. *Physical Review B 49* (1994), 14619–14627.

[128] Okamoto, Y. Density-functional calculations of icosahedral M_{13} (m=Pt and Au) clusters on graphene sheets and flakes. *Chemical Physics Letters 420*, 4–6 (2006), 382 – 386.

[129] Okazaki-Maeda, K., Morikawa, Y., Tanaka, S., and Kohyama, M. Structures of Pt clusters on graphene by first-principles calculations. *Surface Science 604*, 2 (2010), 144 – 154.

[130] Orita, H., and Inada, Y. DFT Investigation of CO Adsorption on Pt (211) and Pt (311) Surfaces from Low to High Coverage. *The Journal of Physical Chemistry B 109*, 47 (2005), 22469–22475.

[131] Paci, J. T., Belytschko, T., and Schatz, G. C. Computational Studies of the Structure, Behavior upon Heating, and Mechanical Properties of Graphite Oxide. *The Journal of Physical Chemistry C 111*, 49 (2007), 18099–18111.

[132] Perdew, J. P., Burke, K., and Ernzerhof, M. Generalized Gradient Approximation Made Simple. *Physical Review Letters 77* (1996), 3865–3868.

[133] Philippot, K., and Serp, P. *Concepts in Nanocatalysis.* Wiley-VCH Verlag GmbH Co. KGaA, 2013, pp. 1–54.

[134] Philipsen, P. H. T., van Lenthe, E., Snijders, J. G., and Baerends, E. J. Relativistic calculations on the adsorption of co on the (111) surfaces of ni, pd, and pt within the zeroth-order regular approximation. *Physical Review B 56* (1997), 13556–13562.

[135] Planeix, J.M, Coustel, N., Coq, B., Brotons, V., Kumbhar, P. S., Dutartre, R., Geneste, P., Bernier, P., and Ajayan, P. M. Application of Carbon Nanotubes as Supports in Heterogeneous Catalysis. *Journal of the American Chemical Society 116*, 17 (1994), 7935–7936.

[136] Plimpton, S. Fast Parallel Algorithms for Short-Range Molecular Dynamics. *Journal of Computational Physics 117*, 1 (1995), 1 – 19.

[137] Pu, N.-W., Wang, C.-A., Liu, Y.-M., Liu, D.-Y., Wang, P.-C., and Ger, M.-D. Graphene-supported platinum nanoparticles prepared by a self-regulated reduction method. *Journal of Nanoscience and Nanotechnology 13*, 8 (2013), 5702–5707.

[138] Pumera, M. Electrochemistry of graphene: new horizons for sensing and energy storage. *The Chemical Record 9*, 4 (2009), 211–223.

[139] Qian, W., Hao, R., Zhou, J., Eastman, M., Manhat, B. A., Sun, Q., Goforth, A. M., and Jiao, J. Exfoliated graphene-supported Pt and Pt-based alloys as electrocatalysts for direct methanol fuel cells. *Carbon 52* (2013), 595 – 604.

[140] Qiu, J.-D., Wang, G.-C., Liang, R.-P., Xia, X.-H., and Yu, H.-W. Controllable Deposition of Platinum Nanoparticles on Graphene as an Electrocatalyst for Direct Methanol Fuel Cells. *The Journal of Physical Chemistry C 115*, 31 (2011), 15639–15645.

[141] Ralph, T. R., and Hogarth, M. P. Catalysis for low temperature fuel cells part i : The cathode challenged. *Platinum Metals Review 46*, 1 (2002), 3–14.

[142] Rao, C. V., Reddy, A. L. M., Ishikawa, Y., and Ajayan, P. M. Synthesis and electrocatalytic oxygen reduction activity of graphene-supported Pt_3Co and Pt_3Cr alloy nanoparticles. *Carbon 49*, 3 (2011), 931–936.

[143] Robertson, A. J. B. The Early History of Catalysis. *Platinum Metals Review 19*, 2 (1975), 64–69.

[144] Rodríguez-Manzo, J. A., Cretu, O., and Banhart, F. Trapping of Metal Atoms in Vacancies of Carbon Nanotubes and Graphene. *ACS Nano 4*, 6 (2010), 3422–3428.

[145] Sanz-Navarro, C. F., Astrand, P.-O., Chen, D., Ronning, M., van Duin, A. C. T., Jacob, T., and Goddard, W. A. Molecular Dynamics Simulations of the interactions between Platinum clusters and Carbon platelets. *The Journal of Physical Chemistry A 112*, 7 (2008), 1392–1402.

[146] Scheuermann, G. M., Rumi, L., Steurer, P., Bannwarth, W., and Mülhaupt, R. Palladium Nanoparticles on Graphite Oxide and its Functionalized Graphene Derivatives as Highly Active Catalysts for the Suzuki–Miyaura Coupling Reaction. *Journal of the American Chemical Society 131*, 23 (2009), 8262–8270.

[147] Sebastián, D., Calderón, J.C., González-Expósito, J.A., Pastor, E., Martínez-Huerta, M.V., Suelves, I., Moliner, R., and Lázaro, M.J. Influence of carbon nanofiber properties as electrocatalyst support on the electrochemical performance for PEM fuel cells. *International Journal of Hydrogen Energy 35*, 18 (2010), 9934 – 9942.

[148] Seger, B., and Kamat, P. V. Electrocatalytically Active Graphene-Platinum Nanocomposites. Role of 2D Carbon Support in PEM Fuel Cells. *The Journal of Physical Chemistry C 113*, 19 (2009), 7990–7995.

[149] Seo, M. H., Choi, S. M., Kim, H. J., and Kim, W. B. The graphene-supported Pd and Pt catalysts for highly active oxygen reduction reaction in an alkaline condition. *Electrochemistry Communications 13*, 2 (2011), 182 – 185.

[150] Shan, B., Zhao, Y., Hyun, J., Kapur, N., Nicholas, J. B., and Cho, K. Coverage-dependent CO adsorption energy from first-principles calculations. *The Journal of Physical Chemistry C 113*, 15 (2009), 6088–6092.

[151] Shang, N., Papakonstantinou, P., Wang, P., and Silva, S. R. P. Platinum integrated graphene for methanol fuel cells. *The Journal of Physical Chemistry C 114*, 37 (2010), 15837–15841.

[152] Shao, Y., Yin, G., and Gao, Y. Understanding and approaches for the durability issues of Pt-based catalysts for PEM fuel cell. *Journal of Power Sources 171*, 2 (2007), 558 – 566.

[153] Sharma, S., Ganguly, A., Papakonstantinou, P., Miao, X., Li, M., Hutchison, J. L., Delichatsios, M., and Ukleja, S. Rapid microwave synthesis of CO tolerant reduced graphene oxide–supported platinum electrocatalysts for oxidation of methanol. *The Journal of Physical Chemistry C 114*, 45 (2010), 19459–19466.

[154] Shelef, M., and McCabe, R.W. Twenty-five years after introduction of automotive catalysts: what next? *Catalysis Today 62*, 1 (2000), 35 – 50.

[155] Siburian, R., Kondo, T., and Nakamura, J. Size control to a sub-nanometer scale in platinum catalysts on graphene. *The Journal of Physical Chemistry C 117*, 7 (2013), 3635–3645.

[156] Singh, J., and van Bokhoven, J. A. Structure of alumina supported platinum catalysts of different particle size during CO oxidation using in situ IR and HERFD XAS. *Catalysis Today 155*, 3–4 (2010), 199 – 205.

[157] Solov'yov, I. A., Solov'yov, A. V., Greiner, W., Koshelev, A., and Shutovich, A. Cluster growing process and a sequence of magic numbers. *Physical Review Letters 90* (2003), 053401.

[158] Somorjai, G.A., and Li, Y. *Introduction to Surface Chemistry and Catalysis.* John Wiley & Sons, 2010.

[159] Song, E. H., Wen, Z., and Jiang, Q. CO Catalytic Oxidation on Copper-Embedded Graphene. *The Journal of Physical Chemistry C 115*, 9 (2011), 3678–3683.

[160] Steele, B. C. H., and Heinzel, A. Materials for fuel-cell technologies. *Nature 414*, 6861 (2001), 345–352.

[161] Steigerwalt, E. S., Deluga, G. A., and Lukehart, C. M. PtRu/Carbon fiber nanocomposites: Synthesis, characterization, and performance as anode catalysts of direct methanol fuel cells. a search for exceptional performance. *The Journal of Physical Chemistry B 106*, 4 (2002), 760–766.

[162] Su, F., Zeng, J., Bao, X., Yu, Y., Lee, J. Y., and Zhao, X. S. Preparation and characterization of highly ordered graphitic mesoporous carbon as a pt catalyst support for direct methanol fuel cells. *Chemistry of Materials 17*, 15 (2005), 3960–3967.

[163] Su, H.-Y., Gu, X.-K., Ma, X., Zhao, Y.-H., Bao, X.-H., and Li, W.-X. Structure evolution of Pt-3d transition metal alloys under reductive and oxidizing conditions and effect on the CO oxidation: a first-principles study. *Catalysis Today 165*, 1 (2011), 89 – 95.

[164] Sun, S., Zhang, G., Gauquelin, N., Chen, N., Zhou, J., Yang, S., Chen, W., Meng, X., Geng, D., Banis, M. N., Li, R., Ye, S., Knights, S., Botton, G. A., Sham, T.-K., and Sun, X. Single-atom catalysis using Pt/graphene achieved through atomic layer deposition. *Scientific Reports 3* (2013).

[165] Takasu, Y., Kawaguchi, T., Sugimoto, W., and Murakami, Y. Effects of the surface area of carbon support on the characteristics of highly-dispersed ptru particles as catalysts for methanol oxidation. *Electrochimica Acta 48*, 25–26 (2003), 3861 – 3868.

[166] Tang, H., Chen, J., Nie, L., Liu, D., Deng, W., Kuang, Y., and Yao, S. High dispersion and electrocatalytic properties of platinum nanoparticles on graphitic carbon nanofibers (GCNFs). *Journal of Colloid and Interface Science 269*, 1 (2004), 26 – 31.

[167] Tang, Y., Dai, X., Yang, Z., Pan, L., Chen, W., Ma, D., and Lu, Z. Formation and catalytic activity of Pt supported on oxidized graphene for the CO oxidation reaction. *Physical Chemistry Chemical Physics 16* (2014), 7887–7895.

[168] Tang, Y., Yang, Z., and Dai, X. Trapping of metal atoms in the defects on graphene. *The Journal of Chemical Physics 135*, 22 (2011).

[169] Tang, Y., Yang, Z., and Dai, X. Preventing the CO poisoning on Pt nanocatalyst using appropriate substrate: a first-principles study. *Journal of Nanoparticle Research 14*, 5 (2012).

[170] Tang, Y., Yang, Z., and Dai, X. A theoretical simulation on the catalytic oxidation of co on pt/graphene. *Physical Chemistry Chemical Physics 14* (2012), 16566–16572.

[171] Tang, Y., Yang, Z., Dai, X., Ma, D., and Fu, Z. Formation, stabilities, and electronic and catalytic performance of platinum catalyst supported on non-metal-doped graphene. *The Journal of Physical Chemistry C 117*, 10 (2013), 5258–5268.

[172] Tang, Yanan, Yang, Zongxian, and Dai, Xianqi. Trapping of metal atoms in the defects on graphene. *The Journal of Chemical Physics 135*, 22 (2011), 224704.

[173] Twigg, M. V. Progress and future challenges in controlling automotive exhaust gas emissions. *Applied Catalysis B: Environmental 70*, 1–4 (2007), 2 – 15.

[174] Uchida, M., Aoyama, Y., Tanabe, M., Yanagihara, N., Eda, N., and Ohta, A. Influences of both carbon supports and heattreatment of supported catalyst on electrochemical oxidation of methanol. *Journal of The Electrochemical Society 142*, 8 (1995), 2572–2576.

[175] Üzengi A., Olcay, and Tomak, M. Au_nPt_n clusters adsorbed on graphene studied by first-principles calculations. *Phys. Rev. B 80* (2009), 085417.

[176] Vedala, H., Sorescu, D. C., Kotchey, G. P., and Star, A. Chemical sensitivity of graphene edges decorated with metal nanoparticles. *Nano Letters 11*, 6 (2011), 2342–2347.

[177] Wang, C., Waje, M., Wang, X., Tang, J. M., Haddon, R. C., and Yan. Proton exchange membrane fuel cells with carbon nanotube based electrodes. *Nano Letters 4*, 2 (2004), 345–348.

[178] Wang, J., Yin, G., Shao, Y., Zhang, S., Wang, Z., and Gao, Y. Effect of carbon black support corrosion on the durability of Pt/C catalyst. *Journal of Power Sources 171*, 2 (2007), 331 – 339.

[179] Wang, J.-g., Lv, Y.-a., Li, X.-n., and Dong, M. Point-Defect mediated bonding of Pt clusters on (5,5) Carbon nanotubes. *The Journal of Physical Chemistry C 113*, 3 (2009), 890–893.

[180] Wang, L.-L., and Johnson, D. D. Density functional study of structural trends for late-transition-metal 13-atom clusters. *Phys. Rev. B 75* (2007), 235405.

[181] Wang, S., Jiang, S. P., and Wang, X. Microwave-assisted one-pot synthesis of metal/metal oxide nanoparticles on graphene and their electrochemical applications. *Electrochimica Acta 56*, 9 (2011), 3338 – 3344.

[182] Wang, X., Waje, M., and Yan, Y. CNT-based electrodes with high efficiency for PEMFCs. *Electrochemical and Solid-State Letters 8*, 1 (2005), A42–A44.

[183] Wu, G., Huang, H., Chen, X., Cai, Z., Jiang, Y., and Chen, X. Facile synthesis of clean Pt nanoparticles supported on reduced graphene oxide composites: Their growth mechanism and tuning of their methanol electro-catalytic oxidation property. *Electrochimica Acta 111* (2013), 779 – 783.

[184] Xing, Y. Synthesis and electrochemical characterization of uniformly-dispersed high loading Pt nanoparticles on sonochemically-treated carbon nanotubes. *The Journal of Physical Chemistry B 108*, 50 (2004), 19255–19259.

[185] Xu, P., Dong, L., Neek-Amal, M., Ackerman, M. L., Yu, J., Barber, S. D., Schoelz, J. K., Qi, D., Xu, F., Thibado, P. M., and Peeters, F. M. Self-organized platinum nanoparticles on freestanding graphene. *ACS Nano 8*, 3 (2014), 2697–2703.

[186] Xu, Y., Getman, R. B., Shelton, W. A., and Schneider, W. F. A first-principles investigation of the effect of Pt cluster size on CO and NO oxidation intermediates and energetics. *Physical Chemistry Chemical Physics 10* (2008), 6009–6018.

[187] Yakovkin, I.N., and Petrova, N.V. Microscopic model of CO oxidation on pt(111). *Surface Science 600*, 12 (2006), 2600 – 2607.

[188] Yamagishi, S., Fujimoto, T., Inada, Y., and Orita, H. Studies of CO adsorption on Pt(100), Pt(410), and Pt(110) surfaces using density functional theory. *The Journal of Physical Chemistry B 109*, 18 (2005), 8899–8908.

[189] Yeo, Y. Y., Vattuone, L., and King, D. A. Calorimetric heats for CO and oxygen adsorption and for the catalytic CO oxidation reaction on Pt (111). *The Journal of Chemical Physics 106*, 1 (1997), 392–401.

[190] Yoo, E., Nagashima, Y., Yamazaki, T., Matsumoto, T., and Nakamura, J. Reduction of Pt usage in fuel cell electrocatalysts using carbon nanotubes and non-Pt metals. *Polymers for Advanced Technologies 17*, 7-8 (2006), 540–543.

[191] Yoo, E., Okada, T., Akita, T., Kohyama, M., Honma, I., and Nakamura, J. Subnano-Pt cluster supported on graphene nanosheets for CO tolerant catalysts in polymer electrolyte fuel cells. *Journal of Power Sources 196*, 1 (2011), 110 – 115.

[192] Yoo, E., Okata, T., Akita, T., Kohyama, M., Nakamura, J., and Honma, I. Enhanced Electrocatalytic Activity of Pt Subnanoclusters on Graphene Nanosheet Surface. *Nano Letters 9*, 6 (2009), 2255–2259.

[193] Yuan, D.W., Liu, Cong, and Liu, Z.R. Structures and catalytic properties of Pd_mAu_n (m+n=7) bimetallic clusters supported on graphene by first-principles studies. *Physics Letters A 378*, 4 (2014), 408–415.

[194] Zhang, Cheng, Lv, Wei, Yang, Quanhong, and Liu, Yuan. Graphene-supported nanoparticles of Pt–Ni for CO oxidation. *Applied Surface Science 258*, 20 (2012), 7795 – 7800.

[195] Zhang, S., Yuan, X.-Z., Hin, J. N. C., Wang, H., Friedrich, K. A., and S., Mathias. A review of platinum-based catalyst layer degradation in proton exchange membrane fuel cells. *Journal of Power Sources 194*, 2 (2009), 588 – 600.

[196] Zhao, Wengao, Zhou, Xibin, Chen, Jing, and Lu, Xiaoquan. Controllable electrodeposition of platinum nanoparticles on graphene nanosheet for methanol oxidation reaction. *Journal of Cluster Science 24*, 3 (2013), 739–748.

[197] Zhou, M., Zhang, A., Dai, Z., Zhang, C., and Feng, Y. P. Greatly enhanced adsorption and catalytic activity of Au and Pt clusters on defective graphene. *The Journal of Chemical Physics 132*, 19 (2010), 194704.

[198] Zhou, W.J., Song, S.Q., Li, W.Z., Sun, G.Q., Xin, Q., Kontou, S., Poulianitis, K., and Tsiakaras, P. Pt-based anode catalysts for direct ethanol fuel cells. *Solid State Ionics 175*, 1–4 (2004), 797 – 803.

[199] Zoval, J. V., Lee, J., Gorer, S., and Penner, R. M. Electrochemical Preparation of Platinum Nanocrystallites with Size Selectivity on Basal Plane Oriented Graphite Surfaces. *The Journal of Physical Chemistry B 102*, 7 (1998), 1166–1175.